MARCELO ARAÚJO DELGADO FILHO

ENHANCING FLUTTER ENERGY HARVESTING BY COMBINING VISCOELASTIC DAMPING AND NONLINEARITIES: A ROBUST-OPTIMAL DESIGN

UNIVERSIDADE FEDERAL DE UBERLÂNDIA

FACULDADE DE ENGENHARIA MECÂNICA

2025

MARCELO ARAÚJO DELGADO FILHO

ENHANCING FLUTTER ENERGY HARVESTING BY COMBINING VISCOELASTIC DAMPING AND NONLINEARITIES: A ROBUST-OPTIMAL DESIGN

Thesis submitted to the Graduate Program in Mechanical Engineering of the Federal University of Uberlândia as part of the requirements for obtaining the title of **PhD IN MECHANICAL ENGINEERING**.

Research Area: Solid Mechanics and Vibrations.

Supevisor: Prof. Dr. Antônio Marcos Gonçalves de Lima.

Co-supervisor: Prof. Dr. Noureddine Bouhaddi.

UBERLÂNDIA - MG

2025

Ficha Catalográfica Online do Sistema de Bibliotecas da UFU
com dados informados pelo(a) próprio(a) autor(a).

D352
2025

Delgado Filho, Marcelo Araújo, 1996-
Enhancing flutter energy harvesting by combining viscoelastic damping and nonlinearities [recurso eletrônico] : a robust-optimal design / Marcelo Araújo Delgado Filho. - 2025.

Orientador: Antônio Marcos Gonçalves de Lima.
Coorientador: Noureddine Bouhaddi.
Tese (Doutorado) - Universidade Federal de Uberlândia, Pós-graduação em Engenharia Mecânica.
Modo de acesso: Internet.
DOI http://doi.org/10.14393/ufu.te.2025.611
Inclui bibliografia.
Inclui ilustrações.

1. Engenharia mecânica. I. Lima, Antônio Marcos Gonçalves de, 1975-, (Orient.). II. Bouhaddi, Noureddine,1961-, (Coorient.). III. Universidade Federal de Uberlândia. Pós-graduação em Engenharia Mecânica. IV. Título.

CDU: 621

Bibliotecários responsáveis pela estrutura de acordo com o AACR2:
Gizele Cristine Nunes do Couto - CRB6/2091
Nelson Marcos Ferreira - CRB6/3074

UNIVERSIDADE FEDERAL DE UBERLÂNDIA
Coordenação do Programa de Pós-Graduação em Engenharia Mecânica
Av. João Naves de Ávila, nº 2121, Bloco 1M, Sala 212 - Bairro Santa Mônica, Uberlândia-MG, CEP 38400-902
Telefone: (34) 3239-4282 - www.posmecanicaufu.com.br - secposmec@mecanica.ufu.br

ATA DE DEFESA - PÓS-GRADUAÇÃO

<table>
<tr><td>Programa de Pós-Graduação em:</td><td colspan="5">Engenharia Mecânica</td></tr>
<tr><td>Defesa de:</td><td colspan="5">Tese de Doutorado, nº 410, PPGEM</td></tr>
<tr><td>Data:</td><td>30/09/2025</td><td>Hora de início:</td><td>09:00</td><td>Hora de encerramento:</td><td>11h40</td></tr>
<tr><td>Matrícula:</td><td colspan="5">12113EMC006</td></tr>
<tr><td>Nome do Discente:</td><td colspan="5">Marcelo Araújo Delgado Filho</td></tr>
<tr><td>Título do Trabalho:</td><td colspan="5">Enhancing flutter energy harvesting by combining viscoelastic damping and nonlinearities: a robust-optimal design</td></tr>
<tr><td>Área de concentração:</td><td colspan="5">Mecânica dos Sólidos e Vibrações</td></tr>
<tr><td>Linha de pesquisa:</td><td colspan="5">Dinâmica de Sistemas Mecânicos</td></tr>
<tr><td>Projeto de Pesquisa de vinculação:</td><td colspan="5">PQ</td></tr>
</table>

Reuniu-se por videoconferência a Banca Examinadora, designada pelo Colegiado do Programa de Pós-graduação em Engenharia Mecânica, assim composta: Prof. Dr. Flávio Luiz Cardoso Ribeiro - ITA; Prof. Dr. Edson Hideki Koroishi - UTFPR; Prof. Dr. Francisco José de Souza - UFU; Prof. Dr. Roberto Mendes Finzi Neto - UFU e Prof. Dr. Antônio Marcos Gonçalves de Lima - UFU; orientador do candidato.

Iniciando os trabalhos, o presidente da mesa, Prof. Dr. Antônio Marcos Gonçalves de Lima, apresentou a Comissão Examinadora e o candidato, agradeceu a presença do público, e concedeu ao Discente a palavra para a exposição do seu trabalho. A duração da apresentação do Discente e o tempo de arguição e resposta foram conforme as normas do Programa.

A seguir, o senhor presidente concedeu a palavra, pela ordem sucessivamente, aos examinadores, que passaram a arguir o candidato. Ultimada a arguição, que se desenvolveu dentro dos termos regimentais, a Banca, em sessão secreta, atribuiu o resultado final, considerando o candidato:

Aprovado.

Esta defesa faz parte dos requisitos necessários à obtenção do título de Doutor.

O competente diploma será expedido após cumprimento dos demais requisitos, conforme as normas do Programa, a legislação pertinente e a regulamentação interna da UFU.

Nada mais havendo a tratar, foram encerrados os trabalhos. Foi lavrada a presente ata que após lida e achada conforme foi assinada pela Banca Examinadora.

Documento assinado eletronicamente por **Antonio Marcos Gonçalves de Lima**, **Professor(a) do Magistério Superior**, em 30/09/2025, às 11:42, conforme horário oficial de Brasília, com fundamento no art. 6º, § 1º, do Decreto nº 8.539, de 8 de outubro de 2015.

Documento assinado eletronicamente por **Edson Hideki Koroishi**, **Usuário Externo**, em 30/09/2025, às 11:43, conforme horário oficial de Brasília, com fundamento no art. 6º, § 1º, do Decreto nº 8.539, de 8 de outubro de 2015.

Documento assinado eletronicamente por **Roberto Mendes Finzi Neto**, **Professor(a) do Magistério Superior**, em 30/09/2025, às 11:43, conforme horário oficial de Brasília, com fundamento no art. 6º, § 1º, do Decreto nº 8.539, de 8 de outubro de 2015.

Documento assinado eletronicamente por **Francisco José de Souza**, **Professor(a) do Magistério Superior**, em 30/09/2025, às 11:43, conforme horário oficial de Brasília, com fundamento no art. 6º, § 1º, do Decreto nº 8.539, de 8 de outubro de 2015.

Documento assinado eletronicamente por **Flávio Luiz Cardoso Ribeiro**, **Usuário Externo**, em 30/09/2025, às 11:44, conforme horário oficial de Brasília, com fundamento no art. 6º, § 1º, do Decreto nº 8.539, de 8 de outubro de 2015.

A autenticidade deste documento pode ser conferida no site https://www.sei.ufu.br/sei/controlador_externo.php?acao=documento_conferir&id_orgao_acesso_externo=0, informando o código verificador **6668317** e o código CRC **41EC4AC6**.

Referência: Processo nº 23117.063225/2025-21 SEI nº 6668317

To my grandma Hebe and uncle Wesley, who passed away during the course of this work. Death shall not prevail over the redeemed in Christ.

ACKNOWLEDGMENTS

To The Almighty Lord, the engineer of all creation, whose care and direction never cease, opening doors I had never imagined possible — to Him be all praise and glory.

To my family, whose support has been present in everything I do, including this research, celebrating each achievement as their own. I owe them my character and personal formation. Without it, I would never be able to succeed.

To my friends in Uberlândia, who made the work lighter and helped its development. To my RF/RN colleagues, Prince, the most *pragmatic* engineer and the best flight simulator pilot ever to live, and Ricardo, the legend of death metal - it was an honor, gentlemen. To Gutembergy, for all advice and both small and productive talks. Thanks for helping to generate the data set. To my fellow RU and LMEst colleagues, Leo Cabral, Maria, Ely, Raimundo, Heluise, Sicchieri, Fernandinha, Fernanda, Erivaldo and Larissa. I would like to thank Fernanda in particular for running some of the simulations while I was not at LMest.

To the generous João Pedro, always willing to help, for initially hosting me abroad and for all guidance on getting myself installed. I also thank him for the useful feedback on the neural network. Thanks to Arthur for receiving me in Besançon. Your lecture on numeric continuation and on non-dimensional nonlinear dynamics was invaluable. I cannot forget the help of Professor Rafael Teloli and his wife Daniele, who aided me substantially during the plumbing incident and had the hospitality of inviting me for Christmas. I also salute my colleagues from office 42H, Nour, Johann, Tsilat, Shakiba, and Océane, and fellow Brazilians abroad, Raqueti, Guilherme, Leonardo, and Catarina.

To my supervisor, Professor Antônio Marcos, for his guidance, understanding, and orientation since the master's degree, including his encouragement in my participation in the UFU–CAPES–PRINT program. I am also grateful to my co-supervisor, Professor Bouhaddi, and to Professor Kacem for welcoming me to FEMTO-ST, for their valuable feedback, and for their assistance with publications.

I acknowledge CAPES for funding my Ph.D. in Brazil and my sandwich period at FEMTO-ST (grant number 88887.846927/2023-00). Finally, I thank the Federal University of Uberlândia and FEMTO-ST for the opportunity and the infrastructure provided.

“Whatever you do, work heartily, as for the Lord and not for men.”

Colossians 3:23 (ESV)

Delgado Filho, M. A. **Aprimoramento do *havesting* de energia a partir de *flutter* por meio da combinação de amortecimento viscoelástico e não linearidades: um projeto ótimo-robusto** 2025. 92 f. Tese de Doutorado, Universidade Federal de Uberlândia, Uberlândia.

Resumo

Harvesting de energia configura-se como um campo de pesquisa muito ativo e promissor. Diversos fenômenos podem ser utilizados para realizar *harvesting*, especialmente em aplicações em pequena escala, como sensores, atuadores e sistemas de controle, que vêm se tornando cada vez mais comuns na prática da engenharia. Entre as opções disponíveis, as vibrações induzidas pelo escoamento do ar destacam-se por sua elevada disponibilidade. O *flutter*, sempre evitado no projeto de estruturas e aeronaves, representa uma fonte de energia promissora. Trata-se de uma instabilidade aeroelástica autoexcitada associada a oscilações de grande amplitude. Além disso, o *flutter* aplicado a *harvesting* constitui uma abordagem versátil e estruturalmente simples. No entanto, o *flutter* ocorre em uma determinada velocidade de escoamento, acima da qual o sistema apresentará oscilações com amplitude continuamente crescente. Assim, a incorporação de não linearidades tem sido proposta na literatura com o objetivo de se obter um suprimento de energia controlado e persistente, na forma de oscilações de ciclo limite. As não linearidades podem ainda reduzir a velocidade do escoamento necessária para que o *harvesting* ocorra. Ao mesmo tempo, o amortecimento viscoelástico foi sugerido como meio de suprimir o *flutter*. Diante do apresentado, a presente tese busca avaliar o uso de não linearidades do tipo *hardening* e *free-play*, em conjunto com amortecimento viscoelástico, para aprimorar e controlar o harvesting de energia a partir do *flutter* de um aerofólio com dois graus de liberdade e transdução piezoelétrica. Propõe-se a otimização robusta do sistema, considerando a influência de variações paramétricas no desempenho de *harvesting*, especialmente motivada pela forte dependência da temperatura introduzida pelos amortecedores viscoelásticos. A combinação proposta de não linearidades estruturais com amortecedores viscoelásticos demonstra ser capaz de aumentar consideravelmente a potência e ampliar a faixa de velocidades de operação, seja pela redução da velocidade mínima necessária para o *harvesting*, seja pelo controle da amplitude do ciclo limite no pós-flutter. Além disso, a metodologia de otimização robusta empregada permite projetar um sistema de *harvesting* de energia que apresente robustez frente a variações de temperatura, ao mesmo tempo em que alcance o melhor desempenho possível. Nesse sentido, constatou-se que a potência média é mais sensível às variações de temperatura do que o intervalo de velocidade de operação. Conclui-se que a combinação de não linearidades estruturais com amortecedores viscoelásticos é benéfica para o *harvesting* a partir do *flutter*, sendo possível a obtenção de sistemas com desempenho ótimo-robusto.

Palavras-chave: Harvesting de energia. Flutter. Aeroelasticidade não linear. Amortecimento viscoelástico. Otimização robusta.

Delgado Filho, M. A. **Enhancing flutter energy harvesting by combining viscoelastic damping and nonlinearities: a robust-optimal design.** 2025. 92 f. PhD Thesis, Universidade Federal de Uberlândia, Uberlândia.

Abstract

Energy harvesting stands as a very active and promising research field. Many phenomena may be used to harvest energy, particularly for small-scale applications such as sensors, actuators, and control systems, which are becoming increasingly widespread in engineering practice. Among the many options, flow-induced vibration is notable for its high availability. Always avoided in the design of structures and aircraft, flutter represents an encouraging source of power. It is a self-excited aeroelastic instability associated with high-amplitude oscillations. In addition, flutter energy harvesting is a versatile and structurally simple approach. However, flutter occurs at a given airspeed, above which the system will display oscillations with an ever-growing amplitude. Thus, the incorporation of nonlinearities has been proposed in the literature to yield a controlled and persistent power supply in the form of limit-cycle oscillations and to reduce the airspeed needed for harvesting to take place. At the same time, viscoelastic damping was suggested to suppress flutter. The present thesis attempts to evaluate the use of hardening and free-play nonlinearities together with viscoelastic damping to enhance and control flutter energy harvesting of a two-degree-of-freedom airfoil with piezoelectric transduction. Robust optimization of the system is proposed considering the influence of varying parametric variations on harvesting performance, especially motivated by the strong temperature dependence introduced by viscoelastic dampers. The proposed combination of structural nonlinearities with viscoelastic dampers proves capable of considerably increasing the power output and broadening the operating velocity range, either by reducing the minimum velocity required for harvesting or by controlling the limit cycle amplitude in the post-flutter regime. Furthermore, the robust optimization methodology employed enables the design of an energy harvesting system that is robust to temperature variations while still achieving optimal performance. In this regard, it was found that the average power is more sensitive to temperature variations than the operating velocity range. It is therefore concluded that the combination of structural nonlinearities with viscoelastic dampers is beneficial for flutter-based energy harvesting, enabling systems with robust-optimal performance.

Keywords: Energy harvesting. Flutter. Nonlinear aeroelasticity. Viscoelastic damping. Robust optimization.

LIST OF FIGURES

LIST OF TABLES

LIST OF ABBREVIATIONS AND ACRONYMS

LMEst	Structural Mechanics Laboratory
UFU	Federal University of Uberlândia
VED	viscoelastic damper
FEM	finite element method
DLM	doublet lattice method
LCO	limit cycle oscillation
FEH	flutter energy harvesting
DOF	degree-of-freedom
FDM	fractional derivative model
IoT	internet of things
CWS	cut-in wind speed
NSGA II	non-dominated sorting genetic algorithm II
NN	neural network
NACA	National Advisory Committee for Aeronautics
MOP	multi-objective optimization problem
RMOP	robust multi-objective optimization problem
LHS	latin hypercube sampling
MLP	multi-layer perceptron
PAPA	pitch and plunge apparatus
ITA	Aeronautics Institute of Technology
FFT	Fast Fourier transform
rms	root mean square
RMSE	root mean square error

LIST OF SYMBOLS

a	Dimensionless location of the elastic axis
a_0^h, a_0^θ	Linear stiffness coefficients
$a_0^{E,G}$, $a_1^{E,G}$, $b_0^{E,G}$, $b_1^{E,G}$	Coefficients of the fractional derivative model
a_1^h, a_1^θ	Cubic stiffness coefficients
α	Electromechanical coupling term
b	Semi-chord
$\bar{q}$	Electric charge
$\bar{V}$	Normalized airspeed
$\bar{\Lambda}$	Eigenvalue
c	Airfoil chord
c_h, c_θ	Viscous damping coefficients
$C(k)$	Theodorsen function
C_L	Lift coefficient
C_M	Moment coefficient
C_{eq}	Equivalent capacitance of the piezoelectric material
$(CD)^i$	Crowding distance
χ	Generic displacement
ΔP	Pressure difference
Δt	Time step
Δx	Perturbation
Δy	Variation in the objective function
$\Delta \mathbf{q}^s_{t+\Delta t}$	Displacement vector increment

d	Number of design variables
d_{ij}	Euclidean distance between two individuals
D	Drag
E	Young's modulus of elasticity
$E^*(\omega)$	Complex modulus of elasticity
ϵ	Deformation
$\eta(\omega)$	Loss factor
$F^h_{t-\Delta t}$, $F^\theta_{t-\Delta t}$	Viscoelastic dissipative forces
$f(t)$	Generic function of time
f^v_n	Vulnerability function
f^i_ϑ	Value of a given objective function of an individual
$\mathbf{f}(\mathbf{x})$	Vector of objective functions
$Front$	Front counter
$\phi(s)$	Wagner function
ϖ_i	Fitness function
φ	Velocity potential
γ	Shear deformation
gen	Generation counter
g^v_j	Grünwald coefficient
$\mathbf{g}\left(\mathbf{x}\right)$	Inequality restrictions
$\mathbf{g_{eq}}\left(\mathbf{x}\right)$	Equality restrictions
Γ	Vortex strength
Γ^*	Gamma function
h	Plunge displacement
h_{fp}	Semi-free-play in plunge
h^v_{fp}	Free-play in the viscoelastic damper in plunge
$H^{(2)}_j(k)$	Hankel function of the second kind
$\mathbf{H}$	Electromechanical vector

I	Moment of inertia
J	Memory size
k	Reduced frequency
k_{fp}^{v}	Discontinuous viscoelastic stiffness in plunge
k_h^l, k_θ^l	Linear stiffness terms
k_h^{nl}, k_θ^{nl}	Nonlinear stiffness terms
k_h^v, k_θ^v	Viscoelastic stiffness terms
κ	Recurrent term of the fractional derivative model
l	Span
Λ	Source strength
l_x, l_y, l_z	Dimensions of the prismatic viscoelastic damper in plunge
l_θ	Length of the viscoelastic damper in pitch
λ_1, λ_2	Aerodynamic lag states
L	Lift
m	Airfoil mass
m_s	Mass of the supporting structure
m_t	Total mass
M	Pitching moment
μ	Viscosity
μ_n	Mean
n	Number of objectives
N_J	Number of memory points
N_s	Niche size
ν, δ	Newmark's parameters
P	Pressure
p	Power
p_h	Shear area per unit of thickness of the viscoelastic damper in plunge
p_θ	Geometric factor of the viscoelastic damper in pitch

p_{rms}	Root mean square value of power
ψ, ι	Fractional derivative order
$\mathbf{q}$	Displacement vector of the degrees-of-freedom
q_j	Generalized coordinate
q_∞	Dynamic pressure
Q_j	Non-conservative forces
R	Electrical resistance
R_e	External radius of the viscoelastic damper in pitch
R_i	Internal radius of the viscoelastic damper in pitch
ρ	Specific mass
ρ_∞	Air density
r	Radial coordinate
r_θ	Radius of gyration
$\mathbf{R}_{t+\Delta t}^{n-1}$	Residue vector of the Newton–Raphson method
S	First moment of mass
$S_f(d_{ij})$	Sharing function
σ	Tensile stress
σ_n	Standard deviation
s	Non-dimensional time
τ	Shear stress
T	Temperature
T_k	Kinetic energy
θ	Pitch angle
θ_{fp}	Semi-free-play in pitch
tol	Tolerance
t	Time
t_v	Thickness of the viscoelastic damper in pitch
U	Potential energy

U_d	Deformation energy
υ	Volume of the viscoelastic damper
V	Airspeed
V_{ef}	Effective airspeed
V^*	Linear flutter speed
v	Voltage
ϱ	Ratio of specific heats
ζ	Damping factor
$\hat{a}$	Lift curve slope
ξ	Dummy integration variable
$\mathbf{A}$	State matrix
$\bar{\mathbf{C}}$	Total damping matrix
$\bar{\mathbf{K}}$	Total stiffness matrix
$\bar{\mathbf{K}}_{\mathbf{v}}^{\mathbf{nl}}$	Nonlinear total stiffness matrix with viscoelastic damping
$\bar{\mathbf{M}}$	Total mass matrix
$\tilde{\mathbf{C}}$	Aeroelastic damping matrix
$\tilde{\mathbf{K}}$	Aeroelastic stiffness matrix
$\tilde{\mathbf{K}}^{\mathbf{nl}}$	Nonlinear aeroelastic stiffness matrix
$\tilde{\mathbf{K}}_{\mathbf{v}}^{\mathbf{nl}}$	Nonlinear aeroelastic stiffness matrix with viscoelastic damping
$\tilde{\mathbf{M}}$	Aeroelastic mass matrix
$\mathbf{F}_{\mathbf{v}}$	Dissipative force vector
$\mathbf{X}$	Decision space
$\mathbf{Y}$	Objective space

CONTENTS

CHAPTER I

INTRODUCTION

The growing need and relevance of energy has motivated the development of new generation strategies (YANG; GUO; SUN, 2022). At the same time, concepts as digital twins applied to structural health monitoring harness sensor streams following an Internet of Things (IoT) paradigm to dynamically update physics-based and machine learning models that simulate structural behavior in real time, supporting predictive maintenance, virtual inspection, and performance optimization (WANG et al., 2025). The implementation of industry 4.0 practices also requires an intense use of sensors with small- and microscale electronics. The field of smart structures also demands such devices.

If necessary, battery replacement can hinder the application of these technologies, particularly in remote areas (LI; ZHOU; LI, 2022) or difficult-to-access machinery. This power request stimulated progress in energy harvesting (BENI; BENI, 2022), which proposes making use of available ambient sources, received considerable attention (LIU; LI; YANG, 2018). Figure 1.1 shows this trend. In fact, a centimeter-sized harvester can power an electrical sensing unit (NAQVI et al., 2022). Furthermore, by eliminating batteries, the harvesting approach reduces chemical waste and costs (ERTURK; INMAN, 2011), which is evidently highly desirable.

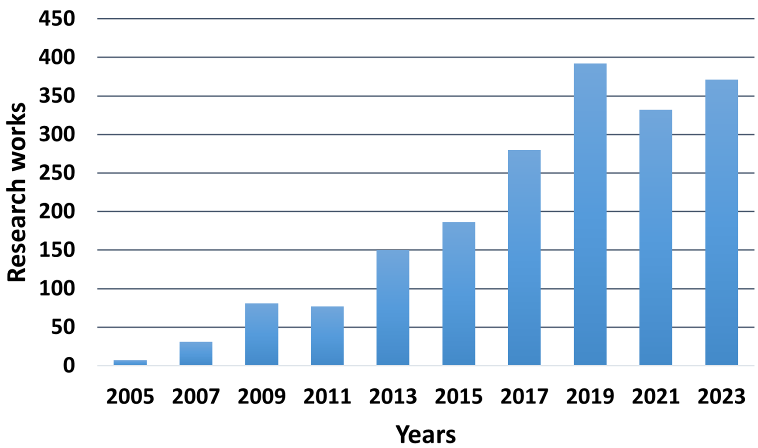

Figure 1.1 – Number of publications on energy harvesting in the field of mechanical engineering per year (CLARIVATE ANALYTICS, 2025).

Various readily available energy sources in the operating environment can be transformed

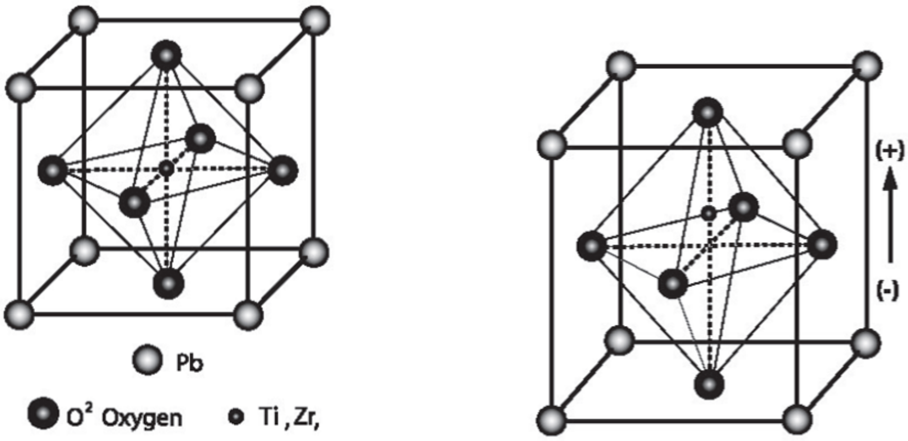

(a) (b)

Figure 1.2 – Structure of a piezoelectric ceramic above the Curie temperature (a) and below it (b) (MOHEIMANI; FLEMING, 2006).

into electrical power, such as solar, thermal, and kinetic energy. The latter usually assumes the form of mechanical vibrations and benefits from a high power density (BONNIN; TRAVERSA; BONANI, 2021).

As different physical phenomena may be used to harvest energy, vibration-based energy harvesting usually comes from electromagnetic, electrostatic, triboelectric, or piezoelectric effects (SHAN et al., 2020). To improve performance, more than one mechanism can be used in hybrid designs. The piezoelectric method, in particular, has clear advantages over the other approaches, such as high energy density and structural simplicity (SHAN et al., 2020), which allows its incorporation into structures that display aeroelastic oscillations (ERTURK; INMAN, 2011).

The direct piezoelectric effect denotes the conversion of strain into electrical charge, while the inverse is also possible (MCCARTHY et al., 2016). This occurs because the crystalline structure of piezoelectric ceramic has tetragonal symmetry at temperatures below a given value, known as the Curie temperature, developing a dipole moment (MOHEIMANI; FLEMING, 2006). The alignment of the dipoles of various crystals (polarization) means that the material will produce voltage if the dipole moments are changed, which can be achieved by applying tension or compression (MOHEIMANI; FLEMING, 2006). In the opposite situation, where an applied voltage deforms the material, piezoelectric ceramics work as actuators.

Among other sources, wind-induced vibration is highly available, clean, and renewable (LI; ZHOU; YANG, 2022). It can take the form of a bluff body vibrating due to a vortex, the galloping movement of a prismatic body, or oscillations caused by a wake or flutter (LIU; LI; YANG, 2018).

Vortex-induced vibration occurs when an alternate shedding of vortexes, created by uniform flow around a bluff body, has a frequency close to any natural frequency of the harvesting structure (ABDELKEFI, 2016). In a similar way, wake-induced vibration uses the wakes created by a fixed, separated bluff body to set the harvesting structure in motion. Although these two approaches are possible, they are highly dependent on specific flow conditions, which can make their practical implementation difficult. In contrast, galloping and flutter are more flexible approaches as both are self-excited oscillations that manifest at a given critical airspeed.

The main difference between galloping and flutter is that the first occurs when the aerodynamic force exceeds the structural damping, identified by a negative derivative of the aerodynamic lift coefficient (ABDELKEFI, 2016). Flutter, on the other hand, is a modal coupling phenomenon in which two or more vibration modes interact so that one of them becomes negatively damped, leading to sustained or growing oscillations of high amplitude (FUNG, 1993). Thus, galloping is a single degree-of-freedom (DOF) phenomenon, while flutter requires at least two. Therefore, flutter energy harvesting (FEH) has more DOF available for harvesting, which favors hybrid approaches. For an airfoil, one can employ piezoelectric and electromagnetic transduction to harvest power from the translational and rotational DOFs, respectively (MCCARTHY et al., 2016). Another advantage of aeroelastic energy harvesting lies in its simplicity and robustness (BRYANT; GARCIA, 2009b).

Usually, flutter is a major concern when designing aircraft and structures subjected to airflow, such as bridges and tall buildings. However, in the context of energy harvesting, these oscillations are a desirable source of energy, having the possibility of reaching a high output voltage (LI; ZHOU; LI, 2022) above the cut-in wind speed (CWS), the minimum airspeed needed to achieve energy harvesting.

Even if FEH has potential for small-scale power generation in several environments, it is not mature enough for practical use given some limitations that include its low efficiency, narrow bandwidth, and sensitivity to airflow velocity and orientation (LI; ZHOU; YANG, 2022). Although the latter can be solved by adding a tail vane to the system, which is a simple and passive solution capable of keeping airflow alignment, the remaining problems pointed out require further investigation, motivating additional studies.

A solution to the above constraints might involve the incorporation of nonlinearities into the system, as there is a consensus in the literature that this benefits FEH (SOUSA et al., 2011; ABDELKEFI, 2016; WANG et al., 2018; BOUMA et al., 2022; AMARAL; DE MARQUI; SILVEIRA, 2023; HAO; LI, 2025) and, therefore, would be a preferred research direction to increase its feasibility (LI; ZHOU; YANG, 2022). Moreover, among other parameters, airspeed should be prioritized, as it is a fundamental factor (NAQVI et al., 2022).

As shown in Fig. 1.3, the nonlinear flutter phenomenon is a Hopf bifurcation (BERAN; STANDFORD; SCHROCK, 2017). Depending on the nonlinear configuration present, LCOs can manifest themselves in supercritical (Fig. 1.3a) or subcritical (Fig. 1.3b) fashion (ERTURK; INMAN, 2011). In the former, the amplitude increases when the airspeed is swept upward, following the same path in the opposite sweeping direction. Furthermore, before V^*, the system is dynamically stable, and any perturbation will result in an oscillation that dies over time. This is not true for the subcritical case, as the paths differ depending on the sweeping direction, leading to LCOs for airspeeds lower than V^*. Hence, the subcritical case could reduce the CWS and favor energy harvesting.

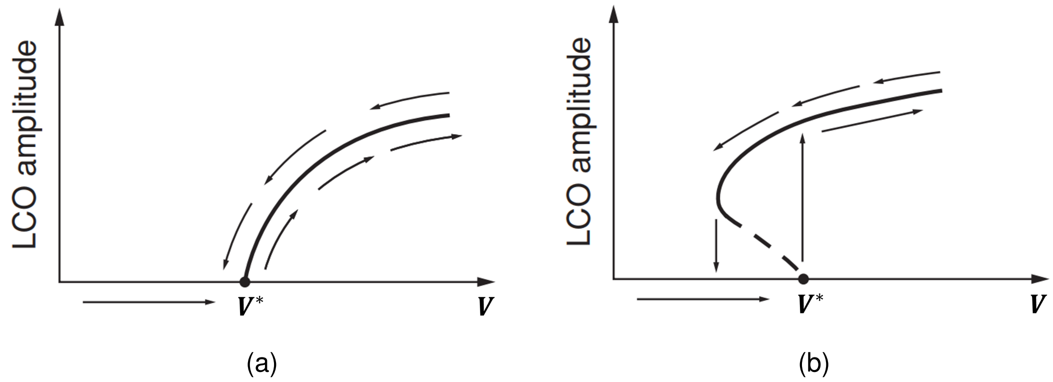

Figure 1.3 – Supercritical (a) and subcritical (b) Hopf bifurcations related to flutter (adapted from ERTURK and INMAN (2011)).

Another positive impact of adding nonlinearity to FEH is that LCOs represent a way to limit the system response. In fact, this might be crucial, since linear aeroelasticity predicts an infinite steady-state amplitude at any airspeed greater than V^*. Therefore, the LCO represents a way to achieve harvesting at supercritical airspeeds with a bounded amplitude, thus creating a persistent power source. In contrast, linear FEH can only attain power at flutter speed, where the response is harmonic. Any slight decrease in airspeed will not result in a sustainable oscillation, and any increase would cause ever-growing unstable oscillations (BRYANT; GARCIA, 2009a). This is precisely the reason why a large flutter safety margin is imposed on aeronautical vehicles.

Even in the presence of strong structural nonlinearities, the LCO amplitude in the post-flutter regime can reach the order of centimeters (TIAN et al., 2022), which may require control. Moreover, doing so could extend the maximum airspeed at which FEH is achieved without reaching a prohibitive amplitude. Clearly, as the goal is to harvest energy, passive control methods are preferred. An option is the use of a viscoelastic damping mechanism, as it has been widely used to control vibration (RAO, 2010).

Many viscoelastic materials are polymers, composed of long chains of repeated molecular units that become interconnected through chemical or physical interactions, creating an intricate network (Fig. 1.4a). For example, Fig. 1.4b illustrates the structure of a vulcanized viscoelastic material used in a viscoelastic damper (VED). In such material, the elasticity comes from cross-linked molecular networks, while viscosity arises from the entanglement and mobility of unbound chains (SHU; YOU; ZHOU, 2022).

Due to the molecular interactions of their inherently long and highly interconnected structure, many polymeric and vitreous materials display a particular type of internal dissipation mechanism called viscoelastic damping (MARTINS, 2014). As in the strain-stress diagram in Fig. 1.5, part of the strain energy dissipates during unloading, given the divergence of the loading and unloading paths, in a hysteretic fashion (LEAL JUNIOR et al., 2017). It is precisely this internal damping mechanism that makes viscoelastic materials suitable for passive vibration control.

Although the use of viscoelastic damping is usually considered as a way to suppress flutter in aeronautic structures, that is clearly not the case when the goal is FEH. However, some

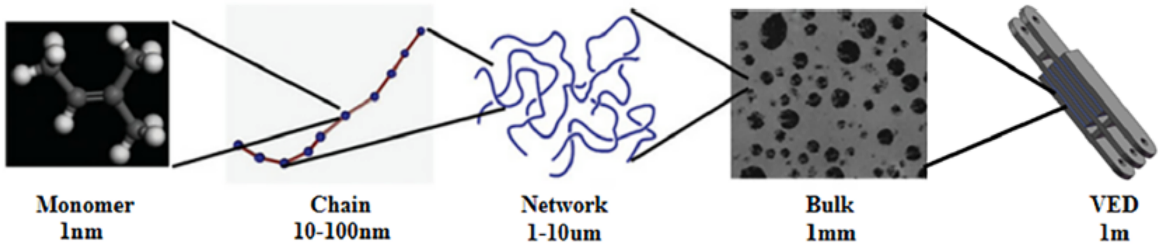

(a)

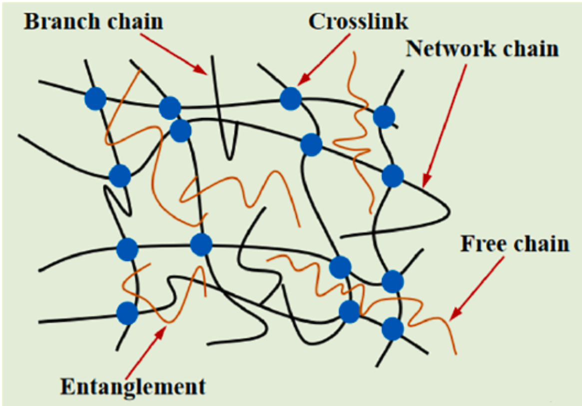

(b)

Figure 1.4 – Hierarchical length scales for polymeric materials (a) (Adapted by SHU, YOU and ZHOU (2022) from LI et al. (2012)) and microstructure of a vulcanized viscoelastic material (SHU; YOU; ZHOU, 2022) (b).

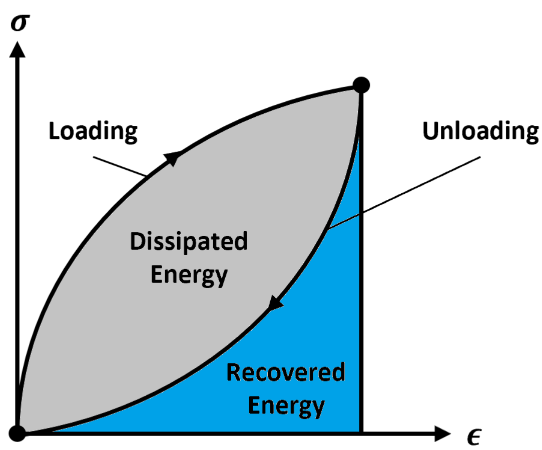

Figure 1.5 – Stress-strain curve for a viscoelastic material.

references (WANG et al., 2018; TIAN et al., 2021; TIAN et al., 2022) concluded that the best harvesting performance may be associated with intermediary values of the individual stiffness and damping terms of each DOF. As VEDs add both damping and stiffness, they could be used to tune the system performance, provided that a nonlinear configuration creates an LCO. Moreover, a VED can be conveniently incorporated into a given DOF. Therefore, the use of viscoelastic damping together with structural nonlinearities could be highly beneficial for FEH, motivating the development of this thesis.

1.1 State of the art

This section summarizes some of the most relevant works in the context of this thesis and recent contributions. In addition, associated research carried out in the structural mechanics laboratory (LMEst) at the Federal University of Uberlândia (UFU) is also included. The research is divided into two sections. First, work on flutter energy harvesting is discussed followed by studies on the use of viscoelastic damping for aeroelastic control.

1.1.1 Flutter energy harvesting

BRYANT and GARCIA (2009a) conducted pioneering work in FEH, proposing a wing connected to piezoelectric beams. An ingenious strategy was used to extend the working envelope of the harvester in terms of wind speed. It consisted of designing the system so that harvesting only starts after reaching a given vibration amplitude, when the circuit is switched on. Due to the shunt damping effect, the critical speed would be increased and the system would enter a stable condition. Hence, the amplitude would decay until reaching a minimum value that would switch off the piezoelectric circuit so that the critical speed reduces and flutter can restart. Thus, the method results in a safe and continuous periodic harvesting at any airspeed superior to the critical. This represents a smart way to make FEH practical in linear aeroelastic systems, as otherwise the harvesting would be restricted to the flutter speed.

As FEH can assume different designs and configurations, BRYANT and GARCIA (2009b) experimentally compared different geometries for FEH, namely a flat plate wing and a NACA 0012 airfoil. Although the CWS was not very different for the two designs, the airfoil showed a higher oscillation amplitude.

MCCARTHY et al. (2013) proposed two harvesters in tandem to investigate how flow patterns, particularly vortices shed from the first flutter harvester, can lead to an increase in power output in the downstream harvester. To accomplish this goal, a new bi-lighting technique was developed to visualize the flow structures. The flutter harvesters consist of a piezoelectric stalk connected to a triangular polypropylene leaf.

To improve performance DIAS, DE MARQUI and ERTURK (2015) employed a hybrid FEH approach for a three-DOF airfoil. The plunge DOF was connected to both piezoelectric and electromagnetic transductions and a parametric study was carried out to identify favorable design configurations. The highest power came from a combination of resistances from each harvesting circuit. Moreover, the authors point out that the three-DOF airfoil widens the design space compared to its two-DOF counterpart.

Power output and power extraction efficiency were shown to increase substantially by adding a beam stiffener to a beam-airfoil harvester in the work of ZHAO and YANG (2015). This was observed for different wind energy harvesting mechanisms, namely, galloping, vortex-induced vibration, and flutter. Among these, although galloping yields superior power at high airspeeds, FEH showed the highest efficiency and was recommended to operate in a wide range of airspeeds. The positive effect of the stiffener is explained by the increase in electromechanical coupling.

A double plunge airfoil for FEH was proposed by WU et al. (2017). Above the flutter speed, the device has higher power and efficiency compared to the traditional two-DOF airfoil. In addition, a parametric analysis was performed with the objective of evaluating the impact of various parameters on the CWS and harvesting efficiency. As a result, parametric design recommendations were made.

Linear stability analysis of a thin plate and flap FEH device was performed by RONG, CAO and HU (2017), who identified geometric ratios that could reduce the CWS. The post-critical behavior of the system was experimentally measured, showing that, above the critical value, only the amplitude increases with the airspeed while vibration frequency tends not to be considerably affected.

The post-critical response of a linear flat-plate was investigated both numerically and experimentally by PIGOLOTTI et al. (2017), from a harvesting perspective. Some general design recommendations are given to reduce CWS. In particular, it is concluded that the mass ratio, polar inertia, and pitch damping should be low, while the plunge and pitch modes should have similar natural frequencies at zero airspeed.

ERTURK et al. (2010) formulated a variation of the k-method to compute the flutter speed of a linear pitch and plunge airfoil with viscous damping and a piezoelectric element in the plunge DOF, experimentally validating the model. Although their system is linear, the authors suggest that nonlinear stiffness components and/or free-play can create an LCO of acceptable amplitude to provide persistent power for a wider range of airspeeds. This was investigated by SOUSA et al. (2011) by inserting a combination of hardening and free-play structural nonlinearities into the pitch DOF of a two-DOF airfoil. It was concluded that increasing the former intensity helped to control the LCO amplitude in the supercritical regime and that the latter could reduce the CWS, hence favoring energy harvesting. Furthermore, free-play alone was responsible for doubling the power output at the flutter boundary compared to its linear counterpart at the same airspeed. Another interesting result is that there is an optimal value for electrical resistance in terms of harvested power.

Taking into account the nonlinear dynamic stall effect at large deflections of a NACA 0012 flap at the tip of a cantilevered beam, BRYANT and GARCIA (2011) demonstrated, by theory and experiments, that energy harvesting in the post-flutter regime is dominated by these nonlinear effects.

By including cubic hardening nonlinearities in both DOFs of a two-DOF airfoil with quasi-steady aerodynamics and a dynamic stall model, ABDELKEFI, NAYFEH and HAJJ (2012) carried out a parametric study on the performance of FEH. The existence of an optimal electrical resistance value for the power output was again indicated. However, the influence of resistance on pitch and plunge amplitudes is negligible. The nonlinear torsional spring has the most influence in the system dynamics, being able to convert the bifurcation to subcritical.

The addition of nonlinearity in the piezoelectric coupling was proposed by AMARAL, DE MARQUI and SILVEIRA (2023) for a two-DOF airfoil with hardening in plunge. Both nonlinearities improved power generation. However, hardening was shown to also increase the CWS, revealing a compromise between this parameter and power generation.

Using computational fluid dynamics, TIAN et al. (2022) investigated the FEH performance of a similar airfoil with hardening in pitch and in plunge. The model was experimentally validated and compared with the theoretical prediction of unsteady aerodynamics. All three methods yielded similar results. The extensive parametric study demonstrated that the best harvesting configuration is associated with intermediary values of the pitch damping and plunge linear stiffness coefficients. Thus, the relation of damping and stiffness is non-monotonic, indicating the complexity of designing nonlinear piezoaeroelastic systems.

In a previous contribution, TIAN et al. (2021) have shown that the unsteady approach was the closest to the experimental results in relation to the quasi-steady and dynamic stall models. Quadratic terms were considered in addition to the cubic hardening coefficients. Parametric analysis suggested that the nonlinearity in pitch has a stronger influence on the system and should be small to increase performance which was also associated with intermediary values of the plunge linear stiffness coefficient.

Recently, HAO and LI (2025) proposed to investigate the effect of airspeed disturbance in a two-DOF airfoil with cubic and quintic stiffness in pitch and plunge. It was concluded that the disturbance could reduce CWS or reduce harvesting efficiency, depending on its magnitude. Moreover, the voltage increased together with the amount of the nonlinearity in plunge.

Another work demonstrating the benefits of the hardening nonlinearity in FEH was carried out by WANG et al. (2018). Their analysis of a two-DOF flat plate showed that hardening increased the harvesting efficiency while reducing the amplitudes of the DOFs. The possibility of using hardening to convert quasi-periodic oscillations to single periodic ones, which are more suitable for energy harvesting according to the authors, is also pointed out. It is observed that subcritical LCOs are possible if a large initial perturbation is applied to the system. Moreover, the oscillations in the supercritical regime are limited by aerodynamic nonlinearities such as vortex shedding and dynamic flow separation. Finally, there was a compromise between power and CWS in relation to viscous damping in plunge.

Aerodynamic nonlinearity was also considered by SANTOS, MARQUES and HAJJ (2019), who used a dynamic stall model together with hardening and free-play in the pitch spring to perform a parametric analysis of a two-DOF airfoil capable of harvesting from both pitch and plunge DOFs. Free-play reduced the CWS at the expense of the power harvested from the pitch DOF. A similar compromise was observed for the mass ratio. As for the hardening effect, although it also reduced the power extracted from pitch, it could increase the power generated from plunge depending on the parameters of the system. Due to the complexity of the system, an optimization problem was proposed to maximize the power generated by both the DOF as a function of the plunge and pitch frequency ratio and dimensionless mass ratio.

BOUMA et al. (2022) used multi-segmented discontinuous nonlinearities in the pitch DOF of a piezoelectric energy harvesting airfoil to obtain a subcritical bifurcation and hence reduce the CWS. Furthermore, the authors point out the need to limit the pitch amplitude to prevent structural damage and aerodynamic stall. This control effect can be achieved by the proposed nonlinearity. Thus, a compromise is observed in terms of harvesting and safe and continuous operation of the system.

Motivated by its previous application to control LCOs in aeroelastic systems, FASIHI, SHAHGHOLI and GHAHREMANI (2022) investigated the incorporation of a nonlinear energy sink into a two-DOF airfoil with piezoelectric transduction. Among other effects, the parametric analysis of the numerical-analytical model showed that the harvesting efficiency improved for a particular range of the nonlinear energy sink stiffness.

According to an analytical and numerical investigation of LIU and GAO (2019), the internal resonance of a two-DOF airfoil with piezoelectric transduction was shown to increase the harvested voltage and power. Beyond flow-induced vibration, there was also a base excitation. To simulate the former, a quasi-steady aerodynamic model with stall effects was used.

To harvest energy at low airspeeds, LI et al. (2019) proposed a magnetically coupled nonlinear harvester composed of a two-DOF airfoil connected to a beam. Simulations and experiments show that this device could operate at a lower CWS, and have higher performance. With the same goal, LI, YANG and ZHOU (2020) developed a bi-stable magnetic coupled system, showing that this effect could convert a supercritical bifurcation into a subcritical one, thus reducing the CWS. In addition, the output voltage was also improved.

A similar configuration was evaluated by ZHOU et al. (2019). It consisted of a rectangular wing connected to a beam. The wing had magnets in its extremity that interacted with fixed external ones. The system was bistable at low airspeed and tri-stable at high airspeed. According to experiments, energy harvesting could be achieved at airspeeds as low as 1.5 m/s.

LI, ZHOU and LI (2022) proposed a beam-airfoil FEH device capable of harvesting vibration from piezoelectric and electromagnetic effects using a piezoelectric patch and a combination of fixed and moving magnets to induce current in a coil. It is observed that this approach can reduce CWS and increase power. A parametric analysis is carried out to identify favorable values for the distances between the magnets and the ideal electrical resistance connected to the coil.

ABDEHVAND, ROKNIZADEH and MOHAMMAD-SEDIGHI (2021) used a beam attached to an airfoil covered with layers of a magneto-electro-elastic material to harvest energy from flutter. This composite exhibits piezoelectric and piezomagnetic properties. Therefore, an external coil was necessary to generate power from the magnetic field variation, which complemented the power produced from the deformation of the composite layers. The hybrid approach increased power by more than 10 $\%$ compared to the piezoelectric approach alone.

SHAN et al. (2020) employed a hybrid approach that combined FEH with vortex-induced harvesting. The device consisted of an airfoil with a cantilever beam attached to its end. The other end of the beam was connected to a bluff body to enable energy harvesting from vortices. Both strategies increased each other's performance. The LCO developed chaotic behavior as the airspeed increased.

1.1.2 Viscoelastic damping for aeroelastic control

Few research works have focused on the use of viscoelasticity for aeroelastic control. According to MARTINS et al. (2022), a pioneering study was carried out by HILTON (2010). This reference emphasizes the importance of time-dependent phenomena such as creep, stress relaxation, and creep buckling in the structural analysis of aerospace structures with viscoelastic properties.

In the aeroelastic context, viscoelastic damping was proposed mainly to increase the flutter speed. In supersonic flow, constrained viscoelastic layers were successfully used to tackle aircraft panel flutter (CUNHA FILHO et al., 2016a; CUNHA FILHO et al., 2016b). Temperature and layer thickness are shown to have a significant effect on aeroelastic stability.

The supersonic flutter of a cylindrical viscoelastic sandwich shell using Zener FDM was analyzed by MOKHTARI, PERMOON and HADDADPOUR (2019) for different geometric ratios. It is observed a non-monotonic relationship between constraining layer thickness and the critical condition. Moreover, it is possible to adjust different thickness ratios in such a way that the increase in the critical pressure by increasing the viscoelastic layer does not change the stiffness of the complete structure. In addition, there is a remarkable influence of viscoelastic properties on the stability boundary.

Viscoelastic damping can also suppress flutter in subsonic flow. This was demonstrated by MARTINS et al. (2017) for a two-DOF linear airfoil, both experimentally and numerically, in a frequency domain analysis. The authors also pointed out the possibility to optimize the VEDs to obtain the desired aeroelastic behavior, highlighting their constructive simplicity and design versatility.

Another study employing VEDs to improve the aeroelastic stability of was carried out by MARTINS et al. (2022), for a three-DOF airfoil (pitch, plunge and control surface). It showed that this approach could increase the flutter speed in 25.6 $\%$ alone and in 34.1 $\%$ when combined with proportional derivative control by the flap DOF, in a hybrid fashion. The gain from the active approach alone was 16.2 $\%$, indicating that it has a weaker impact compared to the viscoelastic. Here, the analysis was also performed in the frequency domain with a linear system.

SALES et al. (2018) considered using VEDs in all three DOFs of an airfoil with cubic hardening springs in pitch and on the control surface. The constitutive viscoelastic relationship was obtained from a fractional derivative model (FDM), an efficient approach to describe viscoelastic behavior in the time domain, accurately representing its fading memory (SALES et al., 2018; CUNHA FILHO et al., 2021). According to the authors, it was the first time that the FDM was applied to a nonlinear aeroelastic model. They found that the VEDs improved the flutter margin and reduced the amplitudes of the LCOs in the post-flutter regime. The intensity of this effect depended on the dimensions of the dampers and the temperature. Thus, VEDs could be employed to control the LCO to some extent, and the influence of temperature must be taken into account.

In a subsequent contribution, SALES et al. (2019) studied a similar three-DOF airfoil. However, the nonlinearity on the control surface was of the free-play type. It was found that adding

VEDs on all DOFs could not only increase the flutter speed and reduce the LCO amplitude but also convert the bifurcation from subcritical, which is not desired in aeronautics, to supercritical. The authors also claim that this is the first time viscoelastic damping was used to change the bifurcation dynamics of a nonlinear airfoil. Moreover, temperature has a strong influence on the performance of the VED.

Instead of the flutter stability gain, LIU, XU and KURTHS (2018) attempted to use sliding mode control to actively suppress vibration of a two-DOF nonlinear airfoil with viscoelastic elements under harmonic load. The nonlinearity was cubic, and fractional derivatives described the discrete viscoelastic elements in both DOF. As a result, higher peak amplitudes were predicted by the fractional approach. In addition, the control strategy was said to perform well. Although this work represented a contribution, the aerodynamic load was considered steady, which is a considerable simplification.

Similarly to the addition of viscoelastic components, LACARBONARA and CETRARO (2011) proposed a vibration absorber that combines viscous and hysteric effects, composed of a Bouc-Wen element in parallel with a dashpot, for a two-DOF airfoil. It was shown that there is no change in the flutter boundary without the dashpot. However, this configuration with the hysteretic component alone could control the oscillation in the post-flutter regime, while increasing damping before flutter.

CHEN et al. (2014) studied the influence of different FDMs and viscoelastic properties on the flutter behavior of a bi-dimensional flag, particularly regarding the flapping frequency and system stability. The research highlights transitions between distinct flapping states and reveals some intriguing dynamics depending on the viscoelastic parameters.

The LMEst has a research tradition in structural dynamics and, particularly, aeroelasticity. (MARTINS, 2014) proposed using VEDs to increase the flutter boundary of a two-DOF airfoil. (CUNHA FILHO, 2019) did the same for a nonlinear airfoil configuration. As the analysis was in the time domain, the author developed a recurrent approach to the viscoelastic fractional derivative model (FDM) used to reduce simulation costs. Furthermore, experiments confirmed the feasibility of the approach.

The work of SILVA (2018) and BORGES (2019) developed a computational algorithm for the analysis of flutter of plate-like wing configurations under unsteady subsonic flow and evaluated the use of a sandwich VED to increase the safety margin of the system in relation to flutter. This tool combines the finite element method (FEM) and the doublet lattice method (DLM) to model the structural and aerodynamic physical aspects of the system, respectively. Subsequently, CARVALHO (2024) adapted this algorithm to include the effect of parametric uncertainty using a stochastic FEM, modeling the sandwich VED with uncertain thickness in the context of the subsonic flutter problem, and performing a robust optimization of the system.

According to what was seen in the literature, the inclusion of nonlinearity in flutter energy harvesting is a fortuitous direction to increase its feasibility, as it creates LCOs that extend the range of operational airspeeds above and below the critical value. However, it might be necessary to control the amplitude of the oscillations, particularly in the post-flutter regime. Some available findings (SALES et al., 2018; SALES et al., 2019), suggest that this could be achieved by VEDs, a versatile passive control approach that can be conveniently incorporated into the system. This new method allows tuning of the damping and stiffness of each DOF individually. Given that the performance of energy harvesting depends on these factors (WANG et al., 2018; TIAN et al., 2021; TIAN et al., 2022), VEDs could also benefit the harvesting itself. Moreover, the physical complexity of the system might require the use of optimization strategies to achieve the desired performance. Strong temperature dependence and parametric variations might indicate the need for a robust optimization to obtain a practical system.

A typical airfoil section, although simple from a structural point of view, allows the study of fundamental aeroelastic phenomena while limiting the complexity of the analysis due to nonlinearities (LEE; PRICE; WONG, 1999; BASTA; GHOMMEM; EMAM, 2021). In fact, the design of an efficient harvester even from two- or three-DOF airfoils has been recognized as a challenge (ABDELKEFI, 2016).

1.2 Objectives

To the best knowledge of the author, so far no work has proposed VEDs for control LCOs from a flutter energy-harvesting perspective. Therefore, the ultimate goal and contribution of this thesis is to evaluate the combination of viscoelastic damping together with free-play and hardening structural nonlinearities to enhance the performance of a flutter energy harvesting device, namely a pitch and plunge (two-DOF) airfoil. In particular, it is expected to increase power output, reduce the airspeed necessary to harvest energy (CWS), and widen the range of airspeeds in which the harvesting can occur. In this regard, the following objectives are established:

- Model a two-DOF airfoil with piezoelectric energy harvesting capability subjected to unsteady aerodynamic load in the time domain;
- Incorporate combined free-play and hardening structural nonlineatires in the model;
- Propose viscoelastic dampers to improve the harvester performance and control the LCO amplitude for a viscoelastic model in time domain;
- Perform a parametric analysis of the nonlinear piezoaeroelastic harvester with viscoelastic damping to identify favorable conditions for energy harvesting;
- Perform the robust multi-objective optimization of the nonlinear piezoaeroelastic harvester with viscoelastic dampers.

The numerical simulations will be performed in MATLAB® environment under academic licenses provided by UFU and FEMTO-ST.

1.3 Thesis structure

This introductory chapter is followed by a discussion on unsteady aerodynamic loads for arbitrary motion in Chapter II, according to potential flow theory. It is shown how these loads can be written as functions of the structural DOF and aerodynamic lag states.

Chapter III develops the equation of motion of the nonlinear airfoil with piezoelectric energy-harvesting feature, following a Lagrangian approach while making use of the aerodynamic forces of the previous chapter.

The incorporation of the VED's in the system is detailed in Chapter IV. Here, the viscoelastic constitutive law is presented according to a recurrent FDM approach. Moreover, the numerical procedure for obtaining the bifurcation diagrams and time responses is described, along with the time integration scheme of the nonlinear equation of motion.

Next, Chapter V presents the fundamental concepts of multiobjective optimization from the deterministic and robust perspectives. The main characteristics of the optimization algorithm used, the Non-Dominated Sorting Genetic Algorithm II (NSGA II) are also discussed. Moreover, due to the cost of the time domain nonlinear analysis with memory effects, a metamodel using a Neural Network (NN) is presented.

The numerical results are presented and discussed in Chapter VI. Finally, Chapter VII presents the concluding remarks and suggestions for future work.

CHAPTER II

UNSTEADY AERODYNAMICS

The unsteady aerodynamic load formulation from fundamental concepts is presented in this chapter. First it is shown how the so called Wagner function can be used to correct the quasi-steady approach followed by a non-exhaustive derivation of the unsteady lift and moment loads as a function of the well-known Theodorsen function for the case of harmonic movement. Finally, Wagner and Theodorsen functions are be combined to obtain arbitrary motion of the airfoil, following the Duhamel approach.

A representative aerodynamics model is necessary for the wind-driven energy harvester. Three types of methods are available: steady, quasi-steady, and unsteady. The first option is unsuitable for a dynamic analysis since it cannot account for the variation of lift and moment with time. A straightforward solution to this matter is the quasi-steady approach, which uses the steady formulation to compute instantaneous variations in lift and moment. However, in doing so, it disregards relevant frequency-dependent effects (WRIGHT; Cooper, 2014), making the technique unsuitable for flutter analysis. The unsteady approach can overcome this limitation. Indeed, when computing the flutter speed of a pitch and plunge airfoil, ABDELKEFI et al. (2013) demonstrated that the unsteady theory predicted a flutter speed closer to the experimentally measured value than the quasi-steady theory. Therefore, an unsteady approach is preferred to describe the time-varying aerodynamic load.

2.1 Fundamental Aerodynamics

It is instructive to start with the fundamental concept of a steady aerodynamic load. Taking into account a uniform horizontal flow of speed V, the pitch angle θ is the angle of attack. Due to airflow, a pressure distribution develops around the airfoil (Fig. 2.1), whose resulting force is located at a given position along the chord. This point is the center of pressure (CP), which varies with the angle of attack (WRIGHT; Cooper, 2014), thus increasing the complexity of the analysis. To overcome this, the resultant force is placed at an arbitrary reference point where a moment M is added so that the new representation is statically equivalent to the original setup. The force is decomposed in two orthogonal components, the lift L and the drag D, while M is termed pitching moment. For the proposed FEH device, fixed on the ground, the drag is of no interest, as it does not influence the dynamical behavior of the system.

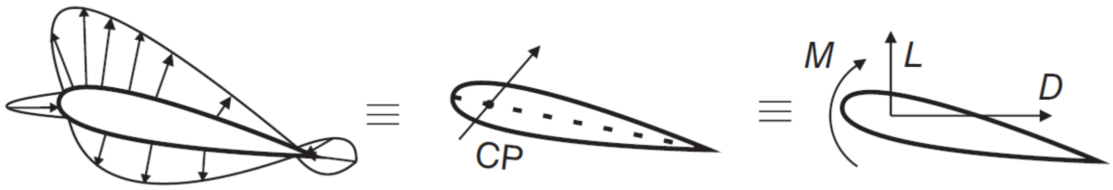

Figure 2.1 – Equivalent representations of an aerodynamic load on an airfoil (WRIGHT; Cooper, 2014).

The lift and moment can be written as function of corresponding non-dimensional coefficients, C_L and C_M, as

$$L = \left(\frac{1}{2}\rho_\infty V^2 c\right) C_L \tag{2.1}$$

and

$$M = \left(\frac{1}{2}\rho_\infty V^2 c^2\right) C_M \tag{2.2}$$

respectively (BISPLINGHOFF; ASHLEY, 1975), where ρ_∞ is the air density and c is the chord of the airfoil. The coefficient C_L is a function of the angle of attack, displaying a linear behavior before the region close to the stall condition is reached (Fig. 2.2), in which the flow separates itself from the airfoil (WRIGHT; Cooper, 2014). For a symmetric airfoil, as considered in this thesis, there is no lift at a zero angle of attack. Hence, the relationship between C_L and θ is:

$$C_L = \hat{a}\theta \tag{2.3}$$

where $\hat{a}$ the angular coefficient of the linear part, termed the lift curve slope. In turn, the coefficient C_M can be made independent of the angle of attack by placing L and D at the aerodynamic center, located at 0.25 of the chord (WRIGHT; Cooper, 2014). Another trait of the symmetric airfoil is that the moment coefficient is zero for zero angle of attack, just like the lift (WRIGHT; Cooper, 2014).

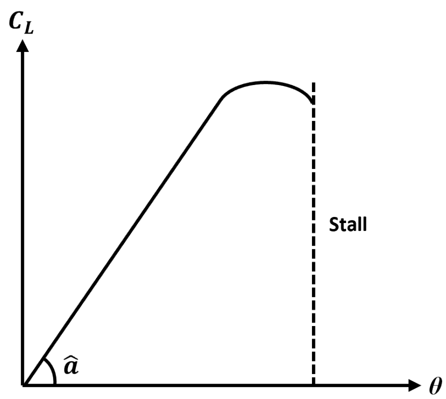

Figure 2.2 – C_L as function of the angle of attack for a symmetric airfoil.

2.2 Wagner function

By substituting Eq. 2.3 in Eq. 2.1 one obtains a direct relation between the variation of the angle of attack and the corresponding change in lift:

$$\Delta L = \frac{1}{2}\rho_{\infty}V^2 c\hat{a}\Delta\theta \tag{2.4}$$

which is assumed to be instantaneous, as a step (Fig. 2.3). This is the behavior predicted by the quasi-steady approach. Although straightforward, the method does not provide a completely accurate representation, as in practice there is a considerable delay before the lift can reach the value predicted by Eq. 2.4. To deal with this matter, the following correction can be made:

$$\Delta L = \frac{1}{2}\rho_{\infty}V^2 c\hat{a}\Delta\theta\phi(s) \tag{2.5}$$

where $\phi(s)$ is the so-called Wagner function (WAGNER, 1925), and $s = Vt/b$ is the non-dimensional time, representing the number of semi-chords b traveled by the flow after it leaves the airfoil, $b = c/2$. It is a challenge to efficiently compute the exact form of the Wagner function, which motivates the development of approximations (DAWNSON; BRUNTON, 2021). One common option is to write $\phi(s)$ as presented by JONES (1940) and SEARS (1940):

$$\phi\left(s\right) \cong 1 - c_1 e^{-c_2 s} - c_3 e^{-c_4 s} \tag{2.6}$$

where $c_1 = 0.165$, $c_2 = 0.0455$, $c_3 = 0.0335$, $c_4 = 0.3$, whose accuracy is higher for intermediate values of s (BISPLINGHOFF; ASHLEY, 1975).

A comprehensive derivation of $\phi(s)$ in its exact form can be found in DAWNSON and BRUNTON (2021). Moreover, it is worth mentioning that the exact formulation of the Wagner function has no representation in the Laplace domain such that it can not be used in control problems (MARTINS, 2014). Equation 2.6 does not have this limitation.

Using Eq. 2.6 to compute the change in lift due to a variation in the angle of attack, it is evident that, although it predicts a sudden increase in lift, it is succeeded by an asymptotic increase to the quasi-steady unitary value (Fig. 2.3). It will be shown that this effect results in a difference when the harmonic response of the airfoil is considered.

2.3 Harmonic lift and moment

2.3.1 Direct convolution approach

Equation 2.5 can be rewritten in terms of the normal flow component, the downwash $w = V\sin\Delta\theta$. If $\Delta\theta$ is small, then the approximation $w \approx V\Delta\theta$ holds, thus Eq. 2.5 becomes:

$$\Delta L = \frac{1}{2}\rho_{\infty}V c\hat{a} w\phi(s) \tag{2.7}$$

showing that the change in lift can be seen as a function of a step change in the downwash corrected by the Wagner function. Hence, if the displacement time history of the angle of attack

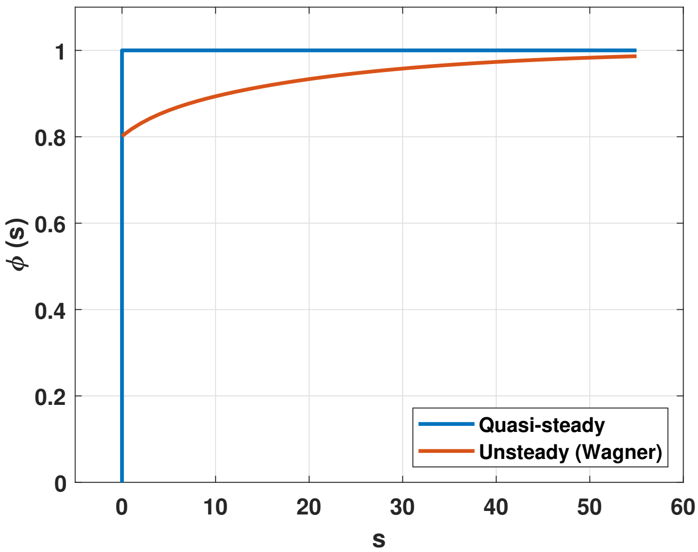

Figure 2.3 – Wagner function compared to the quasi-steady approach.

is known, it is possible to predict the arbitrary lift of the airfoil from a convolution operation, as a superposition of downwash steps. In this context, the lift is written as

$$L\left(s\right)=\frac{1}{2}\rho_{\infty}Vc\hat{a}\left(w_0+\int\limits_{s_0=0}^{s}\phi\left(s-s_0\right)\frac{dw}{ds_0}ds_0\right) \tag{2.8}$$

Assuming a sinusoidal variation for the angle of attack, $\theta=\bar{\theta}\sin\omega t$, then Eq. 2.8 can be used to compute the corresponding harmonic lift. From Fig. 2.4, it is evident that the quasi-steady approach overestimates lift and produces an advanced signal in relation to the unsteady response. In this figure, $V=10$ m/s, $c=1$ m, $\bar{\theta}=1$ rad and $k=0.2$. The latter term is known as the reduced frequency, defined by $k=(\omega b)/V$.

For complex motion cases, usually the time history of the angle of attack is not available. In fact, obtain the time response itself of the dofs might be the ultimate goal. To deal with an airfoil in arbitrary motion first it will be investigated an alternative way to obtain the harmonic response of lift, one that does not relies on expensive convolution operations.

2.3.2 Theodorsen approach

By computing the resultant pressure difference ΔP between the upper surface and the lower surface of the wing, the aerodynamic load may be obtained from the following expressions (BISPLINGHOFF; ASHLEY, 1975):

$$\bar{L}=\int\limits_{-b}^{b}\Delta P dx \tag{2.9}$$

$$\bar{M}=\int\limits_{-b}^{b}\Delta P x dx \tag{2.10}$$

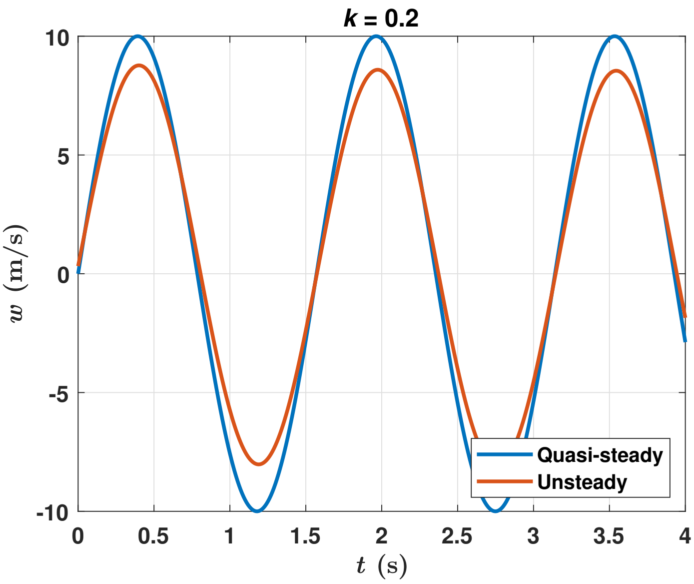

Figure 2.4 – Downwash for an harmonic pitch according to the quasi-steady and unsteady approaches.

where lift and moment are measured at the same reference point and expressed per unit length of the span l, such that: $\bar{L} = L/l$, $\bar{M} = M/l$. Thus, the problem assumes the form of Eq. 2.9 and Eq. 2.10.

To complete the task at hand, one must describe the pressure difference. From the assumptions of incompressible, inviscid and irrotational flow, the Navier-Stokes momentum equations are converted into the modified Bernoulli equation (BLAIR, 1992):

$$\frac{\partial \varphi}{\partial t} + \frac{{q_\infty}^2}{2} + \int \frac{dP}{\rho_\infty} = 0 \tag{2.11}$$

where q_∞ is the dynamic pressure and φ stands for the velocity potential. As the irrotational assumption means that the vorticity must be zero at every point in the flow, $\nabla \times \mathbf{V} = 0$, there must be a scalar function $\varphi(x, y, z)$ satisfying the identity $\nabla \times (\nabla\varphi) = 0$, such that (ANDERSON JUNIOR, 2011):

$$\mathbf{V} = \nabla\varphi \tag{2.12}$$

This scalar function is the velocity potential. It substantially reduces the complexity of the analysis since the velocity components of the flow are replaced by a single unknown function (ANDERSON JUNIOR, 2011).

To further simplify the analysis, it is possible to linearize Eq. 2.11 from the following isentropic equation of state:

$$P = P_0 \left(\frac{\rho}{\rho_0}\right)^{\varrho} \tag{2.13}$$

where ϱ is the ratio of the specific heat at constant pressure to that at constant volume. The procedure results in the equation for the pressure difference (BLAIR, 1992):

$$\Delta P = -\rho_\infty \left(\frac{\partial \varphi}{\partial t} + V\frac{\partial \varphi}{\partial x}\right) \tag{2.14}$$

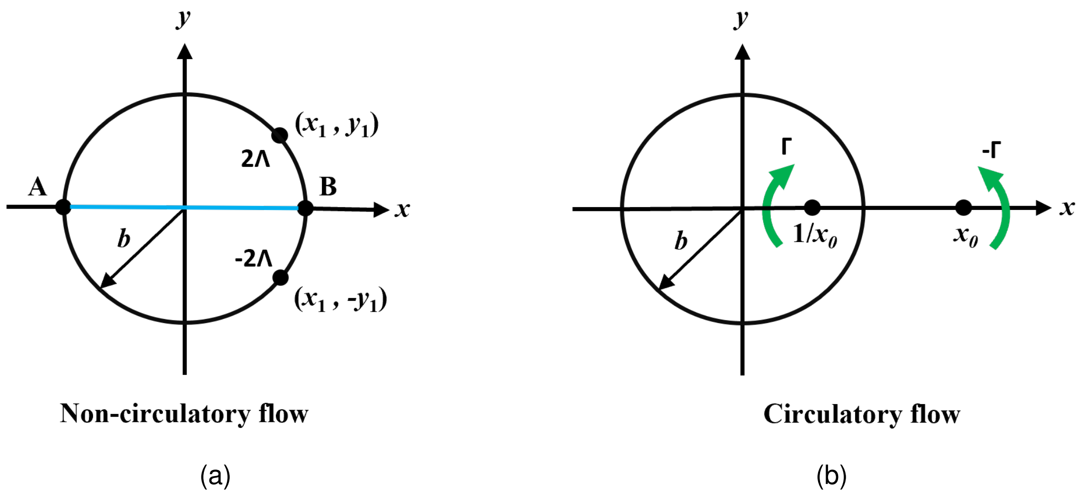

Figure 2.5 – Non-circulatory (a) and circulatory (b) flow components proposed by THEODORSEN (1935) according to a conformal representation of the airfoil.

The step-by-step derivation of Eq. 2.14 is found in SILVA (2018) and BLAIR (1992). Although the assumptions involved might be seen as major simplifications, they are deemed sufficient from an aeroelastic perspective, given that the main concern is the normal stress exerted by the flow on the lifting surface (BISPLINGHOFF; ASHLEY, 1975).

The remaining procedure to evaluate the pressure difference in the form of Eq. 2.14 is to obtain φ. When describing the lift and moment of an airfoil in harmonic motion, THEODORSEN (1935) considered the flow as a combination of two components, termed circulatory and non-circulatory, and derived the resulting velocity potential. Both components are generated from the so-called elementary incompressible flows. The non-circulatory flow is produced by a double source and a double sink, located at the points (x_1, y_1) and $(x_1, -y_1)$, respectively, as illustrated in Fig. 2.5, while the circulatory flow component is created by vortexes of opposite strength Γ at the positions $1/x_0$ and x_0, (Fig. 2.5). To facilitate the derivation of the velocity potential, THEODORSEN (1935) used the Joukowsky conformal transformation to map the airfoil into a circle of unitary radius b.

The elementary flows are idealized theoretical flows, arbitrarily conceived for classical aerodynamic models. In a source flow, the streamlines are straight, originating from a given point, and the velocity varies inversely with the distance to the origin (ANDERSON JUNIOR, 2011)(Fig. 2.6a). If the streamlines are oriented in the opposite sense, the flow is a sink (Fig. 2.6b). In turn, a vortex is composed of circular concentric streamlines where the flow speed is constant at a streamline but varies from one to the other, also inversely with the distance from the center (ANDERSON JUNIOR, 2011)(Fig. 2.6c). The velocity potentials associated with the source, sink and vortex elementary flows are, respectively, (ANDERSON JUNIOR, 2011):

$$\varphi_{source} = \frac{\Lambda}{2\pi} \ln(r) \tag{2.15}$$

$$\varphi_{sink} = -\frac{\Lambda}{2\pi} \ln(r) \tag{2.16}$$

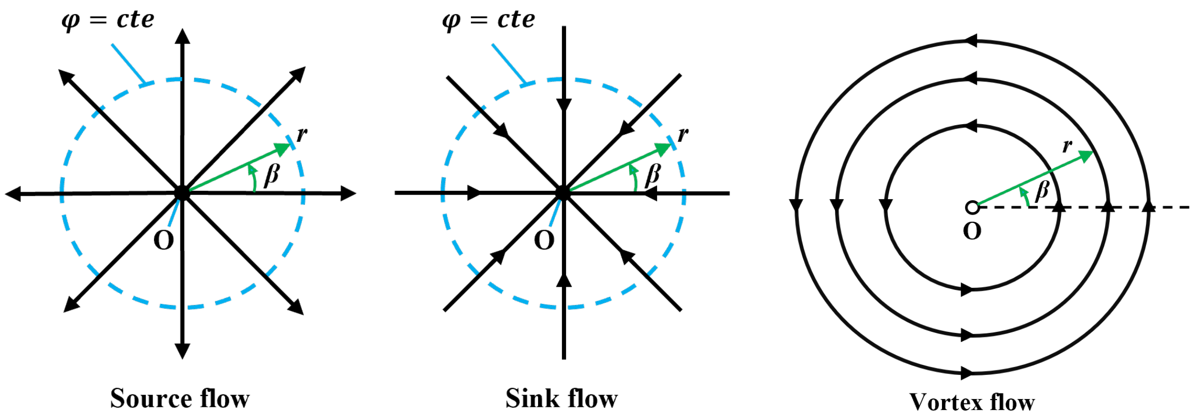

(a) (b) (c)

Figure 2.6 – Elementary incompressible flows: source a, sink b, and vortex c.

$$\varphi_{vortex} = -\frac{\Gamma}{2\pi}\beta \tag{2.17}$$

where Λ is the strength of the source or sink and Γ is the vortex strength. Moreover, r and β are the polar coordinates defined in Fig. 2.5.

Figure 2.7 illustrates how elementary source and sink flows are superimposed with a steady flow to predict flow around a Rankine oval, illustrating how elementary flows can be combined to represent more complex flow patterns.

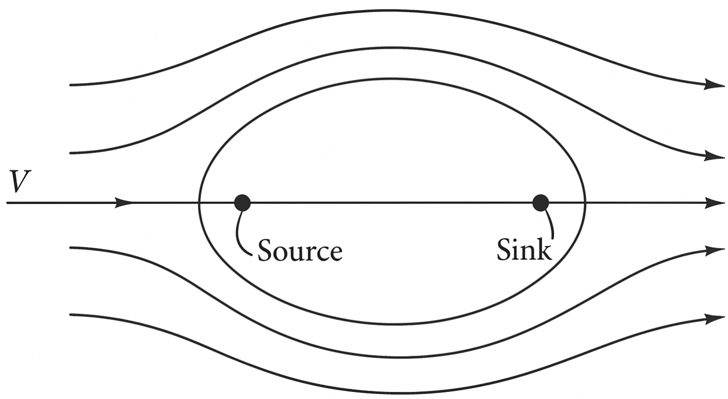

Figure 2.7 – Flow over a Rankine oval by the superposition of a source and sink pair with a uniform flow (adapted from ANDERSON JUNIOR (2011)).

Based on Eq. 2.16 to Eq. 2.17, and on the principle of superposition, THEODORSEN (1935) determined the resultant velocity potential for the non-circulatory and circulatory flows components for the configuration of Fig. 2.5. The author then used the velocity potential to determine the pressure difference in Eq. 2.14 and, finally, the unsteady lift and moment of Eq. 2.9 and Eq. 2.10. The circulatory and non-circulatory components of lift and moment, denoted respectively, by the subscripts c and nc are:

$$\bar{L} = L_{nc} + L_c \tag{2.18}$$

$$\bar{M} = M_{nc} + M_c \tag{2.19}$$

where each contribution, per unit length of the span l, is found to be (THEODORSEN, 1935; SILVA et al., 2018):

$$L_{nc} = \pi\rho b^2 \left(\ddot{h} + V\dot{\theta} - ba\ddot{\theta}\right) \tag{2.20}$$

$$L_c = 2\pi\rho V b C\left(k\right) w(t) \tag{2.21}$$

$$M_{nc} = \pi b^2 \rho \left[V\dot{h} + ba\ddot{h} + V^2\theta - b^2\left(\frac{1}{8} + a^2\right)\ddot{\theta}\right] \tag{2.22}$$

$$M_c = -\pi V\rho b^2 w\left(t\right) + b\left(a + \frac{1}{2}\right) 2\pi\rho V b C\left(k\right) w\left(t\right) \tag{2.23}$$

where a specifies the dimensionless location of the elastic axis of the airfoil. The term $w(t)$ in the above equations is the downwash at $3/4$ of the chord, given as (SILVESTRE; LUCKNER, 2015):

$$w(t) = \dot{h} + V\theta + b\left(\frac{1}{2} - a\right)\dot{\theta} \tag{2.24}$$

Furthermore, $C(k)$ denotes the well-known Theodorsen function, dependent on the reduced frequency k. This function corrects the quasi-steady sinusoidal lift of the airfoil in terms of phase and amplitude to give the proper unsteady behavior (WRIGHT; Cooper, 2014). Indeed, by imposing $C(k) = 1$, in Eq. 2.18 and Eq. 2.19, one arrives at the quasi-steady solution for harmonic lift and moment. The Theodorsen function can be defined in therms of Hankel functions of the second kind and j^{th} order, $H_j^{(2)}(k)$, $j = 0, 1$, being a complex number (BISPLINGHOFF; ASHLEY, 1975; ERTURK; INMAN, 2011):

$$C(k) = \frac{H_1^{(2)}(k)}{H_1^{(2)}(k) + iH_0^{(2)}(k)} \tag{2.25}$$

where the Hankel functions are usually provided in several numeric libraries.

It is important to note that Eq. 2.18 and Eq. 2.19 are only valid for a harmonic response. Although suitable for finding the flutter speed in the frequency domain, they cannot be used to describe the time-domain behavior of the system in their current form. The only exception being the critical flutter condition, where the response is harmonic. However, in Section 2.4 it will be shown how the harmonic solution can be modified to obtain a generic aerodynamic load.

2.4 Arbitrary lift and moment

Given the possibility of complex and even aperiodic response, the time domain analysis of the nonlinear aeroelastic system requires the prediction of arbitrary lift and moment. This non-trivial task can be addressed by replacing the term $C(k)w(t)$ in the circulatory lift and moment expressions, Eq. 2.21 and Eq. 2.23, by the Duhamel formulation (LI; GUO; XIANG, 2010):

$$C\left(k\right)w\left(t\right)=w\left(0\right)\phi\left(s\right)+\int_{0}^{s}\frac{\partial w\left(\xi\right)}{\partial\xi}\phi\left(s-\xi\right)d\xi \tag{2.26}$$

with ξ being the dummy integration variable. Assuming $w(0)=0$ as the initial condition, the first term of Eq. 2.26 is eliminated. Next, applying the approximation for the Wagner function, Eq. 2.6 in Eq. 2.26, yields:

$$C\left(k\right)w\left(t\right)=w\left(t\right)+\lambda_1+\lambda_2 \tag{2.27}$$

where the terms $\lambda_1(t)$ and $\lambda_2(t)$ are aerodynamic lag states related to the delay between the variation of the downwash and lift, described by the following relations (SILVESTRE; LUCKNER, 2015):

$$\dot{\lambda}_1=-0.041\left(\frac{V}{b}\right)\lambda_1-0.165\dot{w} \tag{2.28}$$

$$\dot{\lambda}_2=-0.032\left(\frac{V}{b}\right)\lambda_2-0.335\dot{w} \tag{2.29}$$

which can be written in matrix form as:

$$\begin{Bmatrix}\dot{\lambda}_1\\ \dot{\lambda}_2\end{Bmatrix}=\mathbf{b_1}\begin{Bmatrix}\ddot{h}\\ \ddot{\theta}\end{Bmatrix}+\mathbf{b_2}\begin{Bmatrix}\dot{h}\\ \dot{\theta}\end{Bmatrix}+\mathbf{b_3}\begin{Bmatrix}h\\ \theta\end{Bmatrix}+\mathbf{b_4}\begin{Bmatrix}\lambda_1\\ \lambda_2\end{Bmatrix} \tag{2.30}$$

Finally, substituting Eq. 2.27 in Eq. 2.18 and Eq. 2.19 the lift and moment are expressed as functions of the pitch and plunge dofs and the lag states λ_1 and λ_2:

$$\begin{Bmatrix}-L\\ M\end{Bmatrix}=\boldsymbol{a_1}\begin{Bmatrix}\ddot{h}\\ \ddot{\theta}\end{Bmatrix}+\boldsymbol{a_2}\begin{Bmatrix}\dot{h}\\ \dot{\theta}\end{Bmatrix}+\boldsymbol{a_3}\begin{Bmatrix}h\\ \theta\end{Bmatrix}+\boldsymbol{a_4}\begin{Bmatrix}\lambda_1\\ \lambda_2\end{Bmatrix} \tag{2.31}$$

Equation 2.31 can be conveniently incorporated in the equation of motion, as will be shown in Chapter III. Furthermore, the aerodynamic matrices $\boldsymbol{a_j}$ and $\mathbf{b}_j$ $(j=1,2,3,4)$ are provided in the Appendix A. Except from $\boldsymbol{a_1}$, $\mathbf{b_1}$ and $\mathbf{b_3}$ all aerodynamic matrices depend on the airspeed V.

CHAPTER III

NONLINEAR PIEZOAEROELASTIC MODEL

In this chapter, the equation of motion of the aeroelastic system with nonlinear springs and piezoelectric energy harvesting feature is derived from the Lagrange equations. Next, it is shown how the unsteady aerodynamics is incorporated in the equation of motion. Finally, the state-space representation of the system in its linear configuration is presented, as it can be used to obtain the corresponding flutter speed.

3.1 Equation of motion

The aeroelastic system considered in this work is a bidimensional typical section, as it provides reasonable physical information on the nonlinear problem while restricting the complexity of the analysis ((LEE; PRICE; WONG, 1999; BASTA; GHOMMEM; EMAM, 2021)). Therefore, a lumped parameter model is chosen (Fig. 3.1). It consists of a rigid pitch (θ) and plunge (h) airfoil subjected to a flow of airspeed V. The NACA 0012 airfoil profile is defined by its semi-chord b and the non-dimensional parameters a and x_θ. The former specifies the location of the elastic axis (EA) relative to the position of the mid chord (B), while the latter locates the center of gravity (CG) relative to the EA. Both pitch and plunge dofs are connected to discrete nonlinear stiffness elements, respectively k_θ^{nl} and k_h^{nl}, and linear viscous dampers, c_θ and c_h, respectively. The parameters θ_{fp} and h_{fp} denote the total free-play gap of each nonlinear spring.

The energy harvesting feature is obtained by adding a piezoelectric element to the plunge dof, where term α represents the electromechanical coupling. In this context, after the flutter speed is reached, the airfoil oscillates as an LCO, converting part of the kinetic energy into electricity through the direct piezoelectric effect. The generated power is dissipated by the resistor R.

As demonstrated by ERTURK and INMAN (2011), the extended Hamilton principle can be used to obtain the Lagrange equations for each dof q_j, in the following form:

$$\frac{d}{dt}\left(\frac{\partial T_k}{\partial \dot{q}_j}\right) - \left(\frac{\partial T_k}{\partial q_j}\right) + \left(\frac{\partial U}{\partial q_j}\right) - \left(\frac{\partial W_{ie}}{\partial q_j}\right) = Q_j \tag{3.1}$$

where T_k, U and W_{ie} are the kinetic, potential and internal electric energies, respectively, while Q_j represents the non-conservative forces.

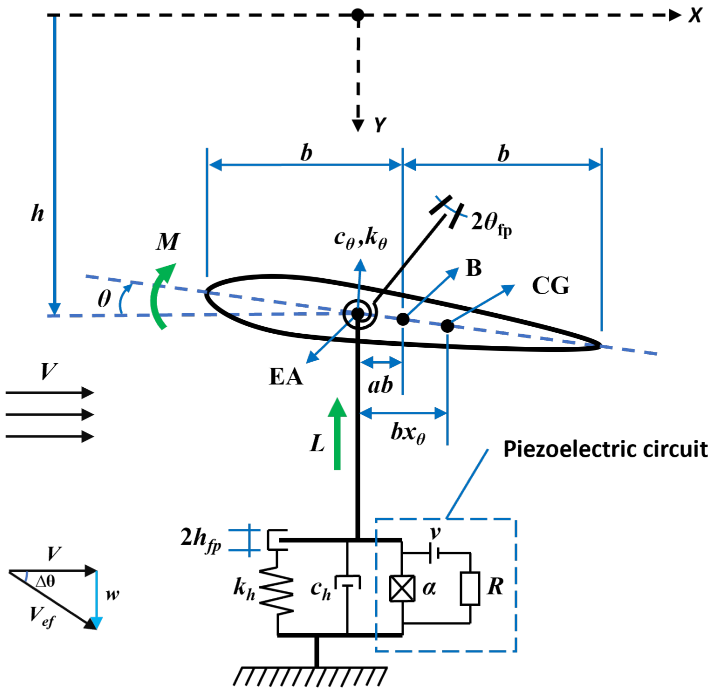

Figure 3.1 – Nonlinear pitch and plunge airfoil with piezoelectric circuit.

Starting with T_k, if the mass per the chord-wise length of the airfoil is ρ, the kinetic energy is:

$$T_k = \frac{1}{2}\int \rho(\dot{y})^2 dx \tag{3.2}$$

where y denotes the vertical displacement of an arbitrary point on the airfoil. As θ is assumed small, the kinetic energy of the horizontal displacement along X is negligible. From Fig. 3.1, y can be written in terms of h, θ and the distance x between the EA and the arbitrary point:

$$y = h + x\theta \tag{3.3}$$

By substituting Eq. 3.3 in Eq. 3.2, the kinetic energy becomes as follows:

$$T_k = \frac{1}{2}\left(\left(\dot{h}\right)^2\int \rho dx + 2\dot{h}\dot{\theta}\int \rho x dx + \left(\dot{\theta}\right)^2\int \rho x^2 dx\right) \tag{3.4}$$

where it is important to consider the physical meaning of the integral terms. From the specific mass ρ, the airfoil mass is $m = \int dm = \int \rho dx$, while $S = \int \rho x dx$ is the first mass moment and $I = \int \rho x^2 dx$ is the moment of inertia. Thus, Eq. 3.4 can be simplified:

$$T_k = \frac{1}{2}m\left(\dot{h}\right)^2 + S\dot{h}\dot{\theta} + \frac{1}{2}I\left(\dot{\theta}\right)^2 \tag{3.5}$$

In addition to the mass of the airfoil itself, the mass m_s of a translating supporting structure must also be considered when computing the kinetic energy:

$$T_k = \frac{1}{2}\left(m + m_s\right)\left(\dot{h}\right)^2 + S\dot{h}\dot{\theta} + \frac{1}{2}I\left(\dot{\theta}\right)^2 \tag{3.6}$$

If one assumes that all the mass of the airfoil is concentrated at the CG, $S = mx_\theta b$ and $I = mr_\theta^2$, such that:

$$T_k = \frac{1}{2}m_t\left(\dot{h}\right)^2 + mbx_\theta\dot{h}\dot{\theta} + \frac{1}{2}mr_\theta{}^2\left(\dot{\theta}\right)^2 \tag{3.7}$$

where r_θ is the radius of gyration and x_θ is the non-dimensional distance between the elastic axis and the CG. The term m_t stands for the sum $m + m_s$.

As previously discussed in the Introduction, the combination of free-play and hardening nonlinearities in stiffness terms favors FEH. Therefore, in this work, both are included in the pitch and plunge springs. To obtain a compact representation in the equation of motion, the nonlinear stiffness terms k_χ^{nl} are written as the ratio between a nonlinear elastic force $F_\chi^{nl}(\chi)$ and the correspondent generic displacement χ, representing either h or θ:

$$k_\chi^{nl} = \frac{F_\chi^{nl}(\chi)}{\chi} \tag{3.8}$$

in which the force assumes the following form:

$$F_\chi^{nl}(\chi) = \begin{cases} k_\chi^l \left(a_0{}^\chi \left(\chi - \chi_{fp}\right) + a_1{}^\chi (\chi - \chi_{fp})^3 \right) & \chi > \chi_{fp} \\ 0 & -\chi_{fp} \leq \chi \leq \chi_{fp} \\ k_\chi^l \left(a_0{}^\chi \left(\chi + \chi_{fp}\right) + a_1{}^\chi (\chi + \chi_{fp})^3 \right) & \chi < -\chi_{fp} \end{cases} \tag{3.9}$$

where χ_{fp} denotes the semi free-play gap. The coefficients a_0^χ and a_1^χ determine the intensity of the linear and hardening contributions, respectively. The linear stiffness is k_χ^l. For plunge, $k_h^l = m_t\omega_h^2$, and, for pitch, $k_\theta^l = I\omega_\theta^2$, where ω_h and ω_θ are the corresponding uncoupled natural frequencies.

Figure 3.2 represents the elastic force F_k for the linear and different nonlinear stiffness configurations of Eq. 3.9 considering $k_\chi^l = 1$, unitary coefficients ($a_0{}^\chi = a_1{}^\chi = 1$) and unitary free-play gap ($\chi_{fp} = 1$). The idea is to favor energy harvesting by the lack of stiffness for a given vibration amplitude range above which the hardening effect helps to control the vibration level in the form of an LCO. Hence, persistent power generation could be achieved at a constrained vibration amplitude.

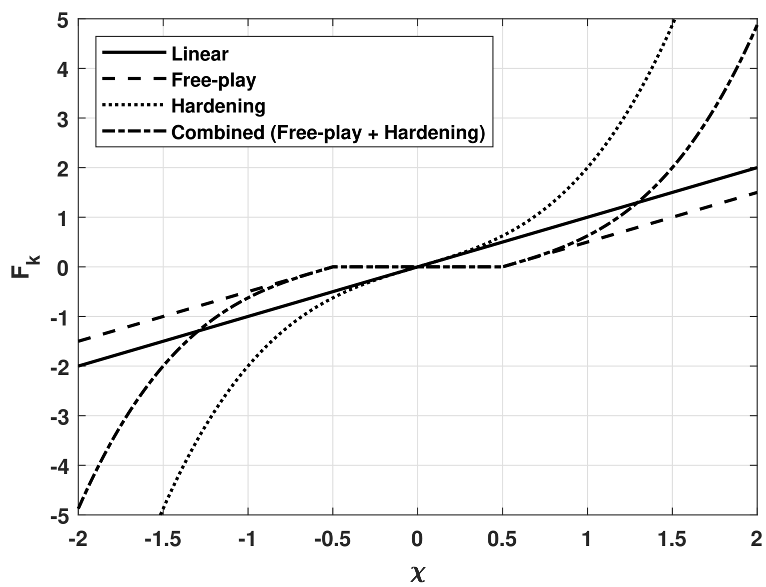

Figure 3.2 – Elastic force as function of a generic displacement for the linear and nonlinear cases.

The potential energy associated with the piezoelectric effect and the pitch and plunge nonlinear springs is:

$$U = \int k_h^{nl} h dh + \int k_\theta^{nl} \theta d\theta - \int \alpha v dh \tag{3.10}$$

whose integration yields:

$$\begin{aligned} U = k_h^l \left\{ \frac{a_0^h}{2} \left[(h - h_{fp})^2 - (h_{fp})^2 \right] + \frac{a_1^h}{4} \left[(h - h_{fp})^4 - (h_{fp})^4 \right] \right\} + \\ k_\theta^l \left\{ \frac{a_0^\theta}{2} \left[(\theta - \theta_{fp})^2 - (\theta_{fp})^2 \right] + \frac{a_1^\theta}{4} \left[(\theta - \theta_{fp})^4 - (\theta_{fp})^4 \right] \right\} - \alpha v h \end{aligned} \tag{3.11}$$

After defining the kinetic and potential energies, it is necessary to describe the internal electric energy W_{ie}. From the equivalent capacitance C_{eq} of the piezoelectric material and the electromechanical coupling term α, W_{ie} is given by:

$$W_{ie} = \frac{1}{2} C_{eq} v^2 + \alpha v h \tag{3.12}$$

The last terms required to evaluate Eq. 3.1 are the non-conservative forces Q_j for each dof. For pitch and plunge, these arise from the structural damping and aerodynamic loads, L being the lift, and M the pitching moment:

$$Q_h = -L - c_h \dot{h} \tag{3.13}$$

$$Q_\theta = M - c_\theta \dot{\theta} \tag{3.14}$$

It is worth mentioning that the negative sign of L comes from the fact that this force points upward, in the opposite direction of h (Fig. 3.1). For the voltage, the non-conservative force comes from the electric charge $\bar{q}$:

$$Q_v = \bar{q} \tag{3.15}$$

Next, substituting equations 3.7, 3.10, 3.12, 3.13, 3.14, and 3.15 into Eq. 3.1 for each dof yields the following:

$$m_t \ddot{h} + S\ddot{\theta} + c_h \dot{h} + k_h^{nl} h - \alpha v = -L \tag{3.16}$$

$$S\ddot{h} + I\ddot{\theta} + c_\theta \dot{\theta} + k_\theta^{nl} \theta = M \tag{3.17}$$

$$C_{eq} v + \alpha h + \bar{q} = 0 \tag{3.18}$$

Equation 3.18 is written in the form of an initial value problem by differentiating it with respect to time. Keeping in mind that $\dot{\bar{q}} = \frac{v}{R}$, it becomes:

$$C_{eq} \dot{v} + \alpha \dot{h} + \frac{v}{R} = 0 \tag{3.19}$$

which together with Eq. 3.16 and Eq. 3.17 govern the dynamics of the nonlinear piezoaeroelastic system. It is convenient to write these equations in matrix form so that a single expression is obtained. Furthermore, this procedure will facilitate the incorporation of the unsteady aerodynamic load, Eq. 2.31, which is also in matrix form. Thus, proceeding in this way, one obtains:

$$\begin{bmatrix} m_t & S & 0 \\ S & I & 0 \\ 0 & 0 & 0 \end{bmatrix} \begin{Bmatrix} \ddot{h} \\ \ddot{\theta} \\ \ddot{v} \end{Bmatrix} + \begin{bmatrix} c_h & 0 & 0 \\ 0 & c_\theta & 0 \\ \alpha & 0 & C_{eq} \end{bmatrix} \begin{Bmatrix} \dot{h} \\ \dot{\theta} \\ \dot{v} \end{Bmatrix} + \begin{bmatrix} k_h^{nl} & 0 & -\alpha \\ 0 & k_\theta^{nl} & 0 \\ 0 & 0 & R^{-1} \end{bmatrix} \begin{Bmatrix} h \\ \theta \\ v \end{Bmatrix} = \begin{Bmatrix} -L \\ M \\ 0 \end{Bmatrix} \tag{3.20}$$

where is evident the electromechanical coupling between plunge (h) and voltage (v), represented by the terms $-\alpha v$ and $\alpha \dot{h}$.

Next, $-L$ and M are substituted from Eq.2.31 in Eq. 3.20, resulting in:

$$\begin{bmatrix} \tilde{\mathbf{M}} & \mathbf{0} \\ \mathbf{0} & 0 \end{bmatrix} \begin{Bmatrix} \ddot{h} \\ \ddot{\theta} \\ \ddot{v} \end{Bmatrix} + \begin{bmatrix} \tilde{\mathbf{C}} & \mathbf{0} \\ \mathbf{H} & C_{eq} \end{bmatrix} \begin{Bmatrix} \dot{h} \\ \dot{\theta} \\ \dot{v} \end{Bmatrix} + \begin{bmatrix} \tilde{\mathbf{K}}^{\mathbf{nl}} & -\mathbf{H}^{\mathsf{T}} \\ \mathbf{0} & R^{-1} \end{bmatrix} \begin{Bmatrix} h \\ \theta \\ v \end{Bmatrix} = \begin{bmatrix} \boldsymbol{a_4} & \mathbf{0} \\ \mathbf{0} & 0 \end{bmatrix} \begin{Bmatrix} \lambda_1 \\ \lambda_2 \\ 0 \end{Bmatrix} \tag{3.21}$$

where $\mathbf{H} = \begin{Bmatrix} \alpha & 0 \end{Bmatrix}$ is the electromechanical vector and the aeroelastic matrices of mass $\left(\tilde{\mathbf{M}}\right)$, damping $\left(\tilde{\mathbf{C}}\right)$ and stiffness $\left(\tilde{\mathbf{K}}^{\mathbf{nl}}\right)$ are:

$$\tilde{\mathbf{M}} = \begin{bmatrix} m_t & S \\ S & I \end{bmatrix} - \boldsymbol{a_1} \tag{3.22}$$

$$\tilde{\mathbf{C}} = \begin{bmatrix} c_h & 0 \\ 0 & c_\theta \end{bmatrix} - \boldsymbol{a_2} \tag{3.23}$$

$$\tilde{\mathbf{K}}^{\mathbf{nl}} = \begin{bmatrix} k_h^{nl} & 0 \\ 0 & k_\theta^{nl} \end{bmatrix} - \boldsymbol{a_3} \tag{3.24}$$

respectively.

Given the dependency on the aerodynamic lag states λ_1 and λ_2, it is necessary to rewrite Eq. 3.21 as a system of equations that includes them. This operation will make the numerical integration of the equation of motion a straightforward process. By substituting Eq. 2.30 and rearranging terms one obtains the following expression:

$$\begin{bmatrix} \tilde{\mathbf{M}} & \mathbf{0} & \mathbf{0} \\ -\mathbf{b_1} & \mathbf{0} & \mathbf{0} \\ \mathbf{0} & \mathbf{0} & 0 \end{bmatrix} \ddot{\mathbf{q}} + \begin{bmatrix} \tilde{\mathbf{C}} & \mathbf{0} & \mathbf{0} \\ -\mathbf{b_2} & \mathbf{I} & \mathbf{0} \\ \mathbf{H} & \mathbf{0} & C_{eq} \end{bmatrix} \dot{\mathbf{q}} + \begin{bmatrix} \tilde{\mathbf{K}}^{\mathbf{nl}} & -\boldsymbol{a_4} & -\mathbf{H}^{\mathsf{T}} \\ -\mathbf{b_3} & -\mathbf{b_4} & \mathbf{0} \\ \mathbf{0} & \mathbf{0} & R^{-1} \end{bmatrix} \mathbf{q} = \mathbf{0} \tag{3.25}$$

where $\mathbf{q} = \begin{Bmatrix} h & \theta & \lambda_1 & \lambda_2 & v \end{Bmatrix}^{\mathsf{T}}$. Moreover, as described in Chapter II, the matrices $\boldsymbol{a_j}$ and $\mathbf{b}_j$ ($j = 1, ..., 4$) are provided in appendix A.

Finally, Eq. 3.25 is rewritten in a more compact form:

$$\bar{\mathbf{M}}\ddot{\mathbf{q}} + \bar{\mathbf{C}}\left(V\right)\dot{\mathbf{q}} + \bar{\mathbf{K}}^{\mathbf{nl}}\left(V, t\right)\mathbf{q} = \mathbf{0} \tag{3.26}$$

to yield the equation of motion of the proposed nonlinear FEH device. Due to the dependency of $\boldsymbol{a_2}$, $\boldsymbol{a_3}$, $\boldsymbol{a_4}$, $\mathbf{b_2}$ and $\mathbf{b_4}$ on the airspeed V, the total damping and total stiffness matrices, $\bar{\mathbf{C}}$ and $\bar{\mathbf{K}}^{\mathbf{nl}}$, respectively, are also functions of V, as highlighted. In contrast, the total mass matrix $\bar{\mathbf{M}}$ is constant. Furthermore, because of the combined nonlinearity in stiffness terms, $\bar{\mathbf{K}}^{\mathbf{nl}}$ also depends on the dofs $h(t)$ and $\theta(t)$, which change at each instant of time t.

Equation 3.26 refers to the configuration without viscoelastic damping. In the next chapter, where the numerical integration process will be detailed, it will be modified to include the viscoelastic feature on the pitch and plunge dofs.

3.2 State space representation

Once the equation of motion was established, Eq. 3.26, it is possible to determine the critical flutter speed of the system by writing its state matrix $\mathbf{A}$ and obtaining its eigenvalues, as these are closely related to the stability of the system. For the linear configuration ($a_0^h = a_0^\theta = 1$, $a_1^h = a_1^\theta = 0$) the state matrix depends only on the airspeed V, $\mathbf{A}(V)$:

$$\dot{\mathbf{x}} = \mathbf{A}(V)\mathbf{x} \tag{3.27}$$

where $\mathbf{x} = \begin{Bmatrix} h & \theta & \dot{h} & \dot{\theta} & \lambda_1 & \lambda_2 & v \end{Bmatrix}^{\mathsf{T}}$.

In this context, an asymptotically stable condition is identified when all eigenvalues have negative real parts, while an unstable behavior develops if any one of these parts becomes positive (ABDELKEFI et al., 2013). The onset of flutter is associated with the transitional condition of neutral stability in which the eigenvalues have a real part equal to zero (ABDELKEFI et al., 2013).

The eigenvalues, denoted by Λ_j, are in the form (WRIGHT; Cooper, 2014):

$$\bar{\Lambda}_j = -\zeta_j\omega_j \pm i\omega_j\sqrt{1-{\zeta_j}^2} \tag{3.28}$$

where i is the imaginary unit and j stands for the jth eigenvalue. As the natural frequency w_j is always positive, for the real part of the eigenvalue $\left(\bar{\Lambda}_j^{\mathrm{Re}}\right)$ to be zero, the damping factor ζ_j must also be zero. Hence, this condition also identifies the onset of flutter. Thus, examining the behavior of the damping factor with the flow speed for each mode, the critical speed may be found for the linear configuration. With this objective, the damping factor can be expressed from Eq. 3.28 as:

$$\zeta_j = \frac{-\bar{\Lambda}_j^{\mathrm{Re}}}{\sqrt{\left(\bar{\Lambda}_j^{\mathrm{Re}}\right)^2 + \left(\bar{\Lambda}_j^{\mathrm{Im}}\right)^2}} \tag{3.29}$$

From Eq. 3.28, the damped natural frequency ω_j^d is the imaginary part of the eigenvalue:

$$\omega_j^d = \bar{\Lambda}_j^{\mathrm{Im}} \tag{3.30}$$

Before ζ_j can be computed from the eigenvalues, one must write $\mathbf{A}$ according to Eq. 3.27. The first step is to solve Eq. 3.21 for $\ddot{h}$ and $\ddot{\theta}$ (SILVA et al., 2018), yielding:

$$\begin{Bmatrix} \ddot{h} \\ \ddot{\theta} \end{Bmatrix} = \tilde{\mathbf{M}}^{-1} a_4 \begin{Bmatrix} \lambda_1 \\ \lambda_2 \end{Bmatrix} - \tilde{\mathbf{M}}^{-1}\tilde{\mathbf{C}} \begin{Bmatrix} \dot{h} \\ \dot{\theta} \end{Bmatrix} - \tilde{\mathbf{M}}^{-1}\tilde{\mathbf{K}} \begin{Bmatrix} h \\ \theta \end{Bmatrix} + \tilde{\mathbf{M}}^{-1}\mathbf{H}^{\mathsf{T}} v \tag{3.31}$$

which is substituted in Eq. 2.30 to obtain $\begin{Bmatrix} \dot{\lambda_1} & \dot{\lambda_2} \end{Bmatrix}^{\mathsf{T}}$ as function of first order therms only. The outcome is the following expression:

$$\begin{aligned} \begin{Bmatrix} \dot{\lambda}_1 \\ \dot{\lambda}_2 \end{Bmatrix} &= \left(\mathbf{b_4} + \mathbf{b_1}\tilde{\mathbf{M}}^{-1} a_4\right) \begin{Bmatrix} \lambda_1 \\ \lambda_2 \end{Bmatrix} + \left(\mathbf{b_2} - \mathbf{b_1}\tilde{\mathbf{M}}^{-1}\tilde{\mathbf{C}}\right) \begin{Bmatrix} \dot{h} \\ \dot{\theta} \end{Bmatrix} + \\ &\left(\mathbf{b}_3 - \mathbf{b_1}\tilde{\mathbf{M}}^{-1}\tilde{\mathbf{K}}\right) \begin{Bmatrix} h \\ \theta \end{Bmatrix} + \mathbf{b_1}\tilde{\mathbf{M}}^{-1}\mathbf{H}^{\mathsf{T}} v \end{aligned} \tag{3.32}$$

The next step is solve Eq. 3.19 for the voltage derivative $\dot{v}$:

$$\dot{v} = -\frac{1}{C_{eq}} \left(\alpha \dot{h} + \frac{v}{R} \right) \tag{3.33}$$

Finally, similarly to SOUSA et al. (2011), the state matrix can be written from Eq. 3.31, Eq. 3.32, and Eq. 3.33 as shown in Appendix B.

For the nonlinear configuration, both with and without viscoelastic damping, the most direct way of computing the flutter speed is by numerically integrating the equation of motion for an increasing flow speed. The speed at which the system start displaying an LCO is the critical speed.

CHAPTER IV

VISCOELASTIC MODEL

As discussed in the Introduction, the main contribution of this thesis is the proposal of viscoelastic damping combined with structural nonlinearities to improve FEH. Part of the enhancement is expected to be a direct consequence of controlling the amplitude of LCO and preventing stalling, which can both extend the airspeed range suitable for harvesting. In this regard, the dissipative properties of the viscoelastic material are crucial.

According to MARTINS (2014), one might consider the viscoelastic behavior as the resulting combination of a linear elastic solid with a Newtonian fluid, the first described by Hooke's law, $\sigma = E\varepsilon$, and the second by $\tau = \mu\dot{\varepsilon}$, where σ and τ denote, respectively, tensile and shear stresses, E is the Young's modulus of elasticity, ε is the strain and μ is the viscosity. Thus, when a load is applied to viscoelastic materials, they deform and exhibit elastic and viscous components simultaneously (AVILA, 2010). As a result, an elastic time-dependent deformation is observed (STOPPA, 2003). Even for a constant stress $\bar{\sigma}$, the strain varies with time in a nonlinear fashion (Fig. 4.1a), according to what is known as the fluency function, $\varepsilon(\bar{\sigma}, t)$. Similarly, the change in stress given a constant strain $\bar{\varepsilon}$ is predicted by the relaxation function $\sigma(\bar{\varepsilon}, t)$ (Fig. 4.1b).

A challenge in modeling this behavior comes from the damping associated with the relaxation and recovery process of the molecular structure of the material, which introduces a frequency and temperature dependence (STOPPA, 2003). To cope with this situation, several methods were proposed, ranging from classic rheological models to more advanced approaches based on fractional derivatives.

After discussing the classic and generalized viscoelastic models, this chapter explains how the viscoelastic damping feature is efficiently modeled by means of a recurrent fractional derivative approach. Moreover, it describes how the viscoelastic effect is added to the system and details the time integration scheme of the associated equation of motion.

4.1 Classic analytical models

Rheological models, also known as classic analytical models, are the simplest uni-dimensional methods in which the material is represented by associations of springs and

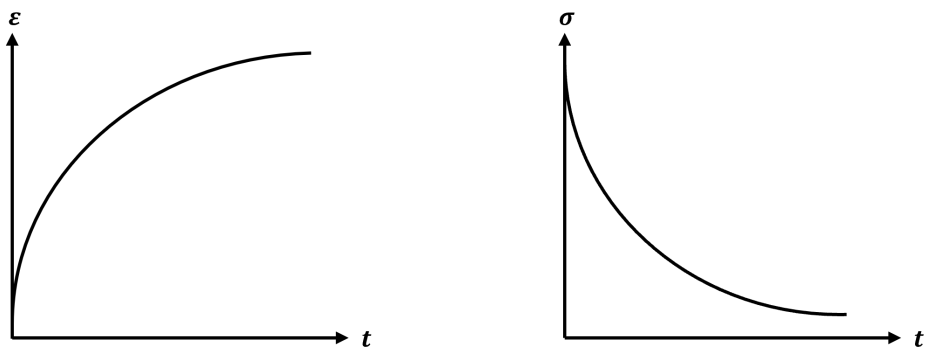

(a) (b)

Figure 4.1 – Viscoelastic fluency (a) and relaxation (b) functions.

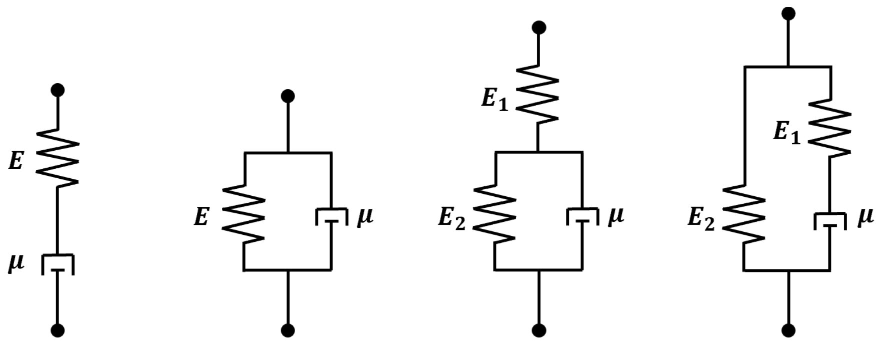

(a) (b) (c) (d)

Figure 4.2 – Maxwell (a), Kelvin-Voigt (b) and Zener (c, d) viscoelastic models.

dashpots (CINIELLO, 2016), described respectively by Hooke's and Newton's laws. Some examples are the models of Maxwell, Kelvin-Voigt and Zener, also known as standard linear solid, displayed in Fig. 4.2, whose constitutive relations are given, respectively, by Eq. 4.1, Eq. 4.2 and Eq. 4.3:

$$\sigma + \frac{\mu}{E}\frac{d\sigma}{dt} = \mu\frac{d\varepsilon}{dt} \tag{4.1}$$

$$\sigma = E\varepsilon + \mu\frac{d\varepsilon}{dt} \tag{4.2}$$

$$\sigma + b_1^E\frac{d\sigma}{dt} = a_0^E\varepsilon + a_1^E\frac{d\varepsilon}{dt} \tag{4.3}$$

where the coefficients b_1^E, a_0^E, and a_1^E are:

$$b_1^E = \frac{\mu}{E_1+E_2}, \qquad a_0^E = \frac{E_1E_2}{E_1+E_2}, \qquad a_1^E = \frac{\mu E_2}{E_1+E_2}, \tag{4.4}$$

and Eq. 4.3 corresponds to the Zener model of Fig. 4.2c.

Although these classic rheological models are valuable for understanding the theoretical fundamentals of viscoelasticity and from a historical perspective (CINIELLO, 2016), by comparing

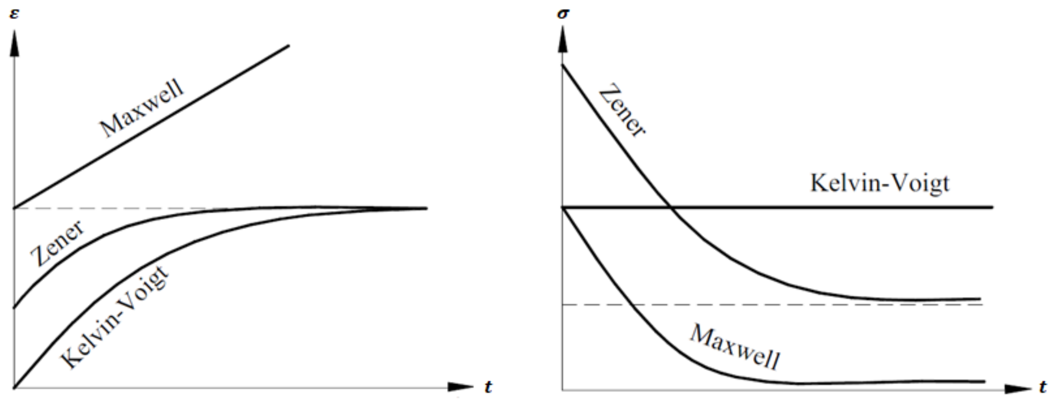

(a) (b)

Figure 4.3 – Comparison of fluency (a) and relaxation (b) functions for classic rheological models (adapted from (WANG, 2001)).

Fig. 4.3 with Fig. 4.1, it is clear that only the Zener model can satisfactorily simulate fluency and relaxation (CHRISTENSEN, 1982).

If a harmonic solution is assumed for the fluency and relaxation functions such that $\sigma(t) = \bar{\sigma}e^{i\omega t}$ and $\varepsilon(t) = \bar{\varepsilon}e^{i\omega t}$, Eq. 4.3 for the Zener model becomes a function of the angular frequency ω:

$$\bar{\sigma} = \left[\frac{a_0^E + a_1^E(i\omega)}{1 + b_1^E(i\omega)}\right]\bar{\varepsilon} \tag{4.5}$$

where the term in brackets is the complex modulus of elasticity $E^*(\omega)$. It can be rewritten as a function of the storage and loss moduli, respectively, $E^{'}(\omega)$ and $E^{''}(\omega)$:

$$E^*(\omega) = \left[\frac{a_0^E + a_1^E(i\omega)}{1 + b_1^E(i\omega)}\right] = E^{'}(\omega) + iE^{''}(\omega) \tag{4.6}$$

where:

$$E^{'}(\omega) = \frac{a_0^E + a_1^E b_1^E \omega^2}{1 + \left(b_1^E\omega\right)^2} \tag{4.7}$$

and

$$E^{''}(\omega) = \frac{\omega\left(a_1^E - b_1^E a_0^E\right)}{1 + \left(b_1^E\omega\right)^2} \tag{4.8}$$

The former represents how much energy is stored elastically and the latter stands for the amount of energy lost as heat.

It is also possible to describe $E^*(\omega)$ by the ratio between the stored and dissipated energies, $\eta(\omega) = E^{''}(\omega)/E^{'}(\omega)$, known as the loss factor. Hence, the complex modulus becomes $E^*(\omega) = E^{'}(\omega)\left[1 + i\eta(\omega)\right]$. Viscoelastic materials are a natural choice for vibration control precisely because they usually possess a high loss factor (RAO, 2010), being able to efficiently dissipate energy.

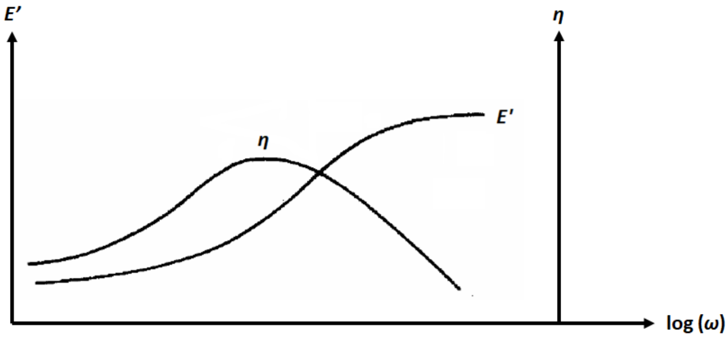

Figure 4.4 – Storage and loss factor as function of oscillation frequency (adapted from NASHIF, JONES and HENDERSON (1985)).

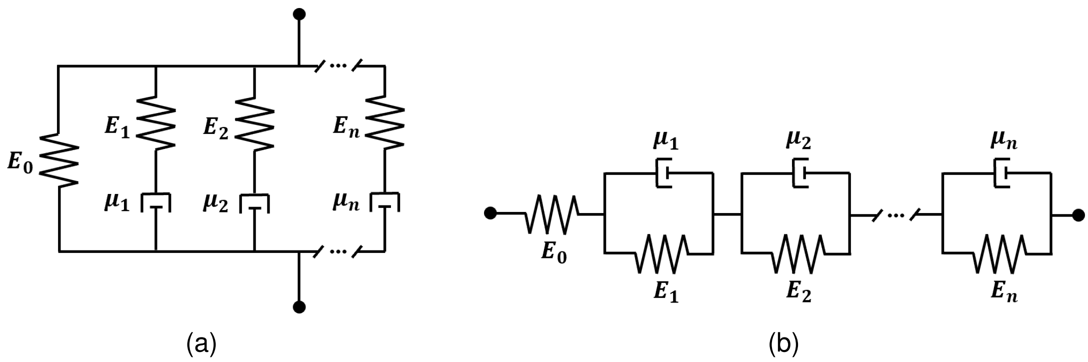

Figure 4.5 – Generalized Maxwell (a) and generalized Kelvin (b) viscoelastic models.

Equations 4.6 to 4.8 are explicit functions of ω. Figure 4.4 displays the variation of $E^{'}$ and η with frequency. As classic rheological models struggle to represent this frequency dependence (SHU; YOU; ZHOU, 2022), a key aspect in viscoelasticity, a more representative approach was needed, motivating the development of generalized viscoelastic models.

4.2 Generalized models

To improve accuracy, the number of springs and dashpots elements was increased to originate the generalized Maxwell (Fig. 4.5a) and generalized Kelvin (Fig. 4.5b) models. These methods were found to predict creep, stress relaxation, and frequency dependency with an accuracy equivalent to more elaborate fractional derivative methods (SHU; YOU; ZHOU, 2022).

Any arbitrary configuration of springs and dashpots such as the generalized Maxwell and Kelvin-Voigt models can be described by the following general constitutive relation:

$$\sigma + \sum_{j=1}^{J} b_j^E \frac{d^j \sigma}{dt^j} = a_0^E \varepsilon + \sum_{n=1}^{N} a_n^E \frac{d^n \varepsilon}{dt^n} \tag{4.9}$$

where j and n are integers that determine the order of each derivative in their respective sums.

Unfortunately, the number of parameters required to reach an acceptable representation through a wide frequency range is usually high in generalized models (STOPPA, 2003), which hinders its application to systems with a large number of dof, particularly to FEM models (LIMA, 2007).

4.3 Fractional derivative representation

The representation of viscoelastic behavior can be enhanced by using fractional order derivatives (PRITZ, 2003). Among the available options, the fractional Zener model is capable of accurately predicting frequency-dependent viscoelastic properties in an efficient way (PRITZ, 2003). The constitutive relation proposed by this model is found by replacing the integer time derivatives in Eq. 4.3 by their fractional correspondents as follows:

$$\sigma + b_1^E \frac{d\sigma^{\psi}}{dt^{\psi}} = a_0^E \varepsilon + a_1^E \frac{d^{\iota}\varepsilon}{dt^{\iota}} \tag{4.10}$$

where ψ and ι are the orders of the fractional derivatives, limited between 0 and 1. It varies with temperature, assuming values close to 1 at higher temperatures, where the behavior of the viscoelastic material approximates a fluid, and close to 0 at lower temperatures, for which the behavior resembles a solid material.

To satisfy the thermodynamic constraints of nonnegative internal work and nonnegative energy dissipation, BAGLEY and TORVIK (1986) demonstrated that the orders of partial derivatives must be the same, as observed in the experimental data. Therefore, it is possible to assume $\psi = \iota$, reducing the number of required parameters in Eq. 4.10 from five to four (a_0^E, a_1^E, b_1^E and ι), thus simplifying the analysis.

A fractional derivative generalizes the concept of differentiation to non-integer orders, being able to describe intermediate behaviors (AVILA, 2010). It was originally created for purely mathematics, before its use in other fields was proposed. In fact, there is more than one definition of a fractional derivative. The Riemann definition is as follows (CUNHA FILHO, 2019):

$$\frac{d^{\iota} f(t)}{dt^{\iota}} = \frac{1}{\Gamma^* (1-\iota)} \frac{d}{dt} \int_0^t \frac{f(t-\xi)}{\xi^{\iota}} d\xi \tag{4.11}$$

where Γ^* is the gamma function. From Eq. 4.11, it is evident that the integral is dependent on the previous values of f, thus adding a memory effect that is necessary to model viscoelastic materials (AVILA, 2010).

Through the Grünwald-Letnikov approximation, it is possible to represent fractional derivatives numerically (AVILA, 2010), in the form:

$$\frac{d^{\iota} f(t)}{dt^{\iota}} = \Delta t^{-\iota} \sum_{j=0}^{J} g_{j+1}^{v} f(t - j\Delta t) \tag{4.12}$$

where g_{j+1}^{v} are the recurrent terms known as Grünwald's coefficients. These are defined by the following:

$$g_{j+1}^{v} = \frac{j-\iota-1}{j} g_j^{v} \tag{4.13}$$

which are computed $j+1$ times according to the memory size J, given by the product of N_J discrete points and a time step Δt, $J = N_J \Delta t$.

By plotting the Grünwald coefficients for $N_J =$ 20 (Fig. 4.6), it is evident that they have a fading influence on the system, asymptotically tending to zero as time increases. Thus, the

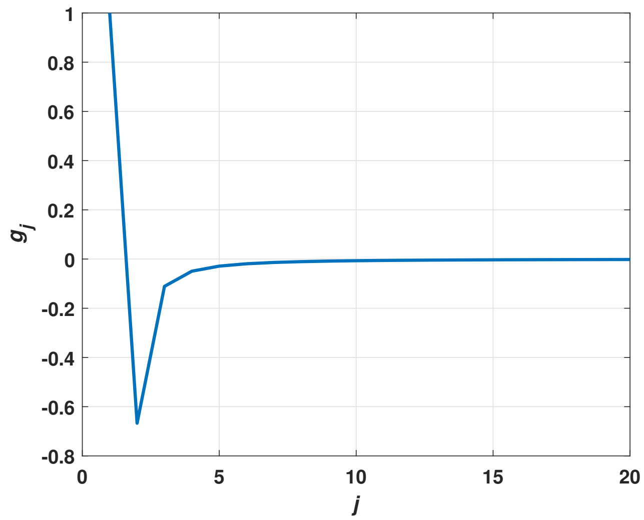

Figure 4.6 – Fading memory effect of the Grünwald's coefficients.

previous states closest to a given instant t dominate the memory effect at this instant, whereas those further in the past have a decaying influence.

Substituting Eq. 4.12 into Eq. 4.10 and solving for σ_t, one obtains the following discrete version of the fractional constitutive relation:

$$\sigma_t = a_0^E(\varepsilon_{t-j\Delta t}) + a_1^E \Delta t^{-\iota} \sum_{j=0}^{J} (g_{j+1}^v)(\varepsilon_{t-j\Delta t}) - b_1^E \Delta t^{-\iota} \sum_{j=0}^{J} (g_{j+1}^v)(\sigma_{t-j\Delta t}) \tag{4.14}$$

where it is evident that σ_t depends on its former states. As noted by CUNHA FILHO (2019), this self-dependency implies the need to compute stress at every instant of time and to store its history, considerably increasing the simulation costs. In the context of this thesis, the analysis is in the time domain, and, to obtain the bifurcation diagrams, one must numerically integrate the equation of motion consecutively for different airspeeds, until steady state is reached at each one. This might be prohibitive, particularly if the optimization of the system is attempted, motivating the use of the recurrent approach described below.

4.3.1 Recurrent approach

To eliminate the inconvenience of stress self-dependency in Eq. 4.14, previous work in LMEst (CUNHA FILHO, 2019; CUNHA FILHO et al., 2021) proposed using a recurrent formulation. Following CUNHA FILHO (2019), the fractional constitutive equation predicted by the recurrent approach at a discrete time instant t is given as follows:

$$\sigma_t = \sum_{j=0}^{J} \kappa_{j+1}^E(\varepsilon_{t-j\Delta t}) \tag{4.15}$$

where κ_{j+1}^E is the recurrent term. Clearly, σ_t is no longer self-dependent, being a function of the known strain history $\varepsilon_{t-j\Delta t}$, calculated in previous iterations. For a uni dimensional stress state,

κ_{j+1}^E becomes the following function of the Grünwald coefficients g:

$$\kappa_{j+1}^E = D_3^E(g_{j+1}^v) + \sum_{i=0}^{j} D_1^E(g_{i+1})(\kappa_{j+1-i}^E) \tag{4.16}$$

where D_1^E and D_3^E are, respectively:

$$D_1^E = -\frac{b_1^E \Delta t^{-\iota}}{1 + b_1^E \Delta t^{-\iota}} \tag{4.17}$$

and

$$D_3^E = \frac{a_1^E \Delta t^{-\iota}}{1 + b_1^E \Delta t^{-\iota}} \tag{4.18}$$

The first term $\kappa_1 = D_2^E$ is:

$$\kappa_1^E = D_2^E = \frac{a_0^E + a_1^E \Delta t^{-\iota}}{1 + b_1^E \Delta t^{-\iota}} \tag{4.19}$$

Equation 4.10 is for an element in tensile stress. In fact, as explained in Section 4.4, the proposed VEDs work in shear. For this case, the shear stress at a given time instant, τ_t, is described as follows:

$$\tau_t = \sum_{j=0}^{J} \kappa_{j+1}^G(\gamma_{t-j\Delta t}) \tag{4.20}$$

where the shear strain story is $\gamma_{t-j\Delta t}$. Moreover, the associated recurrent term κ_{j+1}^G is in the same form as in Eq. 4.21:

$$\kappa_{j+1}^G = D_3^G(g_{j+1}^v) + \sum_{i=0}^{j} D_1^G(g_{i+1})(\kappa_{j+1-i}^G) \tag{4.21}$$

where D_1^G and D_3^G are, respectively:

$$D_1^G = -\frac{b_1^G \Delta t^{-\iota}}{1 + b_1^G \Delta t^{-\iota}} \tag{4.22}$$

and

$$D_3^G = \frac{2a_1^G \Delta t^{-\iota}}{1 + b_1^G \Delta t^{-\iota}} \tag{4.23}$$

The first term $\kappa_1^G = D_2^G$ is:

$$\kappa_1^G = D_2^G = \frac{2a_0^G + 2a_1^G \Delta t^{-\iota}}{1 + b_1^G \Delta t^{-\iota}} \tag{4.24}$$

As the recurrent term is a constant function of the material properties and the time step used, it can be conveniently computed before the numerical integration procedure, reducing computational costs. A detailed derivation of the recurrent term for the uni and tridimensional constitutive laws can be found in CUNHA FILHO (2019).

4.4 Viscoelastic stiffness and damping

Figure 4.7 shows the incorporation of viscoelastic dampers (VED) in the pitch and plunge dofs of the proposed FEH device. The idea is that the added damping and stiffness of each dof can be tuned to enhance the performance of the system and passively control vibration. The stiffness of the VEDs in pitch and plunge is indicated by k_θ^v and k_h^v, respectively, while the damping is in the form of the dissipative forces $F_{t-\Delta t}^\theta$ and $F_{t-\Delta t}^h$. Here, the subscript $t-\Delta t$ highlights the dependency of the system displacement story.

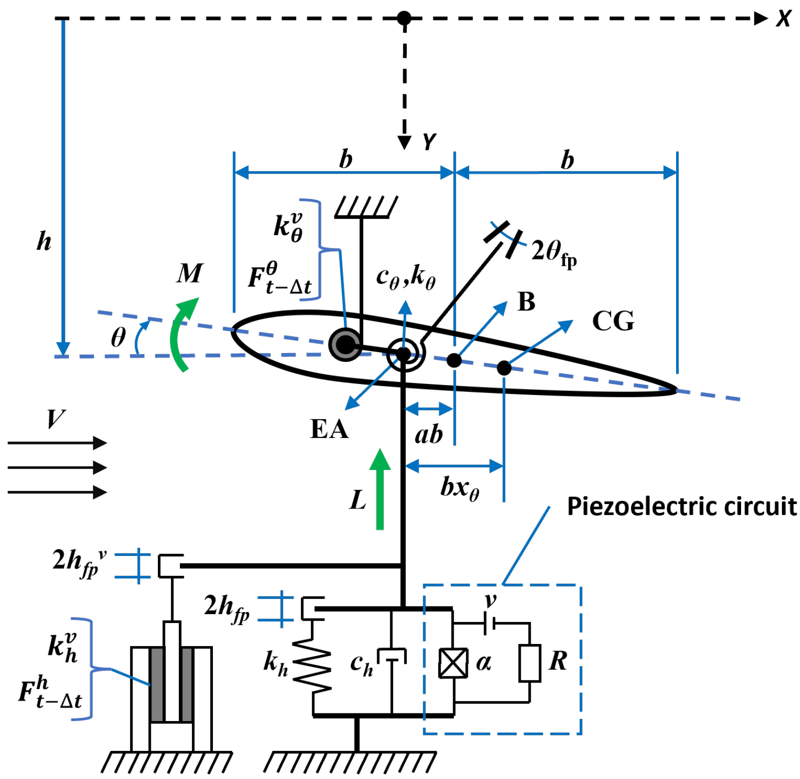

Figure 4.7 – Nonlinear airfoil with piezoelectric circuit and viscoelastic dampers in pitch and plunge.

One may notice that the system must exceed a given vibration amplitude in plunge to start interacting with the VED in this dof. The gap that defines the associated threshold is h_{fp}^v. Hence, there is a free-play nonlinearity in the viscoelastic damper in h, which is discontinuously represented by:

$$k_{h,fp}^v = \begin{cases} \frac{2k_h^v}{h} & h > h_{fp}^v \\ 0 & -h_{fp}^v \leq h \leq h_{fp}^v \\ \frac{2k_h^v}{h} & h < -h_{fp}^v \end{cases} \tag{4.25}$$

where the factor of 2 comes from the two viscoelastic layers that integrate the VED in plunge (Fig. 4.7). In contrast, the VED in θ is directly connected to this dof, without any free-play, and in parallel with the corresponding nonlinear spring.

The VEDs are presented in detail in Fig. 4.8 and Fig. 4.9. The plunge damper is a prismatic element of dimensions l_x X l_y X l_z (Fig. 4.8a), constrained between a fixed support and a moving component, experiencing direct shear (Fig. 4.8b). In turn, the pitch damper is a circular tubular shaft of length l_θ, internal radius R_i and external radius R_e (Fig. 4.9b), which develops shear from the torsion caused by θ (Fig. 4.9a).

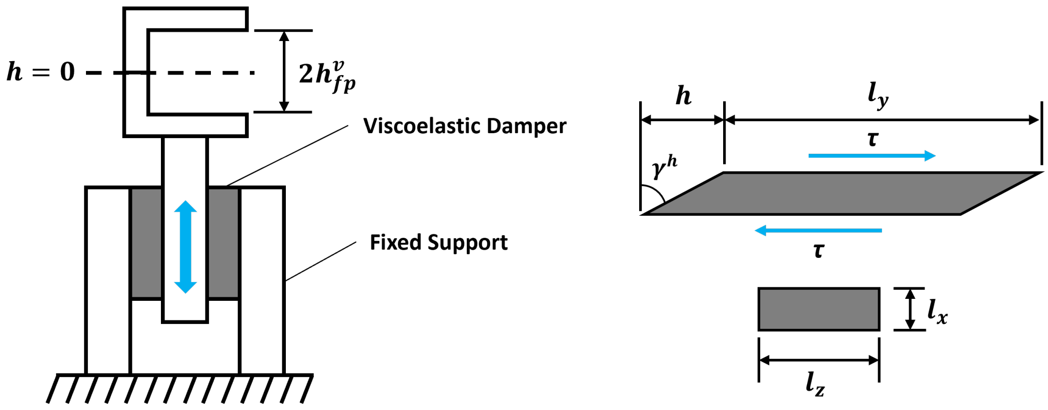

Figure 4.8 – VED in plunge (a) and corresponding viscoelastic element in shear (b) .

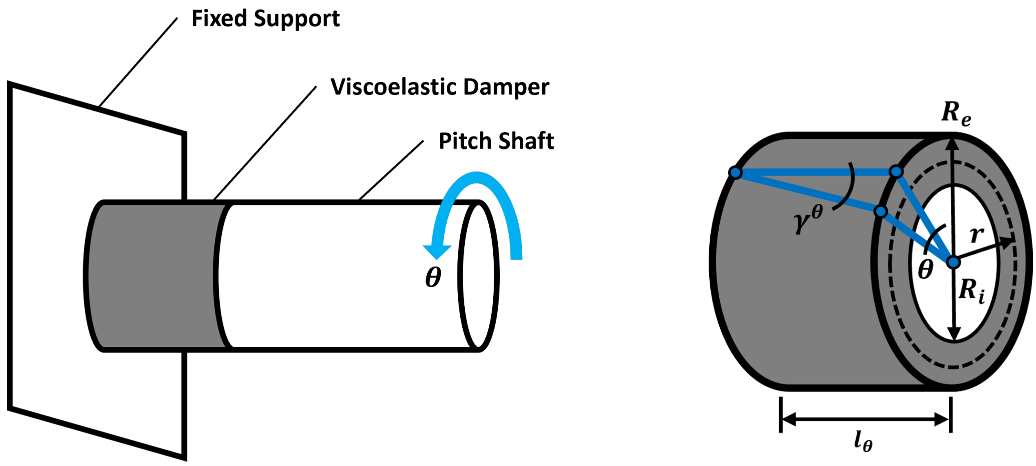

Figure 4.9 – VED in pitch (a) and corresponding viscoelastic element in shear (b).

The viscoelastic properties can be conveniently and efficiently determined from the recurrent fractional derivative description of the shear-strain relationship, Eq. 4.20. With this goal, it is necessary to write the deformation energy U_d of the VED as:

$$U_d = \frac{1}{2}\int_{\upsilon} \gamma_t \tau_t d\upsilon \tag{4.26}$$

where υ denotes the volume of the element. Equation 4.26 must be applied to the pitch and plunge VEDs separately, as their geometries differ.

For VED in plunge, assuming small γ_t^h, such that $\tan(\gamma_t^h) \approx \gamma_t^h$, the deformation is $\gamma_t^h = h_t/l_x$. The rectangular volume element is $d\upsilon^h = dxdydz$. Substituting these terms into Eq. 4.26, along with τ_t from Eq. 4.20, one obtains the associated deformation energy, U_d^h:

$$U_d^h = \frac{1}{2}\int_{\upsilon_h} \gamma_t^h \tau_t d\upsilon^h = \frac{1}{2}\int_0^{l_z}\int_0^{l_y}\int_0^{l_x} \left(\frac{h_t}{l_x}\right) \sum_{j=0}^{J} \kappa_{j+1} \left(\frac{h_{t-j\Delta t}}{l_x}\right) dxdydz \tag{4.27}$$

which, noting that $h_t = h_t(t)$ is independent of x, y and z, results in:

$$U_d^h = \frac{1}{2}\left[p_h \sum_{j=0}^{J} \kappa_{j+1} h_{(t-j\Delta t)}\right] h_t \tag{4.28}$$

where $p_h = (l_z l_y)/l_x$ is a geometric factor that denotes the shear area per unit thickness of the VED. Next, by evaluating the first term in the sum, $j = 0$, the deformation energy becomes:

$$U_d^h = \frac{1}{2}\left(p_h \kappa_1\right) h_t^2 + \frac{1}{2}\left[p_h \sum_{j=1}^{J} \kappa_{j+1} h_{(t-j\Delta t)}\right] h_t = \frac{1}{2} k_h^v h_t^2 + \frac{1}{2} F_{t-\Delta t}^h h_t \tag{4.29}$$

being a direct function of the stiffness and dissipative forces of the VED in the plunge dof, k_v^h and $F_{t-\Delta t}^h$, respectively.

The VED in the pitch dof experiences pure torsion. Thus, the associated deformation is $\gamma_t^\theta = (r/l_\theta)\theta_t$. For a ring-shaped volume element, $dv^\theta = 2\pi r dr dz$, the deformation energy U_d^θ is:

$$U_d^\theta = \frac{1}{2}\int_{v_\theta} \gamma_t^\theta \tau_t dv^\theta = \frac{1}{2}\int_0^{l_\theta}\int_{R_i}^{R_e} \left(\frac{r}{l_\theta}\right)^2 \theta_t \sum_{j=0}^{J} \kappa_{j+1}\theta_{(t-j\Delta t)} \left(2\pi r dr dz\right) \tag{4.30}$$

which, after solving the integral, becomes:

$$U_d^\theta = \frac{1}{2}\left[p_\theta \sum_{j=0}^{J} \kappa_{j+1}\theta_{(t-j\Delta t)}\right]\theta_t \tag{4.31}$$

where $p_\theta = \pi\left({R_e}^4 - {R_i}^4\right)/(2l_\theta)$ is the geometric factor of the pitch VED. Evaluating the first term of the sum $j = 0$ in Eq. 4.31, results in the stiffness and dissipative force associated with the VED in pitch:

$$U_d^\theta = \frac{1}{2}\left(p_\theta \kappa_1\right)\theta_t^2 + \frac{1}{2}\left[p_\theta \sum_{j=1}^{J} \kappa_{j+1}\theta_{(t-j\Delta t)}\right]\theta_t = \frac{1}{2} k_\theta^v \theta_t^2 + \frac{1}{2} F_{t-\Delta t}^\theta \theta_t \tag{4.32}$$

respectively, k_v^θ and $F_{t-\Delta t}^\theta$.

Given that the VEDs are in parallel with the nonlinear springs, they are incorporated into the equation of motion by directly summing the viscoelastic stiffness terms to their corresponding dofs in Eq. 3.24:

$$\tilde{\mathbf{K}}_{\mathbf{v}}^{\mathbf{nl}} = \tilde{\mathbf{K}}^{\mathbf{nl}} + \begin{bmatrix} k_{h,fp}^v & 0 \\ 0 & {k_\theta}^v \end{bmatrix} \tag{4.33}$$

such that Eq. 4.34 replaces $\tilde{\mathbf{K}}^{\mathbf{nl}}$ in Eq. 3.25, and $\bar{\mathbf{K}}^{\mathbf{nl}}$ becomes:

$$\bar{\mathbf{K}}_{\mathbf{v}}^{\mathbf{nl}} = \begin{bmatrix} \tilde{\mathbf{K}}_{\mathbf{v}}^{\mathbf{nl}} & -\boldsymbol{a_4} & -\mathbf{H}^\mathsf{T} \\ -\mathbf{b_3} & -\mathbf{b_4} & \mathbf{0} \\ \mathbf{0} & \mathbf{0} & R^{-1} \end{bmatrix} \tag{4.34}$$

Moreover, the dissipative efforts must also be included in the equation of motion, yielding the following:

$$\bar{\mathbf{M}}\ddot{\mathbf{q}} + \bar{\mathbf{C}}\left(V\right)\dot{\mathbf{q}} + \bar{\mathbf{K}}_{\mathbf{v}}^{\mathbf{nl}}\left(V, t, T\right)\mathbf{q} = \mathbf{F}_{\mathbf{v}}(t, T) \tag{4.35}$$

where the dissipative force vector is given by:

$$\mathbf{F_v}(t,T) = \left\{ -F^h_{t-\Delta t} \quad -F^\theta_{t-\Delta t} \quad 0 \quad 0 \quad 0 \right\}^\mathsf{T} \tag{4.36}$$

which depends on temperature and on the previous displacement due to the memory effect caused by the VEDs. In addition, the stiffness matrix $\bar{\mathbf{K}}^{\mathbf{nl}}_{\mathbf{v}}(V,t,T)$ also becomes a function of temperature as result of the viscoelastic terms. These aspects further increase the complexity of the analysis. In fact, given that the equation of motion, Eq. 4.35, involves nonlinear piecewise terms and memory effects due to the proposed VEDs, the most practical way to obtain a solution is by numerical integration. The use of the recurrent fractional derivative approach to describe the viscoelastic constitutive equation is well suited for such a procedure in the discrete time domain.

4.5 Time integration scheme

A combination of the Newmark and Newton-Raphson methods is used for the time integration procedure. The Newmark method assumes a linear variation in acceleration between two consecutive time instants separated by Δt (RAO, 2010), describing the acceleration and velocity vectors, respectively, as

$$\ddot{\mathbf{q}}_{t+\Delta t} = \left(\frac{1}{\nu \Delta t^2}\right)(\mathbf{q}_{t+\Delta t} - \mathbf{q}_t) - \left(\frac{1}{\nu \Delta t}\right)\dot{\mathbf{q}}_t - \left(\frac{1}{2\nu} - 1\right)\ddot{\mathbf{q}}_t \tag{4.37}$$

and

$$\dot{\mathbf{q}}_{t+\Delta t} = \left(\frac{\delta}{\nu \Delta t^2}\right)(\mathbf{q}_{t+\Delta t} - \mathbf{q}_t) - \left(\frac{\delta}{\nu} - 1\right)\dot{\mathbf{q}}_t - \left[\frac{\Delta t}{2}\left(\frac{\delta}{\nu} - 2\right)\right]\ddot{\mathbf{q}}_t \tag{4.38}$$

where the Newmark parameters are chosen as $\nu = 1/4$ and $\delta = 1/2$ to make the method unconditionally stable (RAO, 2010).

By substituting Eq. 4.37 and Eq. 4.38 in the equation of motion, Eq. 4.35, one obtains:

$$(\mathbf{\Xi_1})\,\mathbf{q}_{t+\Delta t} - (\mathbf{\Xi_1})\,\mathbf{q}_t - (\mathbf{\Xi_2})\,\dot{\mathbf{q}}_t - (\mathbf{\Xi_3})\,\ddot{\mathbf{q}}_t + \left[\left(\bar{\mathbf{K}}^{\mathbf{nl}}_{\mathbf{v}}\right)_{t+\Delta t}\right]\mathbf{q}_{t+\Delta t} = \mathbf{F_v} \tag{4.39}$$

where:

$$\mathbf{\Xi_1} = \left(\frac{1}{\nu \Delta t^2}\right)\bar{\mathbf{M}} + \left(\frac{\delta}{\nu \Delta t}\right)\bar{\mathbf{C}} \tag{4.40}$$

$$\mathbf{\Xi_2} = \left(\frac{1}{\nu \Delta t}\right)\bar{\mathbf{M}} + \left(\frac{\delta}{\nu} - 1\right)\bar{\mathbf{C}} \tag{4.41}$$

$$\mathbf{\Xi_3} = \left(\frac{1}{2\nu} - 1\right)\bar{\mathbf{M}} + \frac{\Delta t}{2}\left(\frac{\delta}{\nu} - 2\right)\bar{\mathbf{C}} \tag{4.42}$$

Rewriting Eq. 4.39 to express $\mathbf{q}_{t+\Delta t}$ as a function of its preceding state at time t, $\mathbf{q}_t$, results in the following:

$$\left[\left(\bar{\mathbf{K}}^{\mathbf{nl}}_{\mathbf{v}}\right)_{t+\Delta t} + \mathbf{\Xi_1}\right]\mathbf{q}_{t+\Delta t} = \mathbf{F_v} + (\mathbf{\Xi_1})\,\mathbf{q}_t + (\mathbf{\Xi_2})\,\dot{\mathbf{q}}_t + (\mathbf{\Xi_3})\,\ddot{\mathbf{q}}_t \tag{4.43}$$

which cannot be solved directly for $\mathbf{q}_{t+\Delta t}$ as the stiffness matrix is a function of the sought displacement due to its nonlinear nature, $\left(\bar{\mathbf{K}}_{\mathbf{v}}^{\mathbf{nl}}\right)_{t+\Delta t} = \bar{\mathbf{K}}_{\mathbf{v}}^{\mathbf{nl}}\left(\mathbf{q}_{t+\Delta t}\right)$. This can be overcome by converting the discrete form of the equation of movement, Eq. 4.43, in a root-finding problem whose solution is determined using the Newton-Raphson method. Hence, it is necessary to define a residue to be nullified, namely $\mathbf{R}_{t+\Delta t}^{n-1}$, as follows:

$$\mathbf{R}_{t+\Delta t}^{n-1} = \left[\left(\bar{\mathbf{K}}_{\mathbf{v}}^{\mathbf{nl}}\right)_{t+\Delta t} + \mathbf{\Xi_1}\right]\mathbf{q}_{t+\Delta t}^{n-1} - \left[\mathbf{F_v} + \left(\mathbf{\Xi_1}\right)\mathbf{q}_t + \left(\mathbf{\Xi_2}\right)\dot{\mathbf{q}}_t + \left(\mathbf{\Xi_3}\right)\ddot{\mathbf{q}}_t\right] \tag{4.44}$$

where n denotes a given iteration in the Newton-Raphson loop.

According to the Newton-Raphson method, the associated displacement $\mathbf{q}_{t+\Delta t}^{n}$ is computed from:

$$\mathbf{q}_{t+\Delta t}^{n} = \mathbf{q}_{t+\Delta t}^{n-1} + \Delta\mathbf{q}_{t+\Delta t}^{n-1} \tag{4.45}$$

where the increment $\Delta\mathbf{q}_{t+\Delta t}^{s}$ is:

$$\Delta\mathbf{q}_{t+\Delta t}^{n-1} = -\left[\frac{d\left(\mathbf{R}_{t+\Delta t}^{n-1}\right)}{d\left(\mathbf{q}_{t+\Delta t}^{n-1}\right)}\right]^{-1}\mathbf{R}_{t+\Delta t}^{n-1} \tag{4.46}$$

and the residue derivative $d\left(\mathbf{R}_{t+\Delta t}^{n-1}\right)/d\left(\mathbf{q}_{t+\Delta t}^{n-1}\right)$ for the problem considered is given as:

$$\frac{d\left(\mathbf{R}_{t+\Delta t}^{n-1}\right)}{d\left(\mathbf{q}_{t+\Delta t}^{n-1}\right)} = \left(\bar{\mathbf{K}}_{\mathbf{v}}^{\mathbf{nl}}\right)_{t+\Delta t} + \mathbf{\Xi_1} + \left(\mathbf{d}_{t+\Delta t}^{n-1}\right)\left(\mathbf{q}_{t+\Delta t}^{n-1}\right) \tag{4.47}$$

where the diagonal matrix $\mathbf{d}_{(t+\Delta t)}^{n-1}$ is:

$$\mathbf{d}_{t+\Delta t}^{n-1} = \begin{bmatrix} \left(dk_h^{nl}/dh\right)_{t+\Delta t}^{n-1} & 0 & \cdots & 0 \\ 0 & \left(dk_\theta^{nl}/d\theta\right)_{t+\Delta t}^{n-1} & \cdots & 0 \\ \vdots & \vdots & \ddots & \vdots \\ 0 & 0 & \cdots & 0 \end{bmatrix} \tag{4.48}$$

The convergence criterion for the displacement vector is the ratio between the norm of its current increment $\Delta\mathbf{q}_{t+\Delta t}^{s}$ and the norm of its current value $\mathbf{q}_{t+\Delta t}^{s}$, given as:

$$\frac{\left\|\Delta\mathbf{q}_{t+\Delta t}^{s}\right\|}{\left\|\mathbf{q}_{t+\Delta t}^{s}\right\|} \leq tol \tag{4.49}$$

where tol denotes an assumed tolerance.

Once convergence for displacement at a given instant t has been obtained by the Newton-Raphson method, $\mathbf{q}_{t+\Delta t}^{s}$ yields the corresponding acceleration and velocity vectors at that instant as predicted by the Newmark approach, respectively from Eq. 4.37 and Eq. 4.38. This process is repeated for every time instant considered to yield the time response and phase diagrams. Alternatively, Eq. 4.38 can be rewritten in the following more compact form:

$$\dot{\mathbf{q}}_{t+\Delta t} = \dot{\mathbf{q}}_t + \Delta t\left(1-\delta\right)\ddot{\mathbf{q}}_t + \left(\delta\Delta t\right)\ddot{\mathbf{q}}_{t+\Delta t} \tag{4.50}$$

Given the dependence of the stiffness and damping matrices on airspeed mentioned previously, it is necessary to add an additional iteration loop in which this parameter changes to compute the bifurcation diagrams. In this way, the steady-state amplitude of the time response at a given airspeed is consecutively extracted to create the bifurcation diagram. This is valid for a given combination of input parameters. Therefore, if any other parameter changes, such as temperature, a new corresponding bifurcation diagram must be generated.

The flow chart of Fig. 4.10 details the described numeric methodology to obtain the time response, and the corresponding bifurcation diagram. As can be seen, the recurrent FDM approach removes the self-dependency of stress from the combined Newmark and Newton-Raphson time integration procedure, detailed in Fig. 4.11.

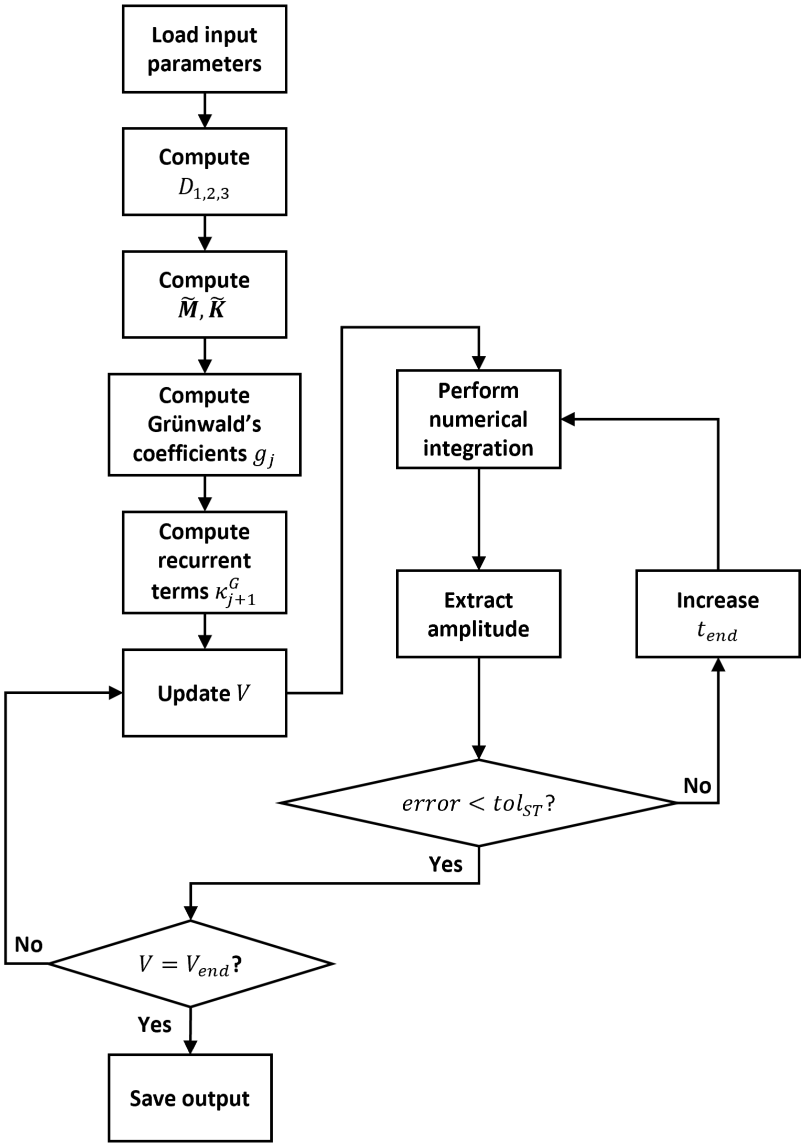

Figure 4.10 – Numeric procedure used to obtain the time response and bifurcation diagrams of the proposed FEH device.

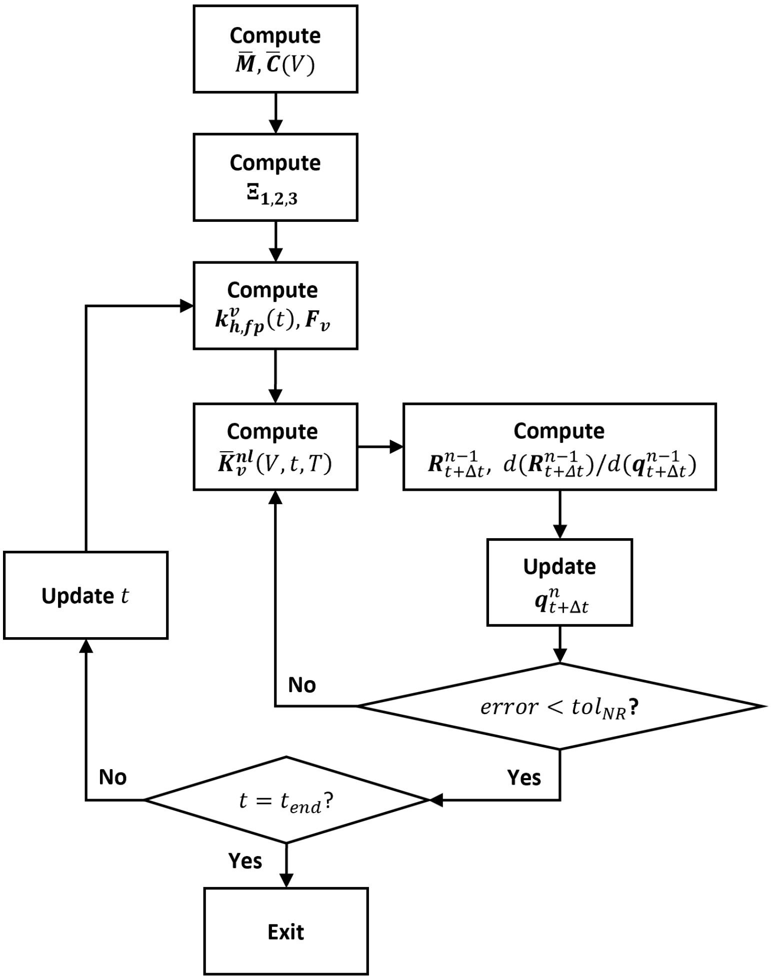

Figure 4.11 – Numerical integration procedure.

4.6 Viscoelastic properties

The present thesis uses 3M-ISD112™ as the material for the proposed VEDs. It is a commercially available acrylic polymer manufactured by 3M™, designed specifically for vibration damping. The choice was motivated by its previous use as a flutter suppression technique in the research efforts of the LMEst (MARTINS, 2014; BORGES, 2019; CUNHA FILHO, 2019; CARVALHO, 2024).

The FDM parameters were determined by CUNHA FILHO (2019) and CUNHA FILHO et al. (2021) from experimental measurements, as an inverse problem. The values are summarized in Tab 4.1 for different temperatures. Intermediate values are obtained from a cubic interpolation of the table values as illustrated by Fig. 4.12. All parameters show a strong nonlinear variation with temperature.

Table 4.1 – FDM parameters at different temperatures (CUNHA FILHO et al., 2021).

T [°C]	a_0^G [kPa]	a_1^G [kPa s]	b_1^G [s]	ι [−]
10	412.887	147.864	8.217×10^{-4}	0.66714
15	403.531	95.061	4.680×10^{-4}	0.66091
20	419.582	57.563	3.162×10^{-4}	0.66780
25	427.808	35.483	2.541×10^{-4}	0.67643
27	423.716	31.293	1.723×10^{-4}	0.67107
29	422.615	27.288	1.097×10^{-4}	0.66801
30	425.301	24.489	1.388×10^{-4}	0.67273
35	429.484	16.272	1.302×10^{-4}	0.67902

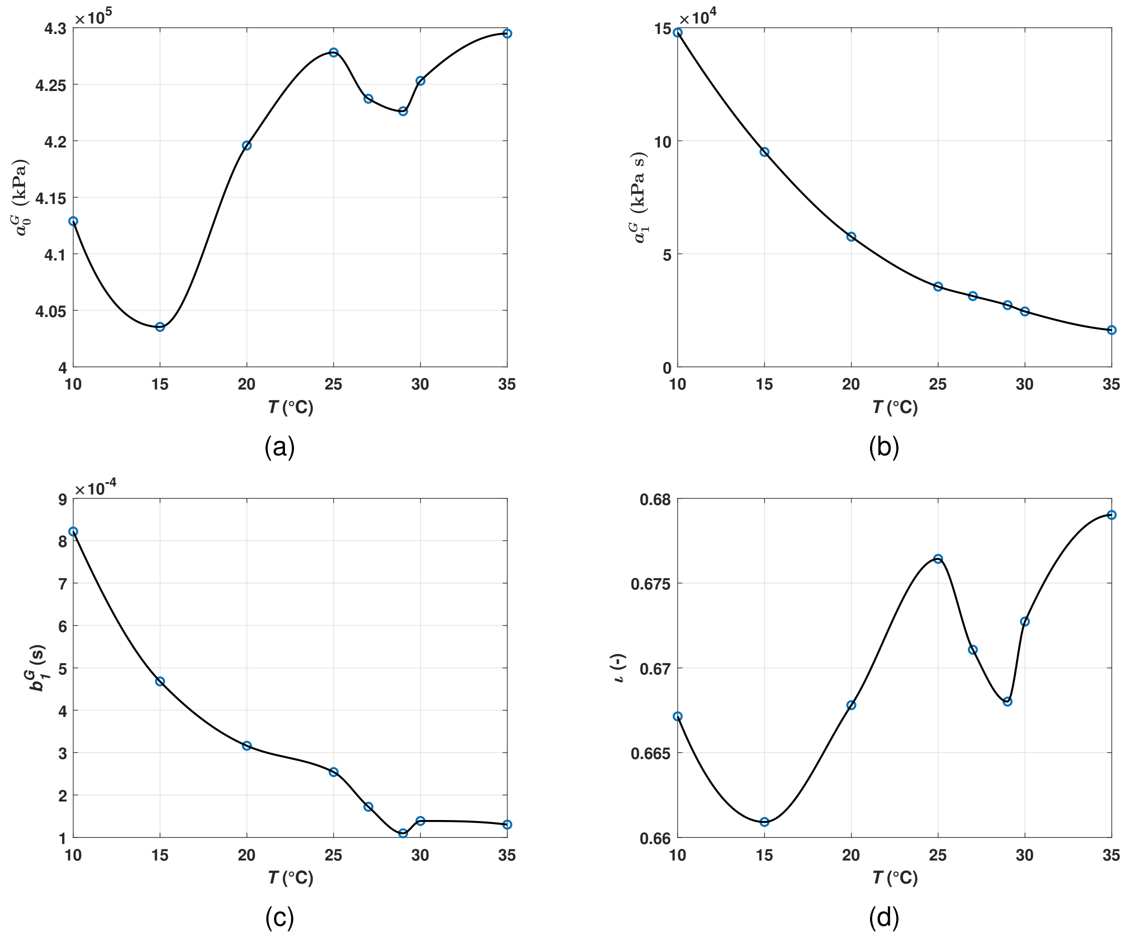

Figure 4.12 – Interpolation of the FDM parameters a_0^G (a), a_1^G (b), b_1^G (c) and ι (d).

CHAPTER V

OPTIMAL-ROBUST DESIGN

A natural goal in engineering is to design a system so that its performance is optimal. In the context of this thesis, it is desirable that the FEH device is able to output the highest power possible for a wide airspeed interval and that the harvesting starts at the lowest CWS. However, given the physical complexity, a parametric analysis, although valuable to gain a general insight of the system's behavior, might not suffice to ensure the best attainable performance.

As one of the main characteristics of VED is its temperature dependency, it is fundamental that the optimal configuration is robust in relation to changes in temperature. In addition, uncertainty in the design parameters will always be present and can also negatively impact its performance. Hence, they should also be included in the optimization scheme from a robust perspective. This chapter briefly discusses the concept of multi-objective optimization for the deterministic and robust cases.

This chapter briefly discusses the concept of multi-objective optimization for the deterministic and robust cases and how to tackle the proposed optimization problem in an efficient way through metamodeling. Given the time domain analysis following a direct time integration procedure of the nonlinear equation of motion with memory effects, as described in the previous chapter, this is necessary to make the optimization feasible, especially for the robust case.

5.1 The optimization problem

An optimization problem consists of finding the combination of design variables, represented by the vector $\mathbf{x}$, that maximizes or minimizes a given function $y = f(\mathbf{x})$. Usually, a general way to define the optimization problem is by the following notation (VANDERPLAATS, 1999):

$$\begin{aligned} &\min y = f(\mathbf{x}) \\ &\text{subjected to} \begin{cases} \mathbf{x^L} \leq \mathbf{x} \leq \mathbf{x^U} \\ \mathbf{g}(\mathbf{x}) \leq 0 \\ \mathbf{g_{eq}}(\mathbf{x}) = 0 \end{cases} \end{aligned} \tag{5.1}$$

where it is assumed as a minimization problem by default. The terms in the curly brackets are the constraints imposed on the design variables. The first term represents the side constraints, indicating the lower and upper boundaries of the design variables, specified by the vectors $\mathbf{x^L}$ and $\mathbf{x^U}$, respectively. These define the domain in which the optimal solution is to be found. In this sense, $\mathbf{x} \subset \mathbb{R}^d$, where d is the total number of design variables. Moreover, $\mathbf{g}(\mathbf{x})$ and $\mathbf{g_{eq}}(\mathbf{x})$ are, respectively, the inequality and equality constraints that the design variables must satisfy.

Side constraints arise from physical limitations imposed by aspects such as fabrication and transportation, for example, while $\mathbf{g}(\mathbf{x})$ and $\mathbf{g_{eq}}(\mathbf{x})$ come from requirements regarding the performance of the system (RAO, 2009). Following an example from VANDERPLAATS (1999), one might attempt to design an internal combustion engine whose efficiency is maximum for a specified power output while limiting the amount of pollutants emitted. In this case, power and the amount of pollution could be considered as inequality constraints. As the engine must fit a given internal space, some of its dimensions would represent side constraints.

A two-dimensional generic design space is presented in Fig. 5.1 together with the values of the design variables that critically satisfy the inequality constrains, that is, when $g_j(\mathbf{x}) = 0$. These critical values will form hypersurfaces of dimension $n - 1$ whose combination will divide the design space between feasible and infeasible points (RAO, 2009). A point located on a hypersurface is named a bound point.

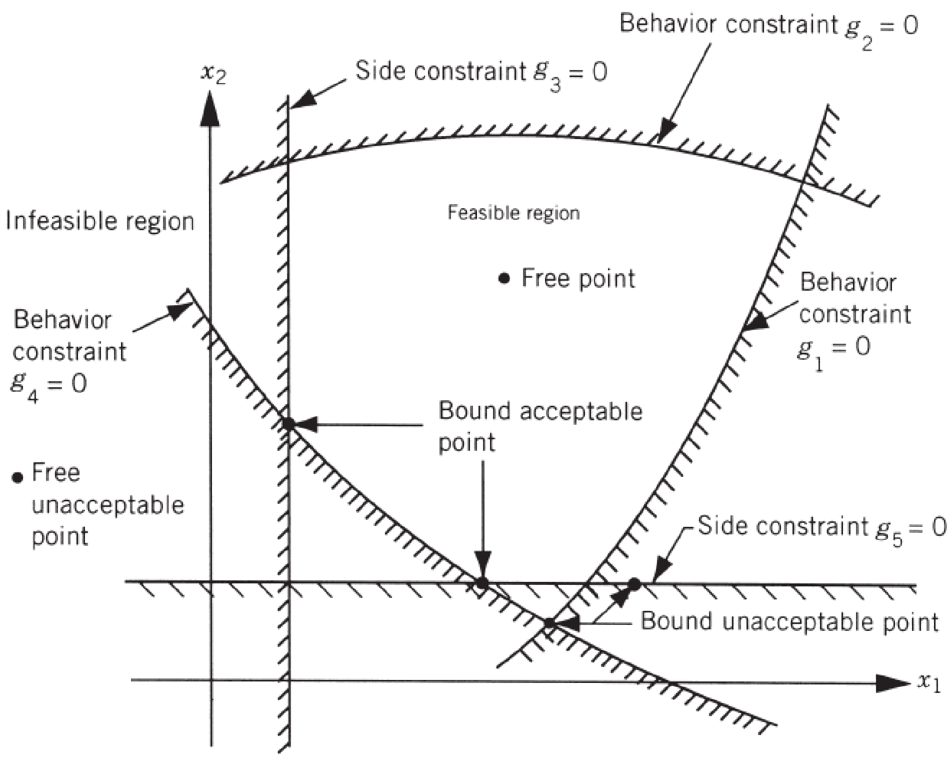

Figure 5.1 – Example of a bi-dimensional design space in the presence of constraint surfaces (RAO, 2009).

Although Eq. 5.1 was defined for minimization, the correspondent maximization problem is written simply by multiplying the objective function by minus one and reversing the inequality sign of the inequality constraints (VANDERPLAATS, 1999). This process is clearly illustrated in Fig. 5.2.

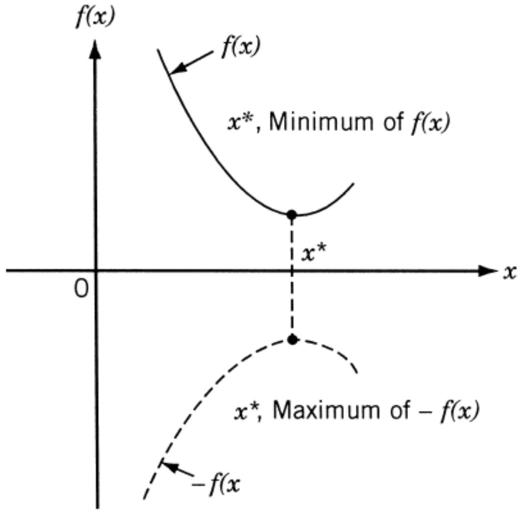

Figure 5.2 – Converting a maximization optimization problem into a minimization problem (RAO, 2009).

5.2 Multi-objective optimization

In practice, most optimization problems in engineering are multi-objective, such that $y = f(\mathbf{x})$ in Eq. 5.1 becomes a vector, $\mathbf{y} = \mathbf{f}(\mathbf{x}) = [f_1(\mathbf{x}), \cdots, f_n(\mathbf{x})]$, where n is the total number of objectives. In this sense, aspects such as cost, performance, reliability, effectiveness, efficiency, safety, and simplicity, among others, usually compete with each other in the design phase, as adjusting the design variables to improve one objective will be often detrimental to the other. Therefore, there is rarely a single solution for a multi-objective optimization problem (MOP) (LOBATO, 2008). Instead, many solutions can be proposed. Hence, it is necessary to establish a comparison criterion between solutions, as a direct approach is not possible, since the distinct objectives are equally important (DINIZ, 2024). This can be made with the concept of Pareto dominance, according to which a particular configuration of design variables $\mathbf{x_a}$ dominates another $\mathbf{x_b}$ ($\mathbf{x_a} \succ \mathbf{x_b}$) if there is no objective in $\mathbf{y_b}$ that surpasses its correspondent in $\mathbf{y_a}$ and at least one objective in $\mathbf{y_a}$ has a better value than its correspondent in $\mathbf{y_b}$ (ROSTAMI; NERI; GYAURSK, 2020).

Figure 5.3 illustrates the concept of dominance for an MOP with two objectives to minimize: $f_1(\mathbf{x})$ and $f_2(\mathbf{x})$. If point D is taken as a reference, it clearly dominates E, having lower values for both objectives. The opposite is true in relation to points B and C. However, the points A and F surpass D in one objective and are surpassed by D in the other. Therefore, they are indifferent in relation to D.

As a result of dominance, solving the MOP means finding a set of solutions not dominated by any other, called Pareto-optimal solutions. In this set, it is impossible to find a solution capable of improving one objective without worsening any other (LIMA, 2007). Formally, it is defined as $P^X = \{\mathbf{x} \in \mathbf{X} : \nexists \mathbf{x}^* \in \mathbf{X} : \mathbf{x}^* \succeq \mathbf{x}\}$ (ROSTAMI; NERI; GYAURSK, 2020), where $\mathbf{X} \subset \mathbb{R}^d$ is the design space.

The image of P^X is the Pareto front, $P^Y = \{\mathbf{f}(\mathbf{x}) : \mathbf{x} \in P^X\}$, which means the optimal

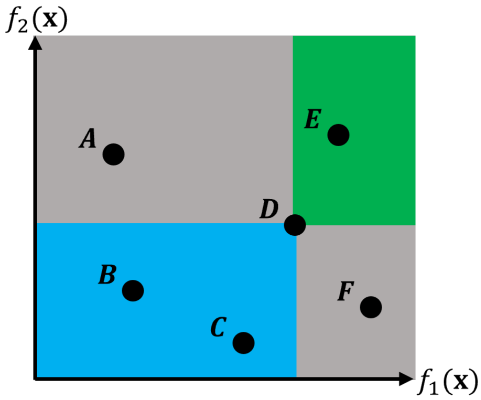

Figure 5.3 – Hypothetical solution points for a two-objective optimization problem.

set of objectives predicted by the non-dominated solutions (DINIZ, 2024). P^Y is located in the objective space $Y \subset \mathbb{R}^n$. Figure 5.4 illustrates the functional relationship between the design and the objective spaces, highlighting the Pareto front.

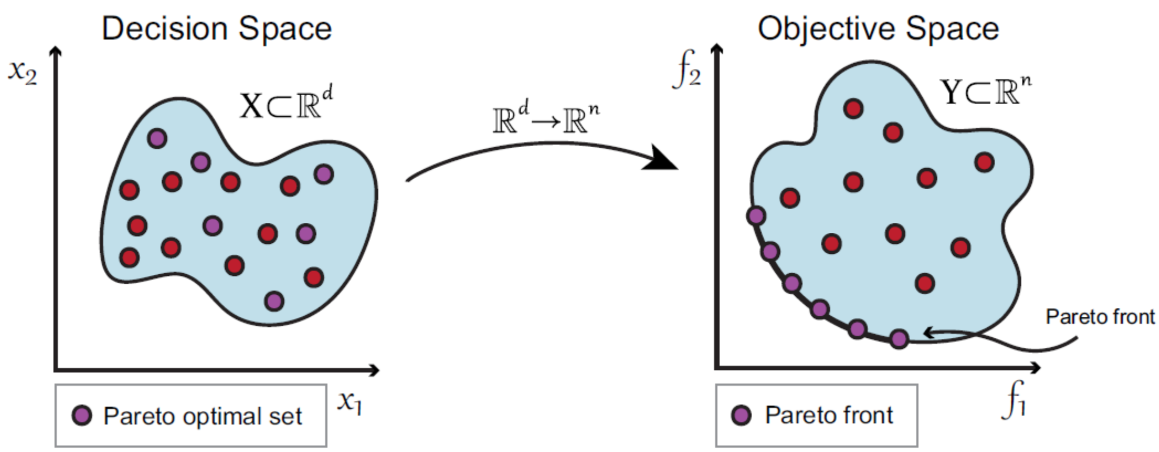

Figure 5.4 – Functional relationship between the design and objective spaces for a MOP with two objectives (ROSTAMI; NERI; GYAURSK, 2020).

Many methods are available to obtain the Pareto front, which can be divided into deterministic and non-deterministic approaches. The former uses concepts from calculus, while the latter does not rely on derivatives, instead proposing a search procedure inspired by concepts of biologic evolution (LOBATO, 2008). Non-deterministic methods include genetic algorithms that incorporate the principle of natural selection in the search procedure (RAO, 2009). For this reason, they are classified as an evolutionary algorithm, which means that each potential solution is considered as an individual belonging to a population that will be iteratively transformed using operations of selection, reproduction, crossover, and mutation, to obtain the best solutions (LOBATO, 2008).

In this thesis, given the complexity of computing the partial derivatives of the nonlinear equation of motion (Eq. 4.35), a non-deterministic approach is preferred, as is often the case. Particularly, the Non-dominated sorting genetic algorithm II (NSGA II) is chosen.

5.2.1 NSGA II

The NSGA II was proposed by DEB et al. (2002) to reduce the computational complexity and hence the simulation time of the NSGA (SRINIVAS; DEB, 1994). The NSGA may be considered a variation of a genetic algorithm in which a non-dominated sorting strategy is used before each generation (Fig. 5.6). This procedure consists of consecutively classifying the available solutions in ranks according to the concept of dominance; the first non-dominated set is assigned to the first rank $(\texttt{rank} = 1)$, and so on (LIMA, 2007), as illustrated in Fig. 5.5. After the ranking is complete, the fitness function of each individual i, $\varpi_i = \texttt{rank}^{-1}$, is calculated and divided by the sharing function to preserve the diversity of solutions (LIMA, 2007).

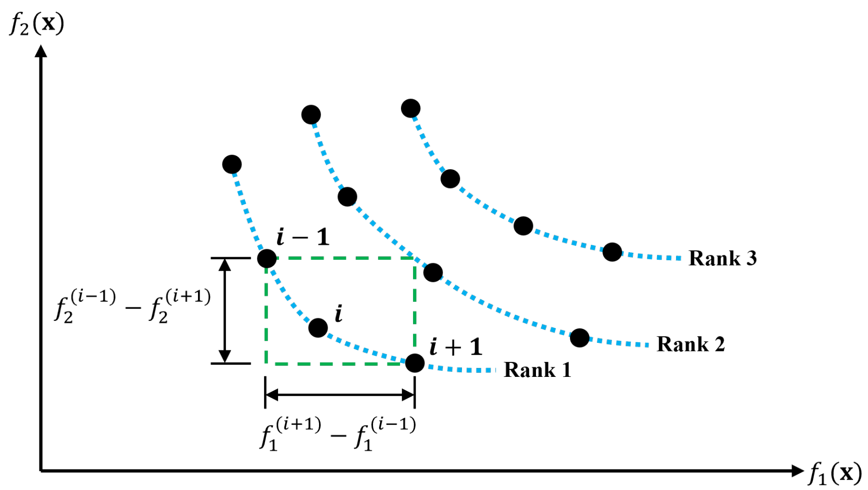

Figure 5.5 – Cuboid used in the crowding distance definition in a ranked population.

The sharing function S_f is given as follows:

$$S_f(d_{ij}) = \begin{cases} 1 - (d_{ij}/N_s) & d_{ij} < N_s \\ 0 & d_{ij} \geq N_s \end{cases} \tag{5.2}$$

where $d_{ij} = \|i - j\|$ is the Euclidean distance between two individuals i and j, and N_s is a constant that determines the size of the niche, that is, the maximum distance within two solutions share each other's fitness (DEB et al., 2002). As N_s is set by the designer, performance will vary depending on this parameter. The NGSA II has two main differences in relation to the NSGA (Fig. 5.7). First, it proposes to maintain the best solutions in the population to prevent the loss of good candidates, known as elitism (LOBATO, 2008). Second, it uses the crowding distance approach in lieu of the sharing function. This eliminates the need to specify N_s, resulting in a more robust method and reduced computational complexity (DEB et al., 2002).

The crowding distance of a solution i, $(CD)^i$, estimates the density of neighboring solutions around i, being defined as the average side length of a cuboid whose vertices are the nearest solutions $i-1$ and $i+1$ at the same rank (Fig. 5.5) (DEB et al., 2002). The $(CD)^i$ can be calculated from

$$(CD)^i = \sum_{\vartheta=1}^{n} \frac{f_\vartheta^{(i+1)} - f_\vartheta^{(i-1)}}{f_\vartheta^{max} - f_\vartheta^{max}} \tag{5.3}$$

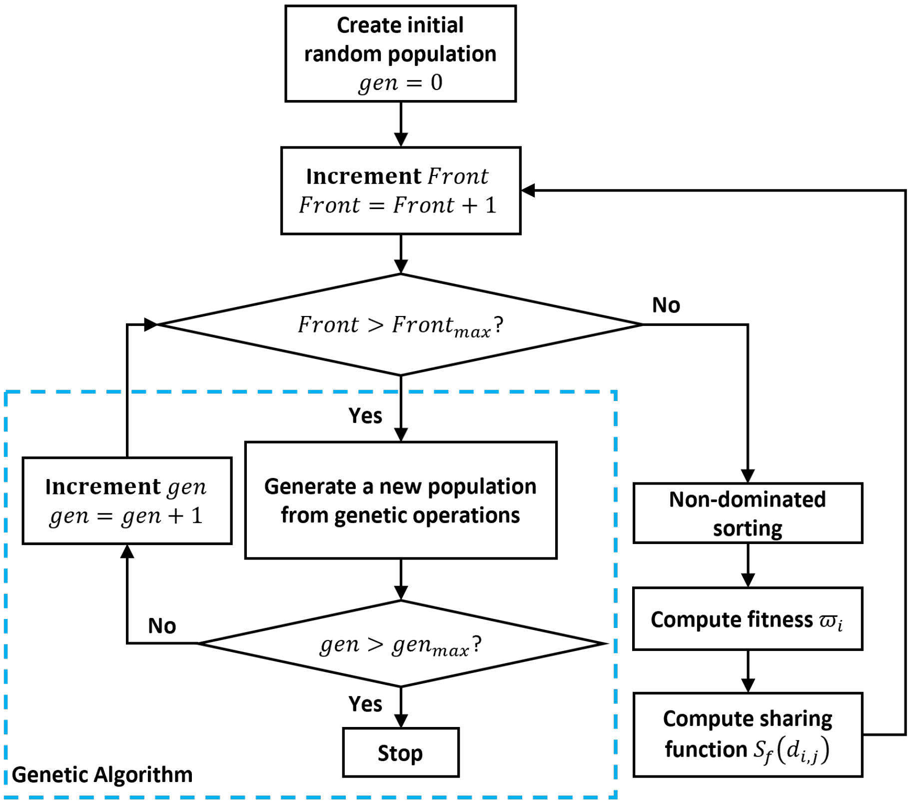

Figure 5.6 – NSGA flowchart.

where ϑ denotes a given objective while f_{ϑ}^{max} and f_{ϑ}^{min} are, respectively, its corresponding maximum and minimum values, used to normalize $(CD)^i$.

5.3 Robust multi-objective optimization

In practical engineering applications, such as aeroelasticity, there are many sources of uncertainty which include manufacturing tolerances, material properties, and non-uniform airflow (DAI; YANG, 2014). These impose deviations in the behavior of the system from the designed configuration which may reduce its intended performance. Hence, it is of interest to take uncertainty into account when solving optimization problems.

Unlike the usual MOP, the robust multi-objective optimization problem (RMOP) attempts to find the optimal solutions taking into account their robustness. This means that not only the value of the objective function itself is relevant, but also how sensitive this value is in relation to perturbations in the associated design variables. A configuration that significantly changes the objectives upon perturbations in its design variables is said to be non-robust. This is not desirable, as the actual system performance might be substantially reduced given the unavoidable presence of uncertainty sources. Variations may also cause a violation of the design constraints such that robustness implies that the optimal point will always be in the feasible region regardless of the perturbations (LEE; PARK, 2001). In the context of this thesis, robustness is a fundamental concept, particularly when considering the strong temperature dependence introduced by the VEDs.

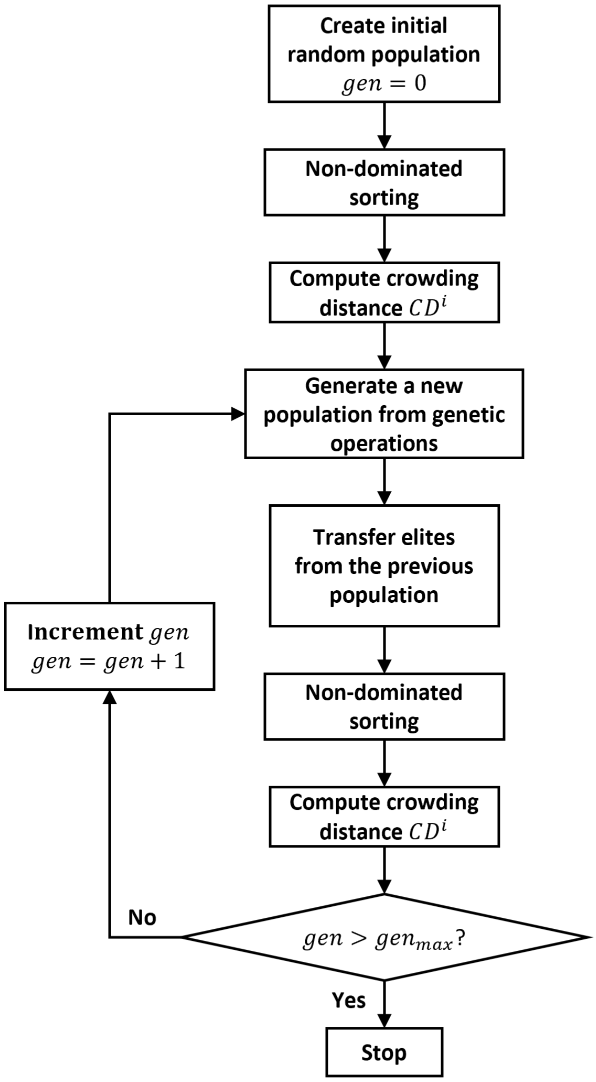

Figure 5.7 – NSGA II flowchart.

The concept of optimal robustness is illustrated by Fig. 5.8 for a single objective problem with a single design variable. Applying the same perturbation Δx for two different points A and B, it is seen that the objective function $f(x)$ is more sensitive to perturbations at the point A than at B $\left(\Delta y^A > \Delta y^B\right)$. Therefore, even though A is a better solution from the perspective of minimization alone, B is a more robust candidate.

A straightforward approach to including robustness in a multi-objective optimization problem is through the concept of the vulnerability function f_n^v. This function represents a means of measuring how much changes in design variables affect a given objective function f_n. Following LIMA (2007), f_n^v is defined as the ratio between the standard deviation σ_n and the mean μ_n of f_n:

$$f_n^v = \frac{\sigma_n}{\mu_n} \tag{5.4}$$

where the reciprocal quantity represents the so-called robustness function, such that $f_n^r = (f_n^v)^{-1}$.

Using the vulnerability function approach to quantify the dispersion of the objective functions, the deterministic multi-objective problem of Eq. 5.1 is converted in its robust counterpart

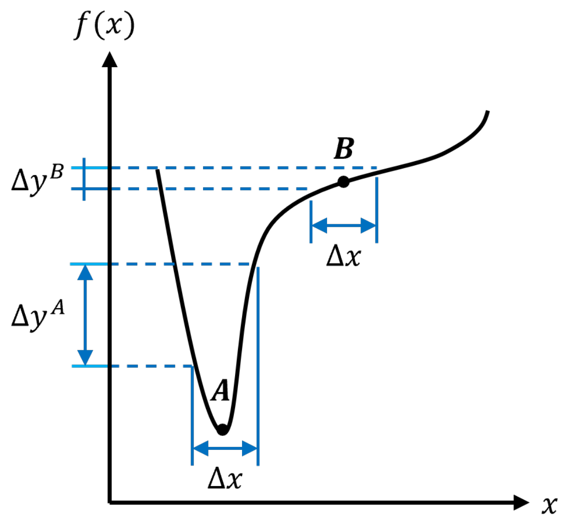

Figure 5.8 – Comparison of two solutions from the optimal robustness perspective.

simply by incorporating the vulnerability functions associated with each objective. As a result, the number of objective functions will double. Therefore, the robust version of the multi-objective optimization problem becomes:

$$\begin{aligned} &\min \mathbf{y^R} = \mathbf{f}(\mathbf{x}) \parallel \mathbf{f^v}(\mathbf{x}) \\ &\text{subjected to} \begin{cases} \mathbf{x^L} \leq \mathbf{x} \leq \mathbf{x^U} \\ \mathbf{g}(\mathbf{x}) \leq 0 \\ \mathbf{g_{eq}}(\mathbf{x}) = 0 \end{cases} \end{aligned} \tag{5.5}$$

where $\mathbf{y^R}$ is a vector that contains all objectives and the vulnerability functions. The dimension of $\mathbf{y^R}$ determines the dimension of the objective space $\mathbb{R}^n$, such that $\mathbf{y^R} \subset \mathbb{R}^n$.

5.3.1 Meta-modeling

Regardless of the chosen optimization method, it will always be necessary to evaluate the objective function consecutively. Depending on the complexity of the model associated with the objective function, this could be a costly procedure which may not be feasible. Unfortunately, as it was discussed in the Chapter IV, this is the case for the approach proposed in this work, as it is necessary to perform direct time integration for each airspeed until a steady state is reached at each one to build a bifurcation diagram.

An option to deal with this situation is the use of meta-modeling so that an expensive high-fidelity model is replaced by another inexpensive one, created from the first. A convenient way to obtain a metamodel is by machine learning techniques, which include the neural network (NN) approach. The goal of the NN is to learn the correlation between a particular combination of input parameters and the associated output, thus replacing the model with an efficient algebraic operation involving the combination weights and biases. In this work, the NN was built and trained with Matlab's Neural Network Toolbox.

The NN architecture is inspired by biological nervous systems, assuming the form of the multilayer perceptron (MLP) shown in Fig. 5.9. This versatile architecture consists of three main parts, namely, an input layer, a given number of hidden layers, and an output layer. Each layer is composed of a given number of neurons. These perform a weighted sum of its input plus a bias and then apply an activation function to produce an output, which is passed to the connected neurons (DINIZ, 2024). It is possible to adjust the weights and inputs consecutively, in an optimization fashion, so that they can relate the input parameters and the expected output of the model to be replaced.

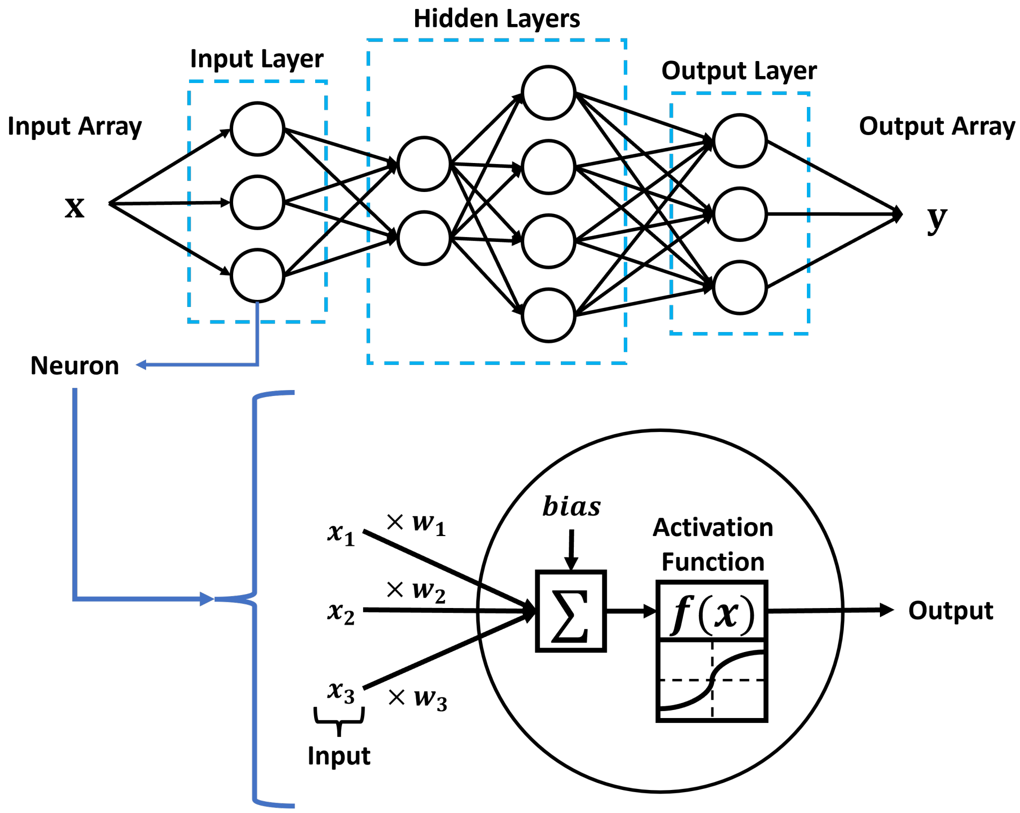

Figure 5.9 – Generic multi-layer perceptron neural network.

CHAPTER VI

NUMERICAL RESULTS

This chapter presents the results of the research thesis. After a brief description of the system, a parametric analysis is performed to identify favorable conditions for energy harvesting. Using its linear behavior as a reference, these conditions are identified by observing time responses, bifurcation, and phase diagrams corresponding to different configurations of the proposed FEH system. Finally, the multi-objective optimization results are discussed for the deterministic and robust cases.

6.1 Piezoaeroelastic system

The airfoil section to be used in the proposed numerical study is a NACA 0012 profile. It integrates an experimental device named PAPA (pitch and plunge apparatus) that belongs to the Aeronautics Institute of Technology (ITA) in São José dos Campos, São Paulo. This device was studied by (SILVA, 2016; SILVA et al., 2018) at ITA, and by (CUNHA FILHO, 2019) in his LMEst research thesis. It consists of an airfoil supported by a mobile frame which is, in turn, connected by springs to a fixed structure, in green (Fig. 6.1). It is worth mentioning that the wing flap DOF is held constant so that there are only the pitch and plunge movements.

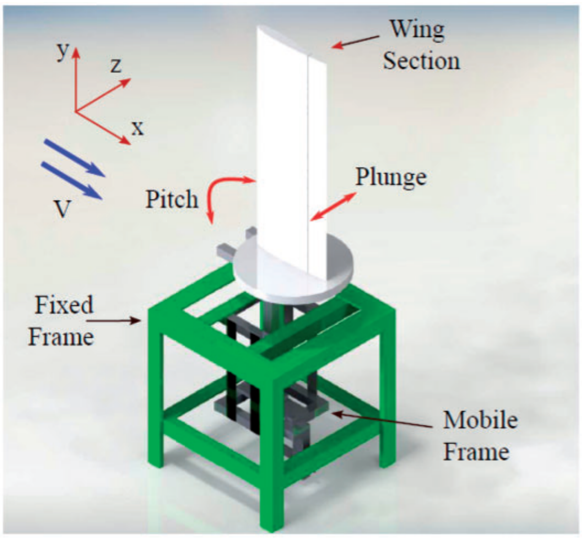

Figure 6.1 – PAPA (SILVA et al., 2018).

A detailed description of the PAPA is available in the above sources. In the context of the present thesis, the specifications in Table 6.1 are sufficient. Moreover, as there is no energy harvesting circuit in the PAPA, the piezoelectric properties used are extracted from the literature dealing with similar FEH systems (ERTURK et al., 2010; BOUMA et al., 2022), also included in Table 6.1.

Table 6.1 – Parameters of the proposed FEH system.

Parameter	Value	Parameter	Value
b	0.145 m	c_h	1.2113 Ns/m
l	0.8 m	c_θ	0.0043 Ns
a	-0.1379	ω_h	14.954 rad/s
x_θ	0.1897	ω_θ	26.955 rad/s
r_θ	0.064 m	α	1.55 mN/V
ρ_∞	1.119 kg/m^3	C_{eq}	120 nF
m_t	13.5 kg	m	6.5 kg

6.1.1 Linear reference behavior

The behavior of the linear configuration of the piezoaeroelastic system will be used as a reference in the proposed analysis. The state-space representation of the system without the harvesting circuit is predicted by Eq. B.12. Solving the associated eigenvalue problem of Eq. 3.28 for a range of airspeeds, one obtains the marginally stable flutter condition when ζ_j of a given mode j becomes zero. This condition is readily identified by plotting ζ_j versus V for the pitch and plunge modes, or the so-called v-g diagram (Fig. 6.2).

Clearly, the critical speed is $V^* =$ 14.01 m/s, which is related to the unstable plunge mode. This value is in agreement with the experimental measurements of CUNHA FILHO (2019) and SILVA (2016). Figure 6.2 also shows the evolution of damped natural frequencies f_j^d with V (v-f diagram), where the coupling between the pitch and plunge modes is evident.

Another way to observe the stability of the system is by directly plotting its time response at a particular airspeed. For an airspeed lower than the flutter speed, such as $V =$ 13.00 m/s, the vibration dies out over time, indicating a stable condition (Fig. 6.3a, Fig. 6.3b). However, at the previously identified critical speed, $V^* =$ 14.01 m/s, the response is harmonic and sustained oscillation is achieved (Fig. 6.3c, Fig. 6.3d). Increasing V to 14.50 m/s will result in unstable behavior, with increasing vibration amplitude over time (Fig. 6.3e, Fig. 6.3f).

It is worth mentioning that, as can be seen in Fig. 6.3, both pitch and plunge DOFs start their movements from an initial condition, respectively, $h =$ 0.1 mm and $\theta =$ 0.01° (Fig. 6.3c, Fig. 6.3d). These initial conditions are necessary to set the system in motion together with a unitary impulse.

Applying the fast Fourier transform (FFT) to the time response, it is possible to obtain

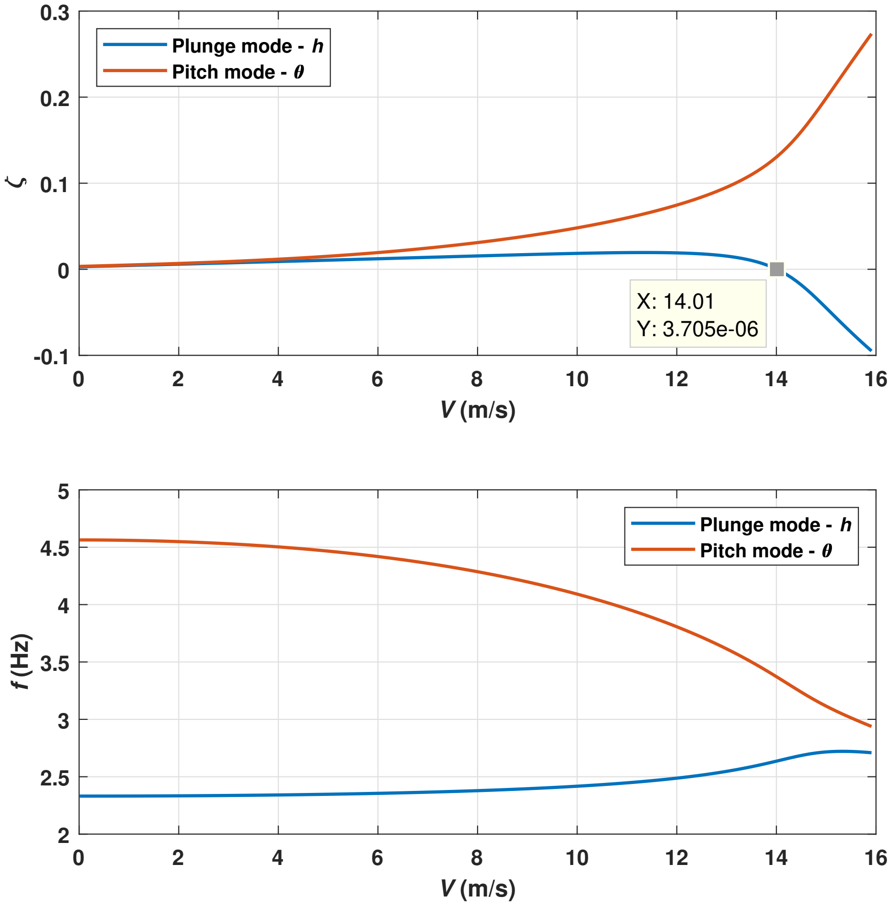

Figure 6.2 – Evolution of the pitch and plunge damping factors ζ_j and damped natural frequencies f_j^d for the linear configuration without the harvesting circuit.

the displacement frequency spectrum. Before flutter, two peaks are observed (Fig. 6.4a) which are close to the natural frequencies of the system at $V = 0$ m/s. As predicted by the v-f diagram of Fig. 6.2, these peaks approach each other as V increases (Fig. 6.4b). At the flutter speed, there is only one peak (Fig. 6.4c), associated with the flutter frequency, which is the frequency of the harmonic response in the flutter condition.

Energy harvesting is achieved by adding the piezoelectric circuit to the aeroelastic system (Fig. 3.1). The piezoelectric material is attached to the plunge DOF so that part of its kinetic energy is converted into electricity by the direct piezoelectric effect. An electric resistance R is connected to the piezoceramic as a means of having an indication of the output power.

Figure 6.5a shows that the voltage increases linearly with R until a saturation region is reached around $R = 1 \times 10^6\ \Omega$. In contrast, there is an optimal value for R in terms of the output power p (Fig. 6.5b), also around $R = 1 \times 10^6\ \Omega$. It is worth mentioning that p is a direct function of R and v, $p = v^2/R$. Furthermore, a direct implication of Fig. 6.5 is that, for the linear configuration, there is a value of R that maximizes both v and p.

From an energy-harvesting perspective, the linear aeroelastic behavior has a major

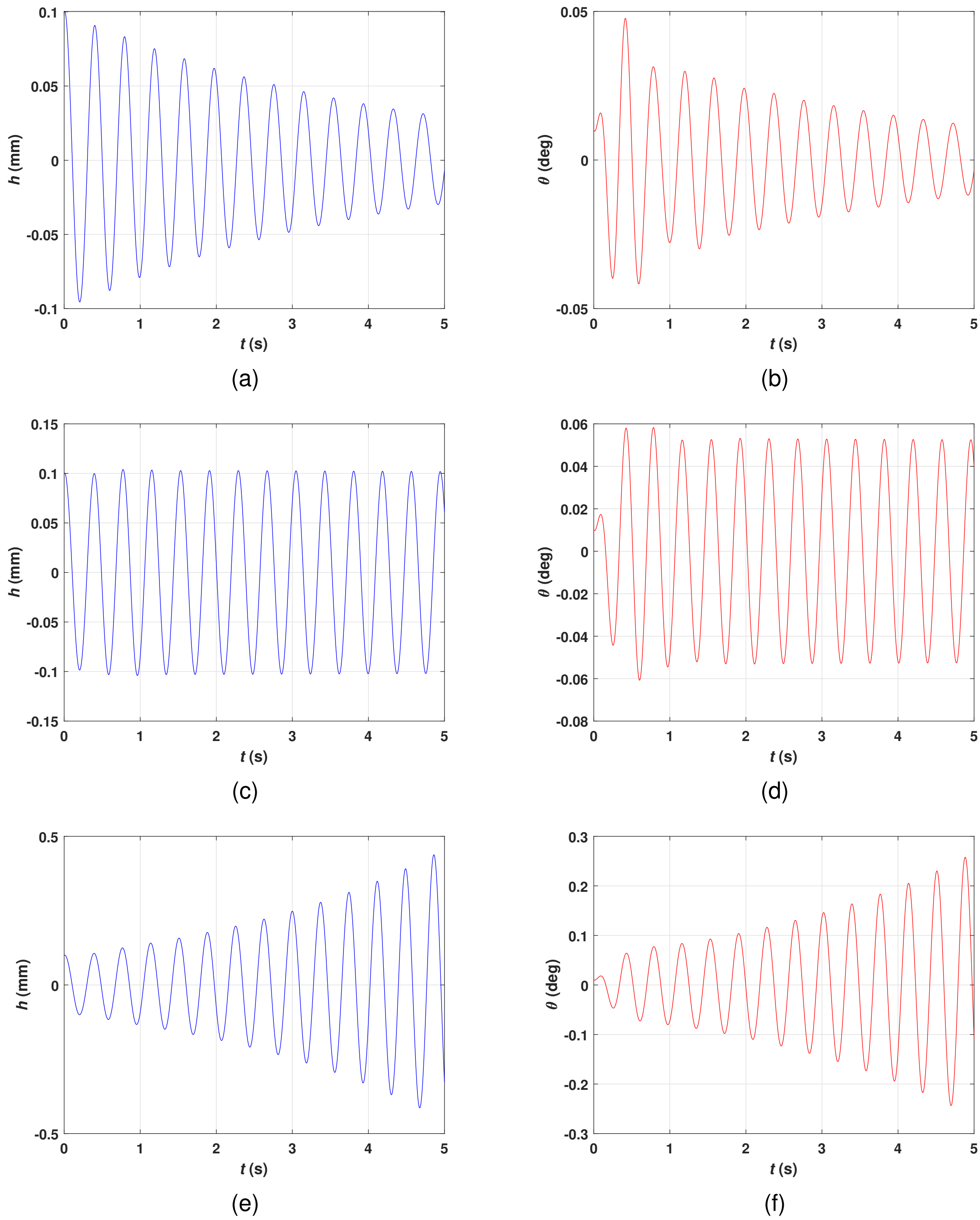

Figure 6.3 – Plunge and pitch time responses for the linear configuration without the piezoelectric circuit for the subcritical (a, b), critical (c, d) and supercritical regimes (e, f).

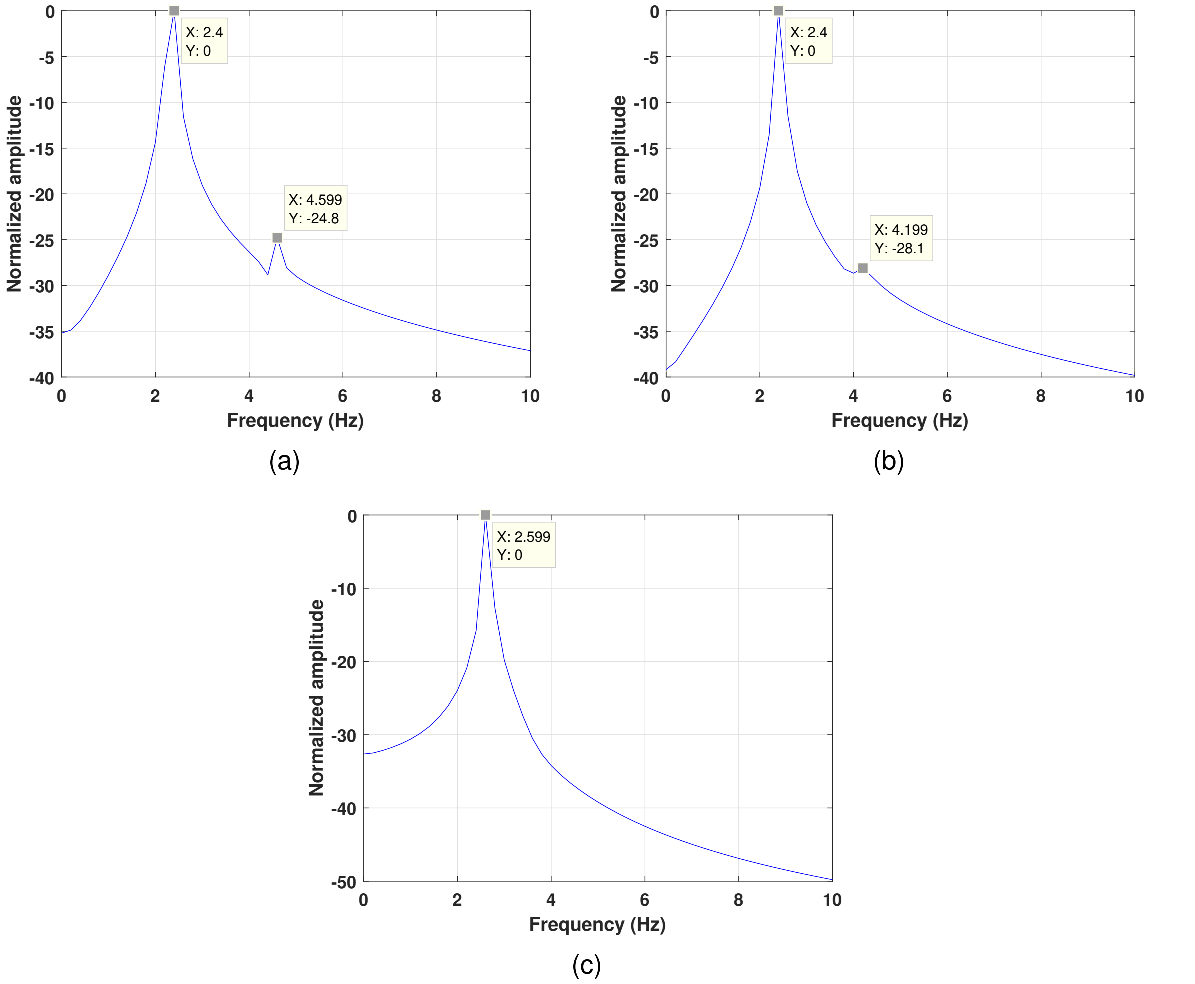

Figure 6.4 – FFT of the displacement time response at $V = 1.00$ m/s (a), $V = 10.00$ m/s (b), and $V = 14.01$ m/s (c).

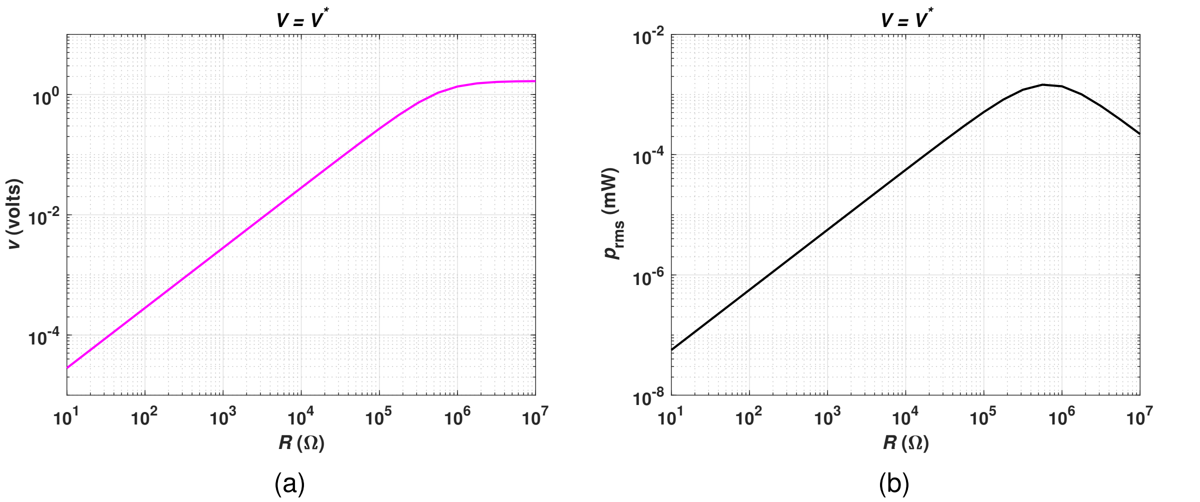

Figure 6.5 – Variation of the rms voltage (a), and power (b) with electrical resistance for harvesting at the linear flutter speed V^{*}.

limitation as it is able to provide persistent power only if the airspeed is kept constant at the critical value. Any reduction in V will imply a stable condition in which the system will eventually stop moving. On the other hand, for supercritical airspeeds, $V > V^*$, the associated unstable oscillation may cause a dynamic stall, which will also stop power output, or even structural damage as a result of the high-amplitude vibrations. Therefore, as discussed in the Introduction, structural nonlinearities will be incorporated into the piezoaeroelastic system to not only contain the supercritical response in the form of LCOs but also to reduce the CWS. Moreover, viscoelastic damping will also be proposed to control thee LCO amplitude and improve the system performance.

6.2 Parametric Study

To better understand the effect of each nonlinear effect and viscoelastic damping in the system, a parametric analysis is performed. In the next sections, to simplify the distinction between subcritical and supercritical regions, the results will display the normalized airspeed $\bar{V} = V/V^*$, where V^* is the critical flutter speed of the linear airfoil. Moreover, R is fixed at $R =$ 100 $\mathrm{k}\Omega$. This value was used as a reference for similar studies (ERTURK et al., 2010; ERTURK; INMAN, 2011). Furthermore, in Section 6.3, it will be shown that the optimal resistance for the nonlinear configuration with VEDs is on the order of kΩ.

6.2.1 Nonlinear configuration

The nonlinear configuration of the piezoaeroelastic system is obtained by adding combined hardening and free-play nonlinearities in the pitch and plunge stiffness terms, following Eq. 3.9. For this case, the state-space plot will not be available. Instead, bifurcation diagrams of the steady-state amplitude versus airspeed will be employed to visualize the effect of nonlinearity.

Taking into account only the hardening nonlinearity, ($h_{fp} =$ 0 mm, $\theta_{fp} =$ 0°), it is seen that adding the cubic stiffness terms a_1^θ and a_1^h creates an LCO (Fig. 6.6). This means that the vibration amplitude will be contained rather than continuously growing as in the linear case. Increasing a_1^θ at a given airspeed reduces the LCO amplitude for a constant a_1^h (Fig. 6.6). The higher stiffness in pitch is responsible for this effect, affecting both pitch and plunge because of their coupling.

The bifurcation diagrams of Fig. 6.7 allow the investigation of a_1^θ for the entire airspeed range. It is seen that the hardening in pitch can be used to control the vibration in the post-flutter regime, and hence extend the harvesting operational range in terms of airspeed. In fact, theoretically, a pure linear configuration would imply a vertical line in the bifurcation diagram at the flutter speed, meaning an infinite amplitude.

As a_1^θ is related to θ, the bifurcation curves for the pitch DOF display a typical hardening behavior (Fig. 6.7b). Due to the coupling of the DOF, the plunge bifurcation also reduces with increasing a_1^θ, but the curves display an almost linear variation with V (Fig. 6.7a). Moreover, since the piezoelectric coupling is in plunge, the voltage bifurcation follows the same behavior

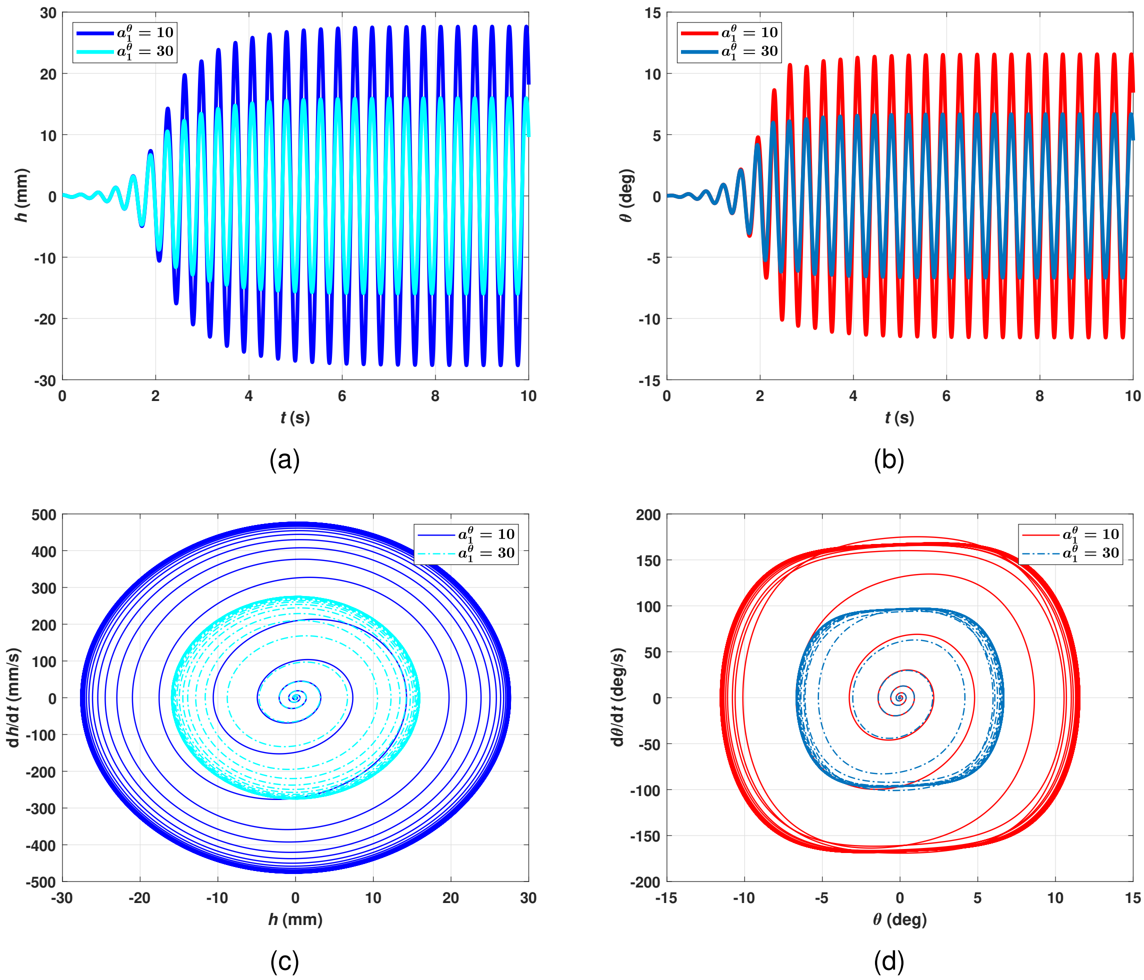

Figure 6.6 – Plunge and pitch time responses (a, b) and phase diagrams (c, d) at $\bar{V} = 1.2$ for $a_1^h = 1$ and varying a_1^θ.

as h (Fig. 6.7c). The negative effect of increasing a_1^θ is that, by reducing the vibration amplitude, less voltage and power are harvested (Fig. 6.7c, Fig. 6.7d). Therefore, there is a compromise between vibration control in post-flutter and energy harvesting.

Keeping a_1^θ constant and changing a_1^h, it is found that neither DOF is sensitive to the latter (Fig. 6.8). Thus, the hardening effect on plunge is unable to substantially change the dynamic behavior of the system. Hence, based on the results obtained so far, the following nonlinear reference configuration is proposed for the next investigations: $a_1^h = 1$ and $a_1^\theta = 10$.

If free-play is applied to the pitch DOF, there is a subcritical bifurcation (Fig. 6.9). The premature onset of flutter means that energy harvesting is favored by a lower CWS. In this sense, increasing θ_{fp} reduces the CWS to a certain point after which the CWS starts to increase with θ_{fp}. This suggests the existence of an optimal value for θ_{fp} in terms of the CWS.

A relevant effect of θ_{fp} for energy harvesting in Fig. 6.9 is that it substantially increases the voltage and power output for all airspeeds compared to the case without free-play. At $\bar{V} = 1$, the gain in power and voltage is of orders of magnitude, which favors energy harvesting. However, the vibration amplitude also increases accordingly. Thus, the compromise between

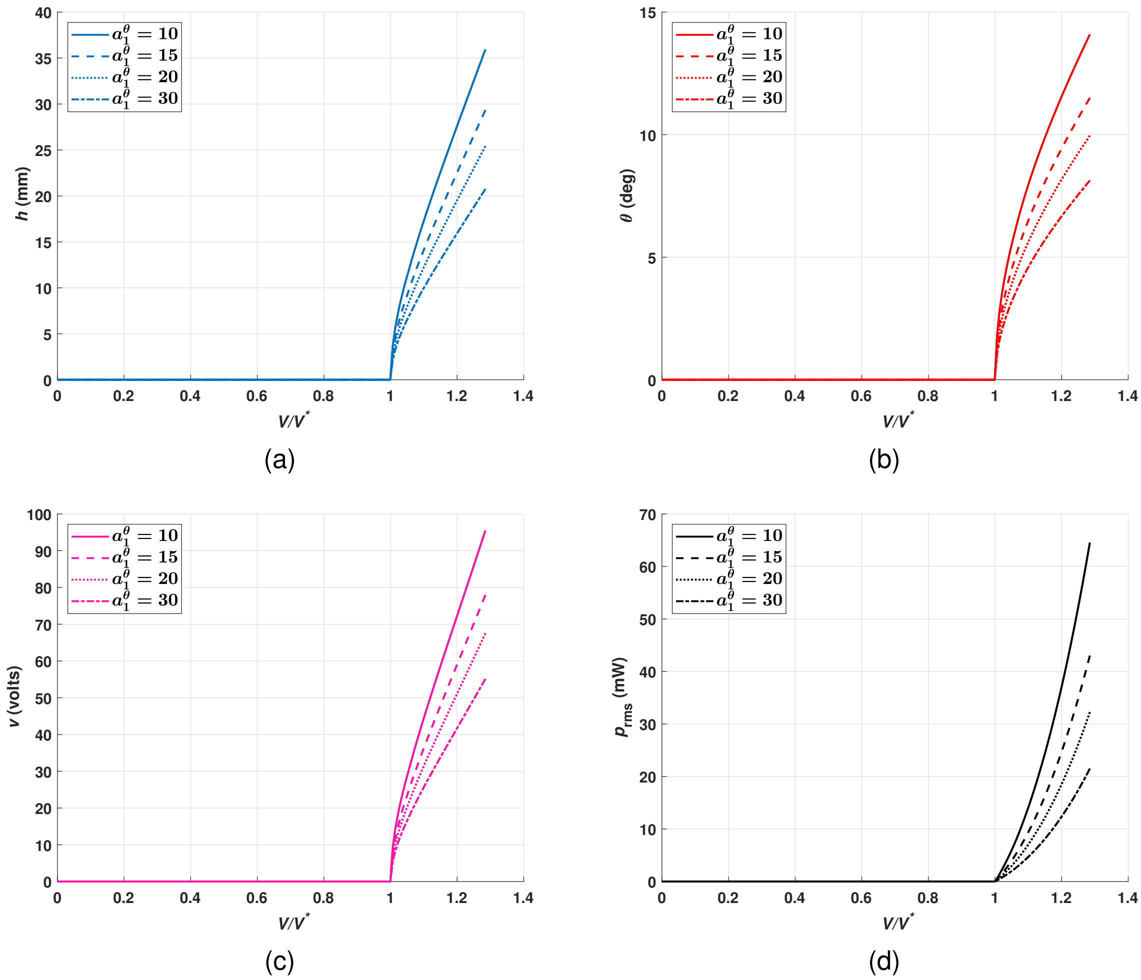

Figure 6.7 – Plunge (a), pitch (b), voltage (c) and power (d) bifurcation diagrams for $a_1^h = 1$ and a varying a_1^θ.

harvesting performance and vibration control is again observed.

As can be seen in Fig. 6.9, the bifurcation diagrams of the plunge, pitch, and voltage DOFs are similar when combined hardening and free-play in pitch are present. Hence, for a more concise exposition, not all DOF will be shown in the remainder of the parametric analysis.

Another implication of the subcritical bifurcation caused by the free-play nonlinearity in pitch is that different paths are found depending on the sweeping direction of airspeed (Fig. 6.10a, Fig. 6.10b). The CWS can be reduced in 40 % when $\bar{V}$ is swept downward. For harvesting, it is desirable that the paths match to secure this lowest CWS regardless of changes in airspeed. Fortunately, this can be achieved by adding free-play in the plunge DOF as well (Fig. 6.10c, Fig. 6.10d). Moreover, by adding h_{fp} the CWS reduces even further to less than 0.5 V^*. It is worth mentioning that, unless otherwise stated, the bifurcation diagram is obtained by incrementing $\bar{V}$.

The addition of free-play in the pitch and plunge DOFs changes the form of the bifurcation in the post-flutter region, leading to a rapidly increasing amplitude as $\bar{V}$ increases. This benefits harvesting, but may require control. In the next section, viscoelastic damping in the pitch and

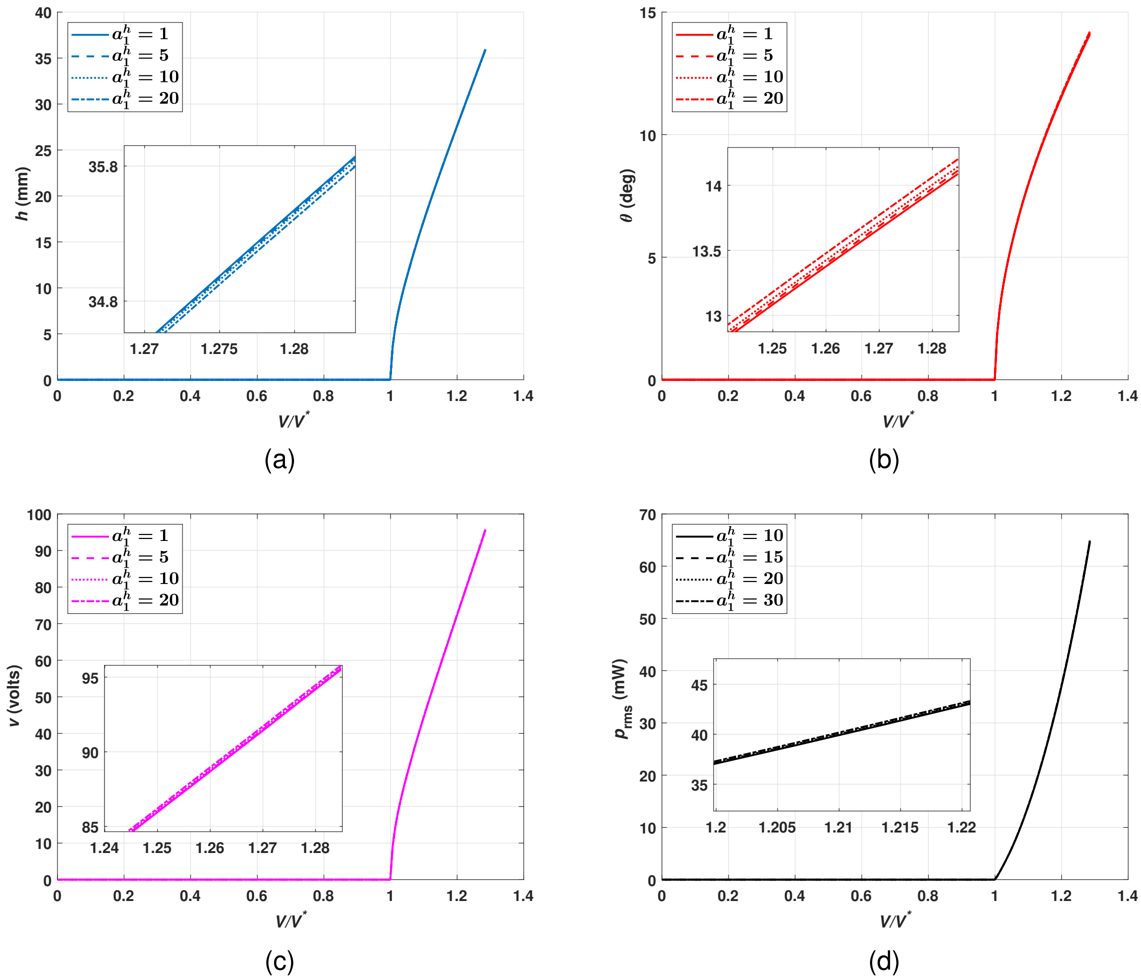

Figure 6.8 – Plunge (a), pitch (b), voltage (c) and power (d) bifurcation diagrams for $a_1^\theta = 1$ and a varying a_1^h.

plunge DOFs is proposed to that end, through the incorporation of the VEDs described in Chapter 4.

6.2.2 Nonlinear configuration with viscoelastic damping

In the previous section, the combination of nonlinearities was shown to be highly beneficial to FEH. However, it must be stated that it might result in complex dynamic behavior, particularly considering the presence of free-play in both DOF. In fact, it is known that aeroelastic systems with such characteristics may even exhibit chaotic nonlinear behavior (TIAN; Yang; Gu, 2017).

The power bifurcation diagram for a varying h_{fp} shows that increasing the amount of h_{fp} from 0.5 to 2 mm while keeping $\theta_{fp} = 1°$, results in unstable behavior in the subcritical region (Fig. 6.11a). At $\bar{V} = 0.6$, the time responses become aperiodic as h_{fp} increases to 2 mm (Fig. 6.12). The strongest effect seems to be in the pitch DOF (Fig. 6.12e). However, from a harvesting point of view, the voltage signal is the most important. Although it increases with h_{fp}, it is desirable to have a constant sinusoidal output in a wide range of airspeeds.

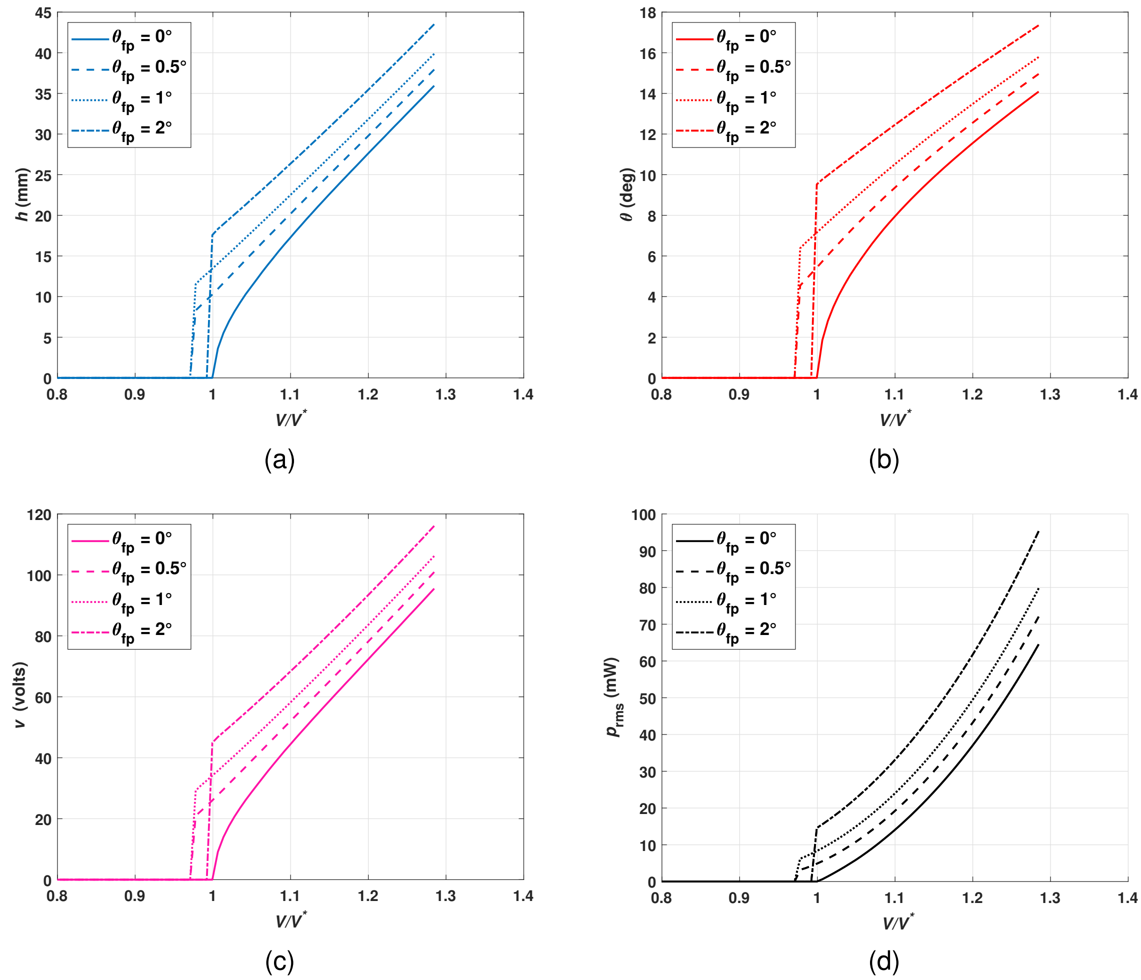

Figure 6.9 – Plunge (a), pitch (b), voltage (c) and power (d) bifurcation diagrams for $a_1^\theta = 10$, $a_1^h = 1$ and a varying θ_{fp}.

The complexity of the dynamic response for $h_{fp} = 2$ mm can be reduced by adding a VED in pitch (Fig. 6.11b), which is shown to stabilize the bifurcation, even for a small amount of viscoelastic material. Here, $t_v = R_e - R_i$ denotes the thickness of the VED in pitch, whose remaining dimensions are $l_\theta = 40$ mm and $R_i = 20$ mm. In addition, the plunge, pitch, and voltage responses become periodic because of the superior stiffness and damping provided by the VED.

When $t_v = 2$ mm, the VED is capable of further reducing the CWS due to the nontrivial relationship between stiffness and damping typical of nonlinear FEH systems. Another benefit of the VED is the increase in power output compared to the case without it ($t_v = 0$ mm) for most of the airspeed range (Fig. 6.11b). In fact, from Fig. 6.11b, there appears to be a compromise between widening the operational airspeed range, by reducing the CWS, and the average power output in this range.

Although the addition of the VED in pitch favored energy harvesting, a key feature of viscoelastic materials is their temperature dependence. Thus, to obtain a robust system, it is necessary to take into account variations in this parameter. Figure 6.13a shows that for one of the previous configurations ($h_{fp} = 2$ mm, $\theta_{fp} = 1°$, $t_v = 1$ mm) the stable behavior in the

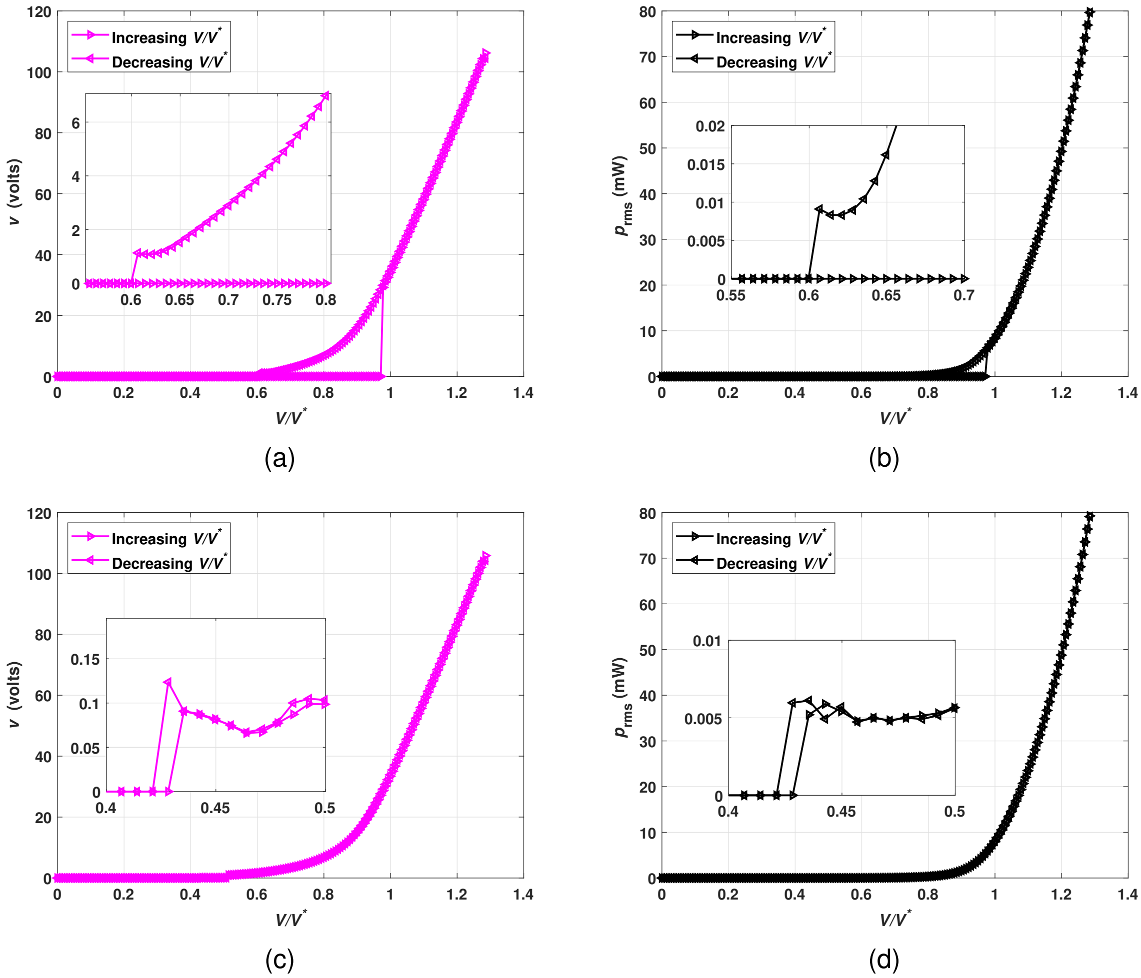

Figure 6.10 – Voltage and power bifurcation diagrams when sweeping $\bar{V}$ upward and downward for a combined nonlinear configuration ($\theta_{fp} = 1°$, $a_1^\theta = 10$, $a_1^h = 1$) with $h_{fp} = 0$ mm (a, b) and $h_{fp} = 0.5$ mm (c, d).

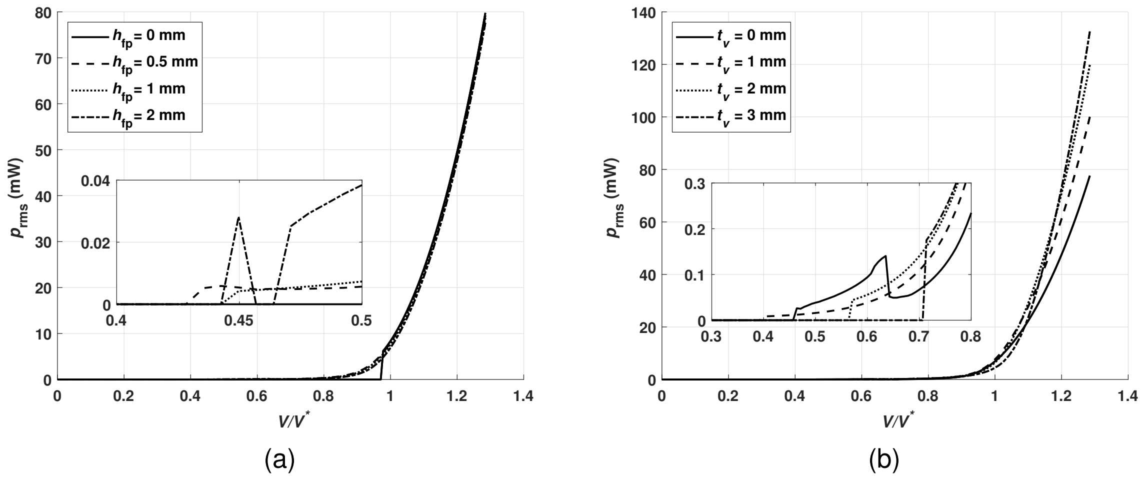

Figure 6.11 – Power bifurcation diagrams for a combined nonlinear configuration ($\theta_{fp} = 1°$, $a_1^\theta = 10$, $a_1^h = 1$) with varying h_{fp} (a) and varying t_v (b) for $h_{fp} = 2$ mm.

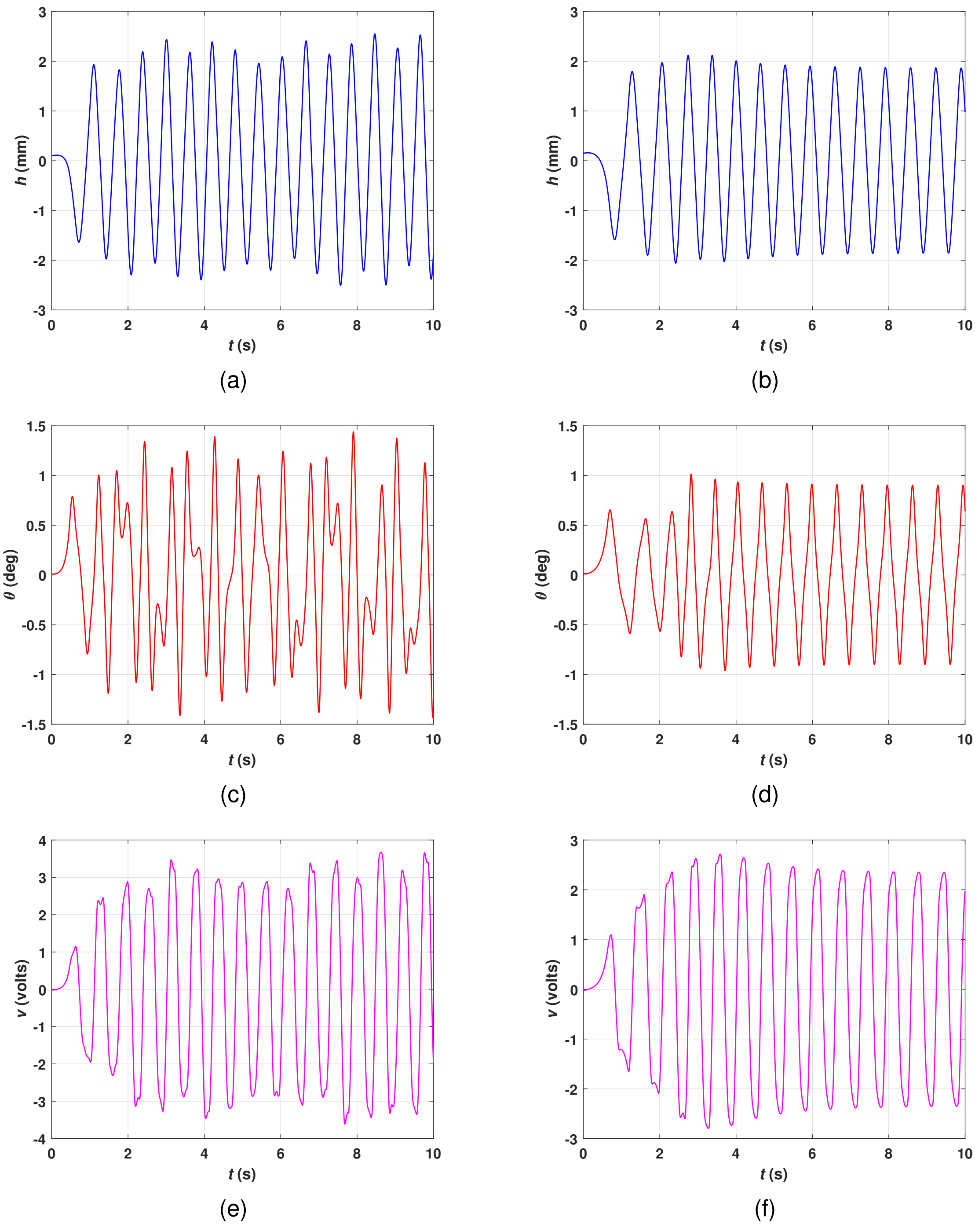

Figure 6.12 – Plunge, pitch and voltage time responses at $\bar{V} = 0.6$ for a combined nonlinear configuration ($h_{fp} = 2$ mm, $\theta_{fp} = 1^{\circ}$, $a_1^{\theta} = 10$, $a_1^{h} = 1$) without (a, c, e) and with the VED in pitch (b, d, f).

subcritical region is lost when the temperature T increases to 35 °C. In addition, the power output is lower at the higher temperature for most airspeeds. An opposite trend is observed by decreasing the temperature, as the associated superior stiffness in the pitch VED was shown to increase both power and the CWS (Fig. 6.11b, Fig. 6.13b).

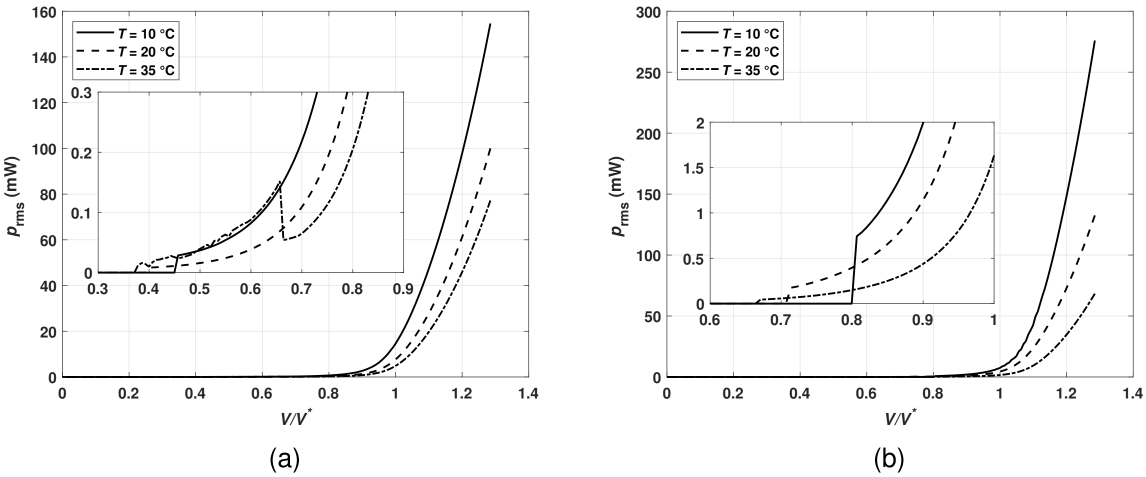

Figure 6.13 – Effect of temperature variation on power bifurcation diagrams for $t_v = 1$ mm (a) and $t_v = 3$ mm (b).

To enhance the robustness of the FEH system in relation to temperature, one can simply increase the thickness of the VED. For $t_v = 3$ mm, the power bifurcation diagram shows a stable behavior regardless of temperature, while keeping the CWS inferior to V^* (Fig. 6.13b). Again, the lower the temperature, the higher the VED stiffness and hence the output power. This power enhancement comes at the cost of increasing the CWS.

The combination of viscoelastic damping and structural nonlinearities proved to substantially benefit energy harvesting. However, in the supercritical region ($V^* > 1$), all previous bifurcation diagrams predict an ever-increasing vibration amplitude with airspeed. To prevent both dynamic stall and structural damage to the FEH system, a VED in the plunge DOF is proposed (Fig. 4.8).

For a geometry $l_x = 10$ mm, $l_y = 24$ mm and $l_z = 10$ mm, the effect of increasing the free-play gap of the VED in plunge (h^v_{fp}) is shown in Fig. 6.14 for all DOFs. The VED in pitch is kept ($l_\theta = 40$ mm, $t_v = 3$ mm, $R_i = 20$ mm) as well as the combined nonlinear configuration ($h_{fp} = 2$ mm, $\theta_{fp} = 1°$). It is seen that all bifurcation diagrams follow the same path until a given point where a jump is observed. After the discontinuity point, the vibration amplitude, voltage, and power increase to a value that is approximately constant with airspeed. This behavior is highly desirable from a harvesting perspective as maximum power and voltage are attained at lower airspeeds and the vibration amplitude is controlled. Furthermore, the use of combined nonlinearities ensures a subcritical bifurcation and thus a subcritical CWS.

Another relevant remark is that as h^v_{fp} increases, the airspeed at which the jump occurs is postponed, and the system achieves a superior vibration amplitude, voltage, and power. Therefore, there is a compromise between attaining higher voltage and power at a smaller airspeed and the maximum voltage and power possible. This is explained by the fact that h^v_{fp}

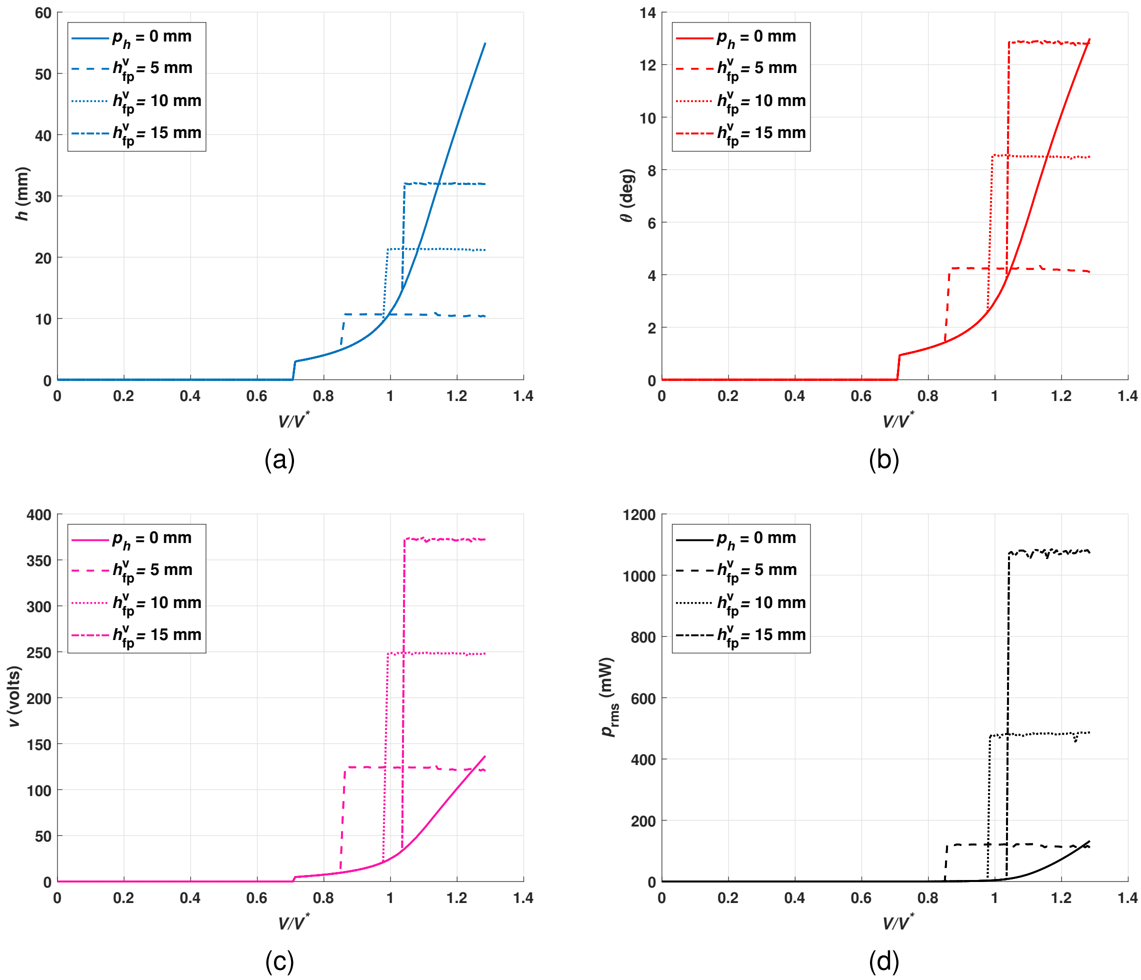

Figure 6.14 – Plunge (a), pitch (b), voltage (c) and power (d) bifurcation diagrams when varying h^v_{fp} for a combined nonlinear configuration (h_{fp} = 2 mm, θ_{fp} = 1 °, a^θ_1 = 10, a^h_1 = 1) and VEDs in pitch and plunge.

represents how much the system is allowed to vibrate without the influence of the VED in plunge. Thus, when the plunge amplitude reaches the value of h^v_{fp} (Fig. 6.15a) there is a sudden gain in stiffness due to the VED, causing the jump. An increase in vibration frequency is also observed and the system displays a sawtooth waveform (Fig. 6.15b). Moreover, the more complex signal creates small oscillations in the predicted amplitude.

Figure 6.16 shows the effect of the temperature variation for the configuration with VED in pitch and plunge when h^v_{fp} = 10 mm. As before, lower temperatures increase vibration amplitude, power output, and CWS, while lowering temperature has the opposite effect. The exception to this behavior is the pitch DOF, which has a more complex relationship with temperate. Fortunately, temperature variation cannot change the occurrence of a subcritical bifurcation nor affect considerably the vibration control in the post-flutter due to the advantageous combination of structural nonlinearities and viscoelastic damping.

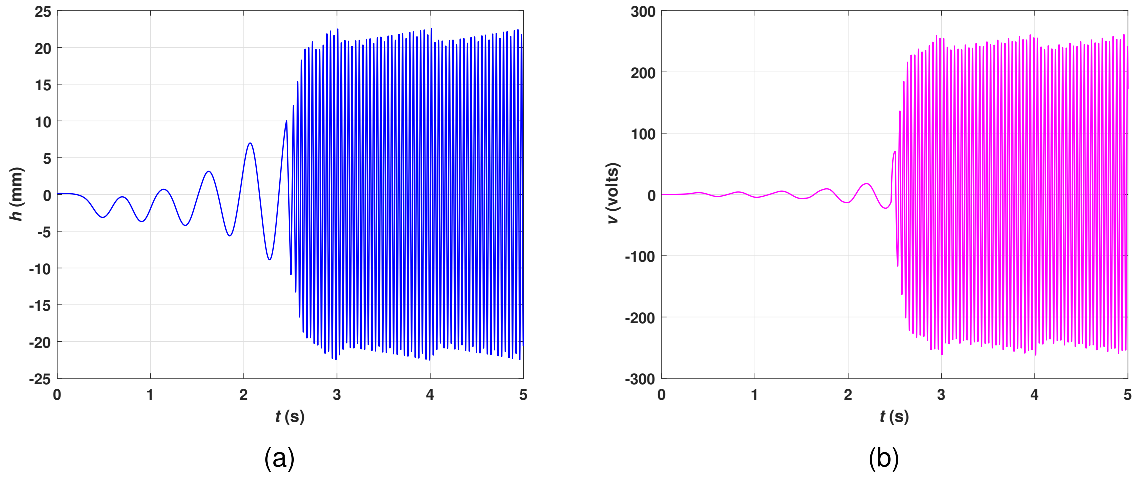

Figure 6.15 – Plunge (a) and voltage (b) time responses at $\bar{V} = 1.2$ for a combined nonlinear configuration ($h_{fp} = 2$ mm, $\theta_{fp} = 1°$, $a_1^{\theta} = 10$, $a_1^{h} = 1$) and VEDs in pitch and plunge.

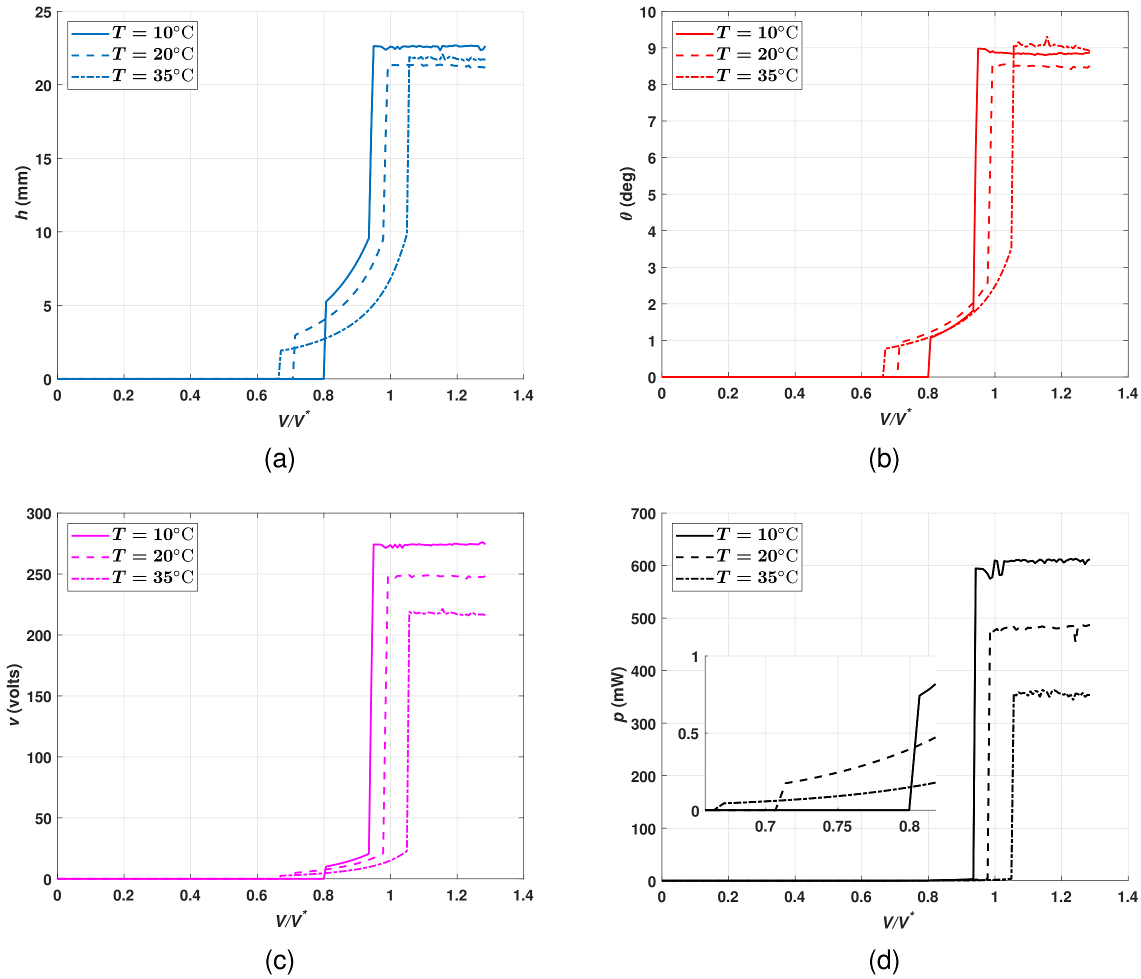

Figure 6.16 – Plunge (a), pitch (b), voltage (c) and power (d) bifurcation diagrams when varying T for a combined nonlinear configuration ($h_{fp} = 2$ mm, $\theta_{fp} = 1\,°$, $a_1^{\theta} = 10$, $a_1^{h} = 1$), VEDs in pitch and plunge, and $h_{fp}^{v} = 10$ mm.

6.3 Multi-objective Optimization

As discussed in the previous section, the best FEH performance is associated with high power output, low CWS, and a wide range of operational airspeeds. The former is defined as the difference between the airspeed associated with a given maximum allowed vibration amplitude and the CWS.

According to the definition of Eq. 5.1, the following deterministic optimization problem is proposed:

$$\begin{aligned} &\max \mathbf{y} = [p_m(\mathbf{x}),\ \Delta V(\mathbf{x})] \\ &\text{subjected to } \left\{\mathbf{x^L} \leq \mathbf{x} \leq \mathbf{x^U}\right. \end{aligned} \tag{6.1}$$

where $\mathbf{x} = \left[a_1^\theta,\ R,\ h_{fp}^v,\ p_\theta\right]$. Moreover, p_m represents the mean of the p_{rms} bifurcation diagram, calculated in the operating airspeed range, which is denoted by ΔV. This range is defined by the difference between the airspeed associated with a predefined vibration amplitude threshold in both pitch and plunge, V_{max}, and the CWS, $V_{\texttt{CWS}}$, such that $\Delta V = V_{max} - V_{\texttt{CWS}}$. In turn, V_{max} is defined formally as:

$$V_{max} = \min\left(V(h_{max}), V(\theta_{max})\right) \tag{6.2}$$

where h_{max} and θ_{max} are the admissible vibration amplitudes. The maximum admissible vibration amplitudes in pitch and plunge, θ_{max} and h_{max}, were defined from experimental studies of similar FEH systems found in the literature (PEREIRA et al., 2016; TIAN et al., 2021; TIAN et al., 2022) and are summarized in Table 6.2.

Table 6.2 – Admissible plunge and pitch vibration amplitudes.

Parameter	Absolute admissible value
$h_{max}(\texttt{mm})$	20
$\theta_{max}(^\circ)$	15

It should be mentioned that the temperature remains constant for the deterministic case, $T = 20$°C, as the geometric factor of the VED in plunge, $p_h = 24$ mm. Furthermore, the lower and upper limits of the design variables associated with the lateral constraints are summarized in Table 6.3, according to the intervals of interest.

Table 6.3 – Lateral constrains of the optimization problem.

Design variable (x_i)	Lower limit (x_i^L)	Upper limit (x_i^U)	Sample space
$a_1^\theta\,(-)$	0	30	linear
$R\,(\Omega)$	1×10^4	1×10^7	logarithmic
$h_{fp}^v\,(\texttt{mm})$	0	20	linear
$p_\theta\,(\texttt{m}^3)$	1.08×10^{-6}	1.02×10^{-4}	logarithmic

The lower and upper limits of p_θ correspond to the geometric configurations of Table 6.4. In addition, the parameters for the NSGA II optimization algorithm are summarized in Table 6.5. They were established considering previous experience of research studies carried out at LMEst when dealing with robust optimization of aeroelastic systems with energy harvesting feature (DINIZ, 2024).

Table 6.4 – Dimentions associated with the lower and upper limits fo p_θ.

Limit	p_θ (m³)	R_e (mm)	R_i (mm)	l_θ (mm)
Lower	1.08×10^{-6}	21	20	50
Upper	1.02×10^{-4}	30	20	10

Table 6.5 – NSGA II parameters.

Parameter	Value
Selection probability	0.25
Reproduction probability	0.25
Mutation probability	0.25
Generation count	100
Population count	50

6.3.1 Meta-model

To compute the objective functions of the proposed optimization problem defined in Eq. 6.1, one must obtain the bifurcation diagram associated with a given set of input parameters. The time domain analysis employed in this thesis means that, to obtain the bifurcation diagram, it is necessary to numerically integrate the equation of motion consecutively, until a steady-state regime is reached at each airspeed. As a consequence of this procedure, the cost required to perform even the deterministic optimization case would be prohibitive for a minimally sufficient population size and number of generations. Therefore, a NN metamodel is proposed to make the intended analysis feasible.

The Latin hypercube sampling (LHS) technique is used to efficiently generate random parameters in the range of interest (Table 6.3), following a uniform probability density function to represent the design space. For a given system configuration, a corresponding bifurcation diagram is generated for the plunge, pitch, voltage, and power DOFs. Hence, a sample consists of a four-point set associated with the four bifurcations, which are obtained from the direct time integration approach. For these bifurcations, V varies from 1 to 18 m/s with a step of 0.2 m/s. A point at 0.1 m/s is added to this array, totaling 87 discrete points. From the parametric analysis, this resolution was considered sufficient to represent the system behavior. It is important to note that because of the existence of the memory effects added by the viscoelastic material, the points of the bifurcation diagrams must be generated sequentially.

A total of 7,200 sets of bifurcation diagrams were generated which yielded 626,400 samples for the specified $\bar{V}$ refinement level. Around 58 hours were necessary to generate the data set in an Intel® core i5 7th gen processor. Although the sample number might seem high, the existence of jump discontinuities and a strong temperature dependence make the training of the NN a challenging task that requires a representative data set. Moreover, the time spent creating the data set is small compared to the amount that would be necessary to directly optimize the system.

Once the data set has been generated, the training procedure consists in adjusting the weights and biases according to the error of the expected and predicted outputs. Table 6.6 summarizes the architecture of the NN and its relevant parameters. The NN is composed of an input layer, two hidden layers, and an output layer with four outputs, namely, plunge, pitch, voltage, and power. All layers are dense and, thus, fully connected. The NN is created from the function *feedforwardnet*, available in Matlab®, according to the specifications in Table 6.6.

Table 6.6 – Neural network specification.

Designation	Number
Neurons in input layer	25
Neurons in first hidden layer	20
Neurons in second hidden layer	25
Neurons in output layer	4
Weights	700
Biases	74

In training the NN, the normalization of the input parameters is of fundamental importance, particularly because voltage and power display a variation of orders of magnitude. After extensive experimentation, normalization from the maximum and minimum values of each design variable yielded the best results. The proposed normalization scheme is given as

$$\bar{\mathbf{x}} = \frac{\mathbf{x} - \mathbf{x}_{\mathbf{min}}}{\mathbf{x}_{\mathbf{max}} - \mathbf{x}_{\mathbf{min}}} \tag{6.3}$$

where $\mathbf{x}_{\mathbf{min}}$ and $\mathbf{x}_{\mathbf{max}}$ are taken from the training set, and $\bar{\mathbf{x}}$ is the normalized input vector.

The training process is carried out using the Matlab® built-in function *train*, following a default configuration. Hence, 70 % of the training set is used for the training itself, 15 % for test, and 15 % for validation. The training set is used to adjust the weights and biases at each epoch. After each epoch, the training convergence is monitored by evaluating the validation set. If this set stops improving performance in terms of the MSE, the net is said to converge, and the weights associated with the best validation performance will be selected. Finally, the performance of the best configuration is evaluated in the test set. The default behavior of the *train* function is to also monitor performance in the test set at each epoch, although this does not influence the training procedure.

The evolution of the MSE for the training, validation, and test sets is shown in Fig. 6.17. Convergence is observed at the 107th epoch, which minimizes the MSE. Furthermore, the regression plots (Fig. 6.18) show the regression coefficient for the final values of each set, which are all close to the unit, as intended.

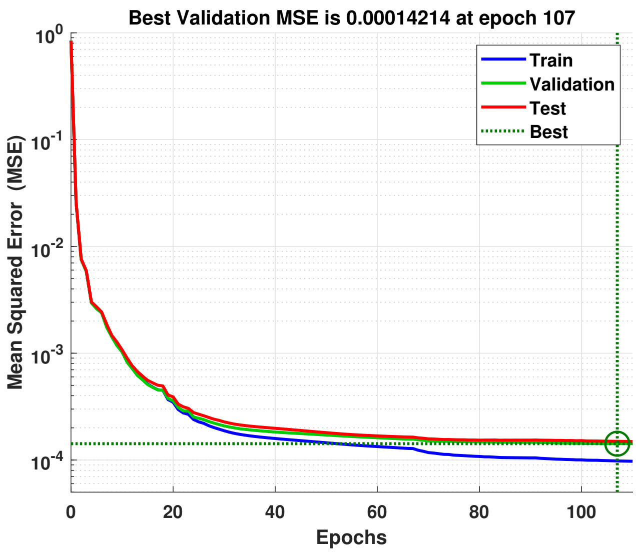

Figure 6.17 – Evolution of the MSE for the training, validation and test sets.

6.3.2 Deterministic case

Once the metamodel was established, the optimization can be carried out with a more refined airspeed vector. Hence, the step of V was reduced to 0.1 m/s. By solving the deterministic MOP proposed in Eq. 6.1, using the NSGA II parameters of Table 6.5, one obtains Fig. 6.19a.

The Pareto front is shown in Fig. 6.19b whose axes were inverted because the goal was to maximize the objectives. It has a complex shape, which highlights the need for an optimization-oriented design of the proposed FEH system. Between $p_m =$ 0 and 50 mW, it is concave, as expected in an MOP whose goal is to maximize both objectives. Next, there is a plateau from $p_m =$ 50 to 150 mW, after which the front becomes convex for most of the p_m axis. Finally, the Pareto front turns concave again around $p_m =$ 300 mW.

The design variables associated with the best compromise point (179.92, 11.5) according to the Min-Max method are listed in Table 6.7. Surprisingly, the optimal electrical resistance value, $R = 5.307 \times 10^4\ \Omega$, is considerably lower in relation to the one predicted by the linear system without VEDs, which was around $1 \times 10^6\ \Omega$. Furthermore, a_1^θ is close to its upper boundary, in accordance with the observed trend that increasing the stiffness of the pitch DOF benefits energy harvesting. The remaining variables all have intermediary values.

In Tab. 6.7 the values of the best possible p_m and ΔV are also listed together with their respective design variables. The best p_m configuration is closer to the best compromise, except for the value of p_θ.Increasing p_θ from 2.19×10^{-6} to 9.24×10^{-6} almost doubles the power output while halving the operational range of airspeeds. This shows how viscoelastic damping and stiffness alone can influence harvesting performance.

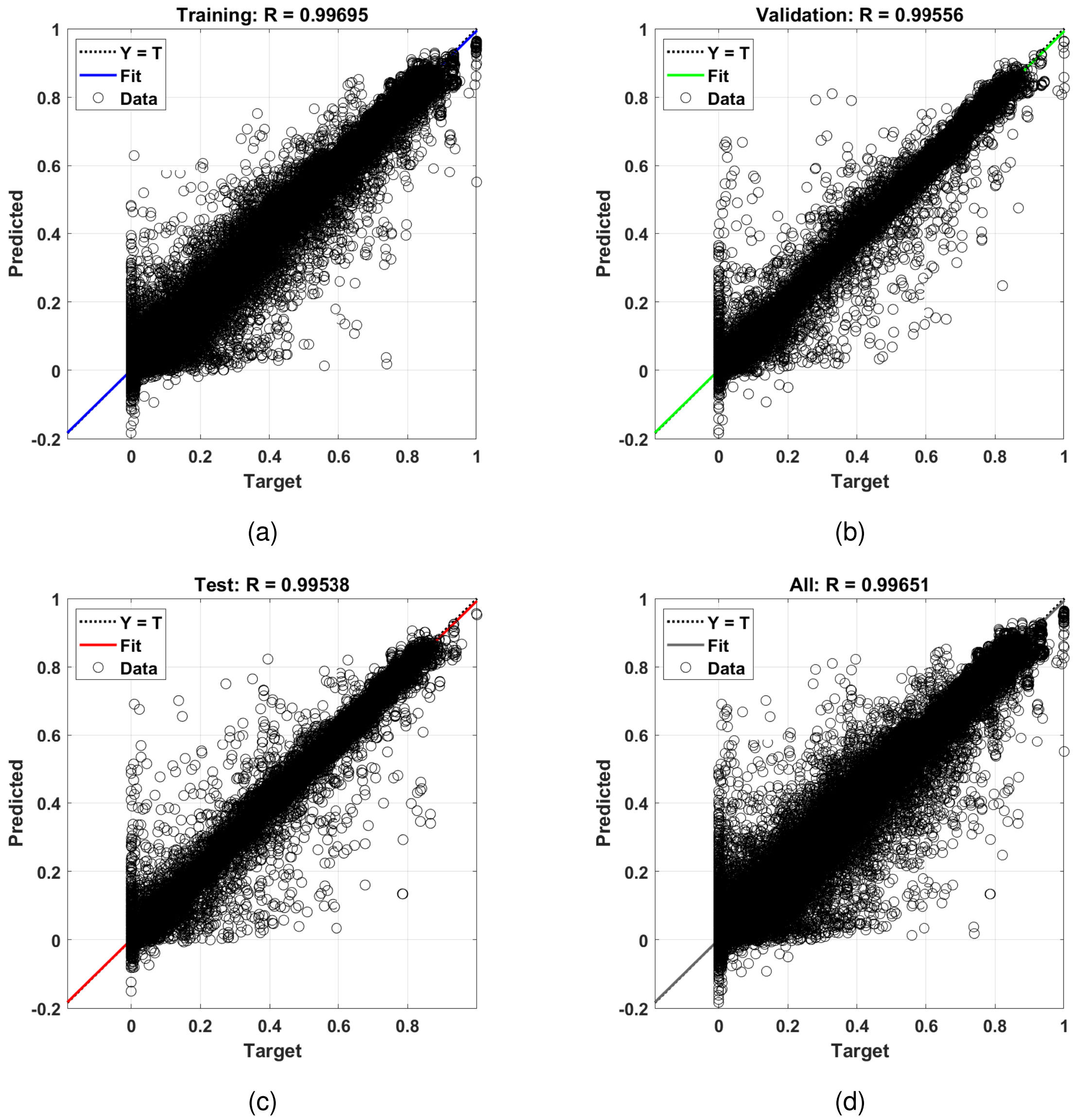

Figure 6.18 – Regression plots of the training (a), test (b), validation (c), and complete (d) sets.

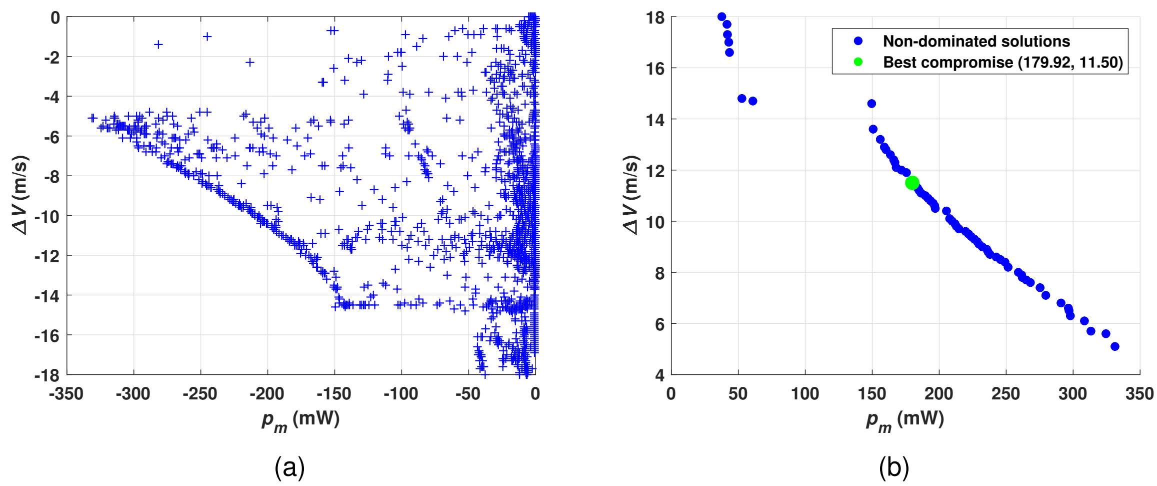

Figure 6.19 – Solutions in the objective space (a) and Pareto front (b) of the deterministic MOP.

Table 6.7 – Configurations and associated objective values of the best compromise, best ΔV, and best p_m for the deterministic MOP.

Deterministic MOP						
Point	Design variables				Objectives	
	a_1^θ	R (kΩ)	h_{fp}^v (mm)	p_θ (m^3)	p_m (mW)	ΔV (m/s)
Best compromise	27.24	53.07	9.27	2.19×10^{-6}	179.92	11.5
Best ΔV	15.66	273.39	8.89	6.66×10^{-6}	37.68	18.0
Best p_m	29.91	53.58	9.32	9.24×10^{-6}	331.24	5.1

All optimal configurations of Tab. 6.7 have a p_θ of the order of 10^{-6}, close to the lower limit for this parameter. This indicates that there is an upper limit to the dimensions of the VED in pitch, after which it starts to hinder the performance of the system. Furthermore, the best configuration for ΔV has a resistance of one order of magnitude higher than the other two to compensate for the lower power output. In contrast, the intensity of the hardening non-linearity in pitch (a_1^θ) is reduced for the best ΔV, shifting to the middle of its respective range. This highlights the difficulty in designing such FEH systems and the need for optimization techniques to achieve the best performance.

The bifurcation diagrams corresponding to the best compromise are shown in Fig. 6.20, as predicted by the metamodel and direct numerical integration. It is seen that the metamodel can reasonably represent the bifurcation diagrams, particularly for the pitch and plunge DOFs (Fig. 6.20a, Fig. 6.20b), although it underestimates voltage and power outputs (Fig. 6.20c, Fig. 6.20d). Fortunately, this is a conservative error. The performance of the metamodel can be improved by increasing the size of the data set.

It is clear that the plunge DOF is the most critical in terms of a safe operational airspeed range, as it reaches the admissible vibration amplitude of 20 mm, while the pitch DOF is far from the 15° threshold. Hence, since neither amplitude is exceeded (Fig. 6.20a), the VED on the plunge DOF was able to control vibration and extend the operation of the FEH system in the post-flutter regime, apart from substantially increasing the power output. This demonstrates the potential of the proposed FEH system and the design methodology adopted.

6.3.3 Robust case

Although the incorporation of the VEDs was shown to favor both energy harvesting and vibration control, it introduces a strong temperature dependence into the FEH system. In a practical application, the temperature is the parameter that can display the most substantial variation. Therefore, in the robust optimization case, the temperature is considered as a random variable following a Gaussian distribution. The mean value is the center of the interval 10°C to 35°C, and a variation of three standard deviations is assumed, meaning that 99.73 % of all data is included in the interval.

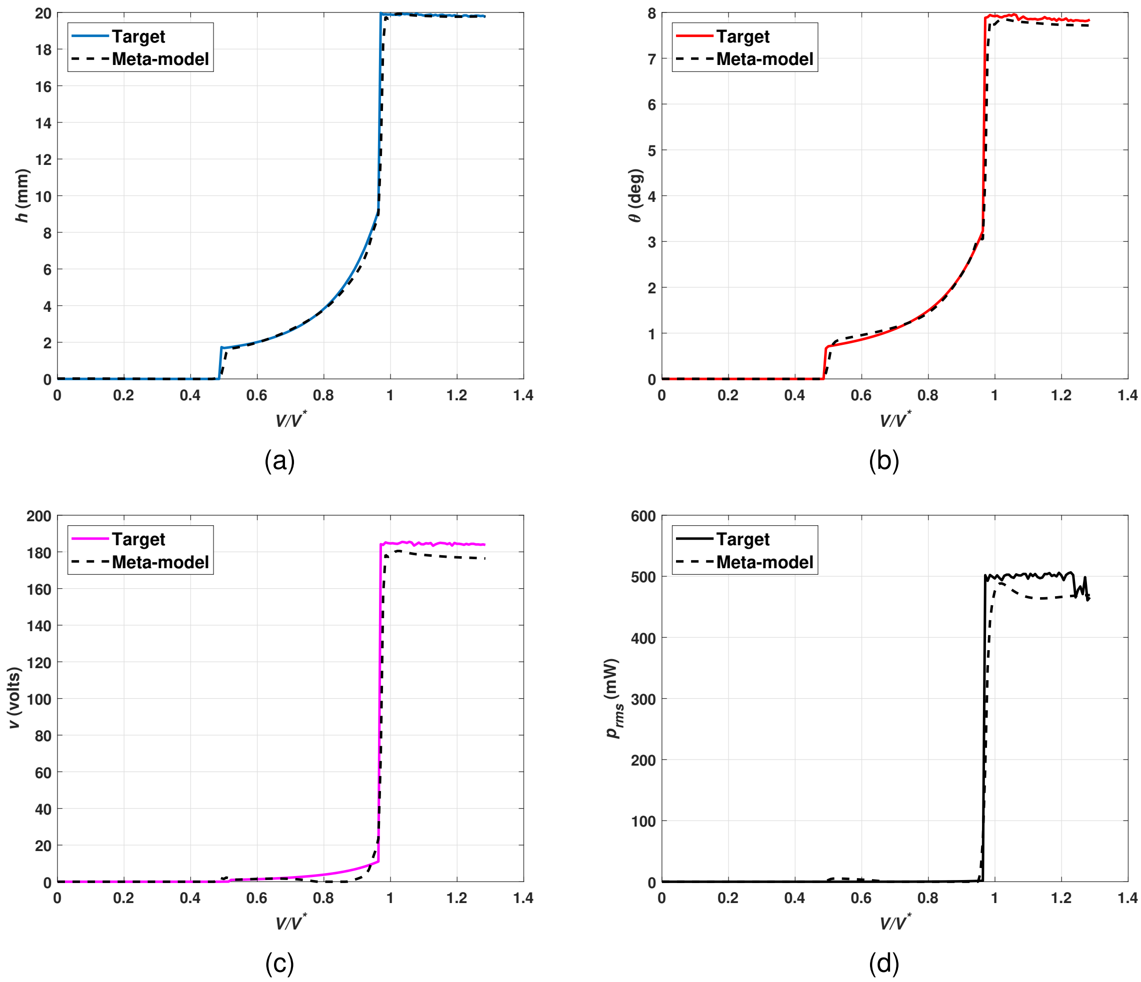

Figure 6.20 – Plunge (a), pitch (b), voltage (c) and power (d) bifurcation diagrams for the best compromise of the deterministic MOP.

A direct consequence of a random parameter is that the objectives will vary accordingly. The vulnerability functions associated with p_m and ΔV will become additional objectives in the MOP, doubling the number of objectives. Hence, the MOP becomes an RMOP, which is defined as follows:

$$\begin{aligned} &\min \mathbf{y} = [-\mu_p(\mathbf{x}),\ -\mu_{\Delta V}(\mathbf{x}),\ p_m^v(\mathbf{x}),\ \Delta V^v(\mathbf{x})] \\ &\text{subjected to } \left\{\mathbf{x}^{\mathbf{L}} \leq \mathbf{x} \leq \mathbf{x}^{\mathbf{U}}\right. \end{aligned} \tag{6.4}$$

where μ_p and $\mu_{\Delta V}$ are the means of p_m and ΔV, respectively. Moreover, the vulnerability functions in Eq. 6.4 are identified by the superscript v, and defined as the ratio of the standard deviation σ and the mean μ of the corresponding objective, as in Eq. 5.4. Hence, $p_m^v = \sigma_p/\mu_p$ and $\Delta V^v = \sigma_{\Delta V}/\mu_{\Delta V}$. As before, $\mathbf{x} = \left[a_1^\theta,\ R,\ h_{fp}^v,\ p_\theta\right]$. The objectives μ_p and $\mu_{\Delta V}$ were multiplied to minus one because the goal of the MOP is to maximize them while minimizing the vulnerability functions considered.

To compute the vulnerability functions, it is necessary to obtain a bifurcation diagram for each temperature sample so that the mean and standard deviation of the set of diagrams can be determined. This procedure substantially increases the optimization cost, according to the number of samples employed. In this study 20 temperature samples will be used. In addition, the airspeed vector step was increased to 0.2 m/s to reduce the simulation time.

For the same population of 50 individuals and 100 generations, the Pareto front of $\mu_{\Delta V}$ versus μ_p reveals a concave front as both objectives must be maximized, less complex than in the determinist case (Fig. 6.21a). The best compromise point for this curve is (114.00, 13.85) whose associated design variables are listed in Table 6.8. The coefficient a_1^θ reduces and moves away from its upper limit. In turn, the remaining design variables do not change substantially compared to the deterministic case, maintaining the same order of magnitude. The electrical resistance increases, while both h_{fp}^v and p_θ reduce.

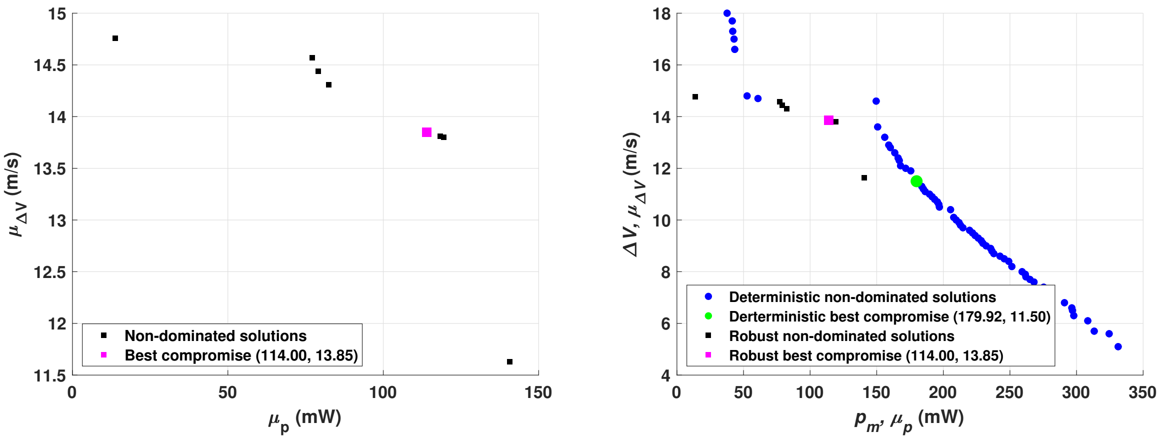

(a) (b)

Figure 6.21 – Pareto front of the RMOP (a) and comparison of the deterministic and robust Pareto fronts (b).

Table 6.8 – Configurations and associated objective values of the best compromise between $\mu_{\Delta V}$ and μ_p, best μ_p, and best $\mu_{\Delta V}$ for the RMOP.

Best compromise between $\mu_{\Delta V}$ and μ_p							
Design variables				Objectives			
a_1^θ	R (kΩ)	h_{fp}^v (mm)	p_θ (m³)	μ_p (mW)	$\mu_{\Delta V}$ (m/s)	p_m^v (mW^{-1})	ΔV^v (s/m)
18.89	77.53	8.33	1.08×10^{-6}	114.00	13.85	0.31	0.24
Best $\mu_{\Delta V}$							
a_1^θ	R (MΩ)	h_{fp}^v (mm)	p_θ (m³)	μ_p (mW)	$\mu_{\Delta V}$ (m/s)	p_m^v (mW^{-1})	ΔV^v (s/m)
0.00	8.31	8.66	1.08×10^{-6}	13.70	14.76	0.36	0.01
Best μ_p							
a_1^θ	R (kΩ)	h_{fp}^v (mm)	p_θ (m³)	μ_p (mW)	$\mu_{\Delta V}$ (m/s)	p_m^v (mW^{-1})	ΔV^v (s/m)
30.00	49.64	8.09	2.13×10^{-6}	140.67	11.63	0.49	0.02

According to Tab. 6.8, the best $\mu_{\Delta V}$ is associated with the lower limits of a_1^θ and p_θ. Although the resistance is on the order of MΩ, its mean power μ_p corresponds to an order of magnitude lower than the other optimal points. This objective can be favored by increasing the intensity of the hardening coefficient in pitch to yield the best compromise point. An additional gain in μ_p is obtained by further increasing a_1^θ and adding the VED to the pitch DOF, as suggested by the best μ_p configuration.

Another observation is that, except for the best compromise, the best $\mu_{\Delta V}$ and the best μ_p have vulnerability functions ΔV^v considerably smaller than their p_m^v counterparts, which are always above 30 %. Thus, power is shown to be more sensitive to temperature variations than ΔV. The variation of $\mu_{\Delta V}$ from 11.63 to 14.76 m/s (only about 14 %) also supports this conclusion.

To show the robustness of the RMOP solution, the power bifurcation diagram corresponding to its best compromise configuration is shown in Fig. 6.22 for the lower and upper temperature limits, 10°C and 35°C, respectively. Although there is a considerable power variation with temperature, the maximum power varies from 277.0 to 759.0 mW (about 174 %), for the deterministic case, and from 246.8 to 517.4 mW (110 %), for the robust case, representing a 64 % reduction. Hence, as intended, the solution of the RMOP reduced the objective variation.

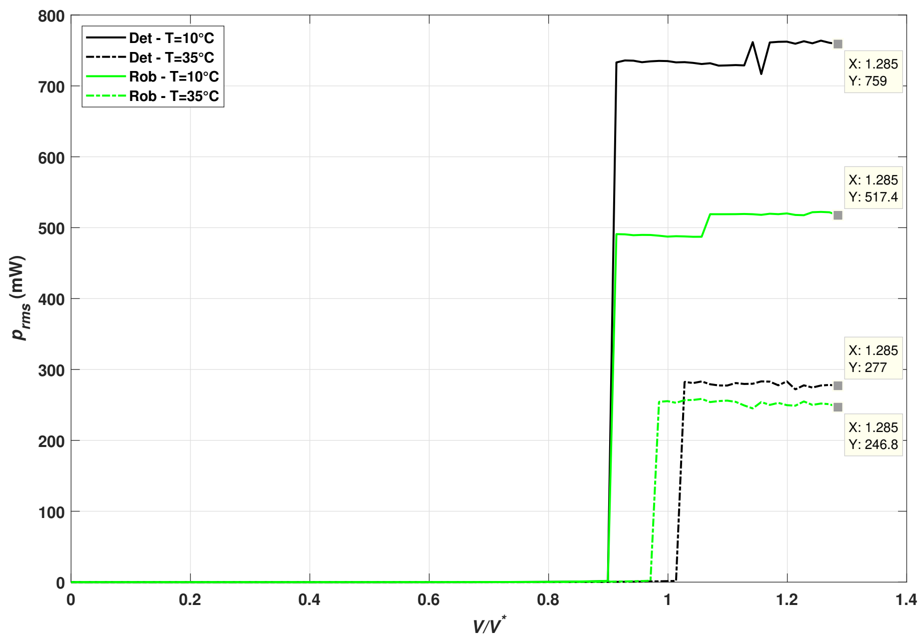

Figure 6.22 – Power bifurcation diagrams for the best deterministic (Det) and robust (Rob) compromise configurations.

The Pareto fronts of the vulnerability functions are shown in Fig. 6.23a and Fig. 6.23b. It is evident that the best FEH performance in terms of μ_p and $\mu_{\Delta V}$ will result in a higher vulnerability. In contrast, improved robustness will imply lower performance. Furthermore, the power standard deviation is shown to vary up to 50 % of its mean, while the maximum variation for ΔV is less than 1.3 %. Therefore, power is considerably more sensitive to temperature variation than ΔV^v.

The best configurations for p_m^v and for the best compromise between p_m^v and μ_p of

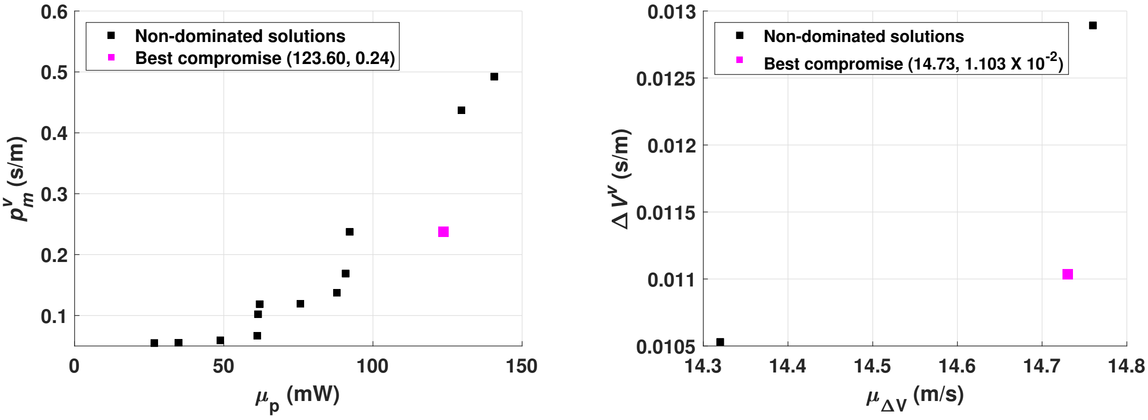

(a) (b)

Figure 6.23 – Pareto fronts of the vulnerability functions p_m^v (a) and ΔV^v (b).

Fig. 6.23a are listed in Tab. 6.9. The best configuration for μ_p is the same as in Tab. 6.8, repeated here for convenience. It is clear that the best value of p_m^v is associated with the least amount of viscoelastic material. This is a reasonable outcome as the variations in the objectives are induced by the change in the temperature-dependent properties of the VED. Hence, minimizing the vulnerability functions implies reducing p_θ. Another aspect is that prioritizing p_m^v substantially reduces μ_p and favors $\mu_{\Delta V}$.

Table 6.9 – Configurations and associated objective values of the best compromise between p_m^v and μ_p, best p_m^v, and best μ_p for the RMOP.

Best compromise between p_m^v and μ_p							
Design variables				Objectives			
a_1^θ	R (kΩ)	h_{fp}^v (mm)	p_θ (m³)	μ_p (mW)	$\mu_{\Delta V}$ (m/s)	p_m^v (mW^{-1})	ΔV^v (s/m)
20.17	8.95	6.89	8.07×10^{-6}	123.63	7.57	0.24	0.25
Best p_m^v							
a_1^θ	R (kΩ)	h_{fp}^v (mm)	p_θ (m³)	μ_p (mW)	$\mu_{\Delta V}$ (m/s)	p_m^v (mW^{-1})	ΔV^v (s/m)
18.89	279.39	5.71	1.08×10^{-6}	26.71	14.42	0.05	0.02
Best μ_p							
a_1^θ	R (kΩ)	h_{fp}^v (mm)	p_θ (m³)	μ_p (mW)	$\mu_{\Delta V}$ (m/s)	p_m^v (mW^{-1})	ΔV^v (s/m)
30.00	49.64	8.09	2.13×10^{-6}	140.67	11.63	0.49	0.02

The best compromise has a greater p_θ that results in a higher ΔV^v compared to the other two points. Since the resistance of the best compromise (8.95 kΩ) is less than 20 % of that associated with the best μ_p (49.64 kΩ), its p_m^v is about half of that related to the best μ_p. Hence, the magnitude of the resistance also increases the vulnerability of power, together with p_θ.

For Fig. 6.23b a table in the for of Tab. 6.9 and Tab. 6.8 is not provided as the Pareto front corresponding to ΔV^v and $\mu_{\Delta V}$ features small variation.

CHAPTER VII

FINAL REMARKS AND FUTURE WORK PERSPECTIVES

As discussed in the Introduction, the nonlinear behavior is fundamental to achieve the feasibility of FEH systems. At the same time, viscoelastic damping was shown to be a promising aeroelastic passive control technique. Hence, the present thesis proposed the combination of hardening and free-play structural nonlinearities together with viscoelastic dampers to improve the energy harvesting performance of a two-DOF airfoil with piezoelectric transduction. In addition to a parametric analysis, the robust multi-objective optimization of the FEH system was also performed.

To accomplish the proposed study, the nonlinear equation of motion of the piezoaeroelastic system was formulated from the Lagrange equations and directly integrated in time with a combined Newton-Raphson and Newmark method. The feasibility of the time domain analysis of the system with viscoelastic damping required the use of a recurrent FDM approach. Moreover, potential unsteady aerodynamics based on the convolution of the Wagner function was used to represent an arbitrary aerodynamic load. Finally, deterministic and robust optimization cases were performed using a NN metamodel.

The proposed study is unprecedented in the literature, thus highlighting its novelty and contribution to the field, representing a natural continuation of the research activities developed at LMEst and FEMTO-ST. By the time the writing of this manuscript was complete, two research papers were published directly related to the present work (LIMA et al., 2025; DELGADO FILHO et al., 2025).

7.1 Final remarks

As a result of this work, the following conclusions became evident, which are valuable for guiding future research studies:

- For the linear piezoaeroelastic configuration, the output voltage increases with electrical resistance R. In contrast, the optimal power is associated with a particular R;
- The addition of the hardening nonlinearity alone creates a supercritical Hopf bifurcation, yielding a LCO in the post-flutter regime;

- For a nonlinear configuration with only the hardening effect, there is a compromise between controlling the vibration amplitude in the post-flutter and both voltage and power outputs;
- It is suggested that the hardening influence is system-dependent, and its relevance may vary depending on the damping and stiffness of each DOF. For the system considered, only the pitch hardening coefficient was able to substantially impact its behavior;
- The combination of free-play with hardening was shown to reduce the CWS and increase substantially voltage and power;
- If only free-play in pitch is combined to the hardening nonlinearity, different paths are found for the bifurcation diagrams depending on the direction in which the airspeed is swept;
- By adding free-play in pitch and plunge to hardening, the difference between the paths in the bifurcation diagrams is eliminated regardless of the sweeping direction of airspeed;
- The complexity of the dynamic response associated with a nonlinear configuration with hardening and free-play in both pitch and plunge DOFs, can be reduced by the incorporation of a viscoelastic damping in pitch, making the time response periodic;
- The addition of viscoelastic damping can reduce the CWS and increase voltage and power output;
- The amount of viscoelastic damping can be tuned to conserve the favorable harvesting features regardless of temperature variations;
- A viscoelastic damper in plunge with free-play can be used to control the LCO amplitude in the post flutter regime and to substantially increase voltage and power output;
- The optimization of the FEH system by direct time integration requires the use of meta modeling techniques;
- A MLP NN can yield a reasonable metamodel of the system;
- Power is considerably more sensitive to temperature variation than the operational airspeed range;
- Increasing the electrical resistance and the dimension of the VED in pitch increases the vulnerability functions;
- The proposed design methodology serves as a preliminary study for the development of FEH with robust-optimal performance.

7.2 Future works perspectives

The results obtained in this thesis motivate further research concerning the use of viscoelastic damping to control aeroelastic LCOs from the perspective of piezoelectric energy harvesting. The following research directions are suggested:

- Perform an experimental validation of the proposed model, as the presented analysis was exclusively numeric;
- Perform a fatigue analysis of the system, given its operation in cyclic loading due to the LCO;
- Evaluate the system performance in terms of noise, an important operational aspect;
- Perform a sensitivity non dimensional analysis of the system;
- Apply the model to more complex structures, including a three-DOF airfoil with a control surface dof and three dimensional wing configurations. This second can be conveniently achieved by the strip theory;
- Evaluate the harvesting performance and system dynamics under time-varying flow speed to simulate a real environmental flow condition;
- Add nonlinear aerodynamic effects such as dynamic stall to extend the investigation of the system performance to higher airspeeds;
- Extend analysis range regarding temperature, particularly to negative values;
- Investigate the degradation of the viscoelastic material with time, particularly in terms of stiffness and damping;
- Include the geometric parameters of the airfoil in the parametric analysis and optimization scheme to expand the design space;
- Propose an analytical or semi-analytical approach to model the system behavior;
- Investigate the effect of nonlinearities in the piezoelectric material;
- Increase the fidelity of the aerodynamic model by adding CFD to include more complex nonlinear aerodynamic effects in the analysis and, hence, extend the airspeed range considered.

BIBLIOGRAPHY

ABDEHVAND, M. Z.; ROKNIZADEH, S. A. S.; MOHAMMAD-SEDIGHI, H. Modeling and analysis of novel coupled magneto-electro-aeroelastic continuous system for flutter-based energy harvesting system. *Energy*, v. 230, p. 120742, 2021. DOI: <https://doi.org/10.1016/j.energy.2021.120742>.

ABDELKEFI, A. Aeroelastic energy harvesting: A review. *International Journal of Engineering Science*, v. 100, p. 112–135, 2016. DOI: <https://linkinghub.elsevier.com/retrieve/pii/S0020722515001482>.

ABDELKEFI, A.; NAYFEH, A. H.; HAJJ, M. R. Modeling and analysis of piezoaeroelastic energy harvesters. *Nonlinear Dynamics*, v. 67, p. 925–939, 2012. DOI: <http://link.springer.com/10.1007/s11071-011-0035-1>.

ABDELKEFI, A. et al. An analytical and experimental investigation into limit-cycle oscillations of an aeroelastic system. *Nonlinear Dynamics*, v. 71, p. 159–173, 2013. DOI: <http://link.springer.com/10.1007/s11071-012-0648-z>.

AMARAL, A. C. G.; DE MARQUI, C.; SILVEIRA, M. Aeroelastic energy harvesting in flutter condition increases with combined nonlinear stiffness and nonlinear piezoelectrical coupling. *Journal of the Brazilian Society of Mechanical Sciences and Engineering*, v. 45, p. 111, 2023. DOI: <https://link.springer.com/10.1007/s40430-023-04028-w>.

ANDERSON JUNIOR, J. D. *Fundamentals of aerodynamics.* 5th. ed. [S.l.]: McGraw-Hill, 2011. 1106 p.

AVILA, E. *Estudo do cálculo fracionário aplicado à modelagem de sistemas vibratórios com amortecimento viscoelástico*. Thesis (PhD) — Universidade Federal de Uberlândia, 2010. DOI: <https://repositorio.ufu.br/handle/123456789/14890>.

BAGLEY, R. L.; TORVIK, P. J. On the fractional calculus model of viscoelastic behavior. *Journal of Rheology*, v. 30, p. 133–155, 1986. DOI: <https://pubs.aip.org/sor/jor/article/30/1/133-155/235577>.

BASTA, E.; GHOMMEM, M.; EMAM, S. Flutter control and mitigation of limit cycle oscillations in aircraft wings using distributed vibration absorbers. *Nonlinear Dynamics*, v. 106, p. 1975–2003, 2021. DOI: <https://doi.org/10.1007/s11071-021-06889-z>.

BENI, Z. T.; BENI, Y. T. Dynamic stability analysis of size-dependent viscoelastic/piezoelectric nano-beam. *International Journal of Structural Stability and Dynamics*, v. 22, 2022. DOI: <https://www.worldscientific.com/doi/10.1142/S021945542250050X>.

BERAN, P.; STANDFORD, B.; SCHROCK, C. Uncertainty quantification in aeroelasticity. *Annual Review of Fluid Mechanics*, v. 49, p. 361–386, 2017. DOI: <https://doi.org/10.1146/annurev-fluid-122414-034441>.

BISPLINGHOFF, R. L.; ASHLEY, H. *Principles of Aeroelasticity*. [S.l.]: Dover Publications, Inc, 1975.

BLAIR, M. *A compilation of the Mathematics Leading to the Doublet Lattice Method*. [S.l.], 1992. v. 48, 1091-1104 p.

BONNIN, M.; TRAVERSA, F. L.; BONANI, F. Leveraging circuit theory and nonlinear dynamics for the efficiency improvement of energy harvesting. *Nonlinear Dynamics*, v. 104, p. 367–382, 2021. DOI: <https://link.springer.com/10.1007/s11071-021-06297-3>.

BORGES, D. *Desenvolvimento de uma metodologia de análise da estabilidade de sistemas aeroviscoelásticos empregando o método Doublet Lattice*. Thesis (Master) — Universidade Federal de Uberlândia, 2019. DOI: <https://doi.org/10.14393/ufu.di.2019.2374>.

BOUMA, A. et al. Effective design and characterization of flutter-based piezoelectric energy harvesters with discontinuous nonlinearities. *Energy*, v. 238, p. 121662, 2022. DOI: <https://linkinghub.elsevier.com/retrieve/pii/S0360544221019101>.

BRYANT, M.; GARCIA, E. Development of an aeroelastic vibration power harvester. In: AHMADIAN, M.; GHASEMI-NEJHAD, M. N. (Ed.). *Proceedings Volume 7288, Active and Passive Smart Structures and Integrated Systems*. [s.n.], 2009. p. 728812. DOI: <http://proceedings.spiedigitallibrary.org/proceeding.aspx?doi=10.1117/12.815785>.

BRYANT, M.; GARCIA, E. Energy harvesting: a key to wireless sensor nodes. In: LENG, J.; ASUNDI, A. K.; ECKE, W. (Ed.). *Proceedings Volume 7493, Second International Conference on Smart Materials and Nanotechnology in Engineering*. [s.n.], 2009. p. 74931W. DOI: <http://proceedings.spiedigitallibrary.org/proceeding.aspx?doi=10.1117/12.845784>.

BRYANT, M.; GARCIA, E. Modeling and testing of a novel aeroelastic flutter energy harvester. *Journal of Vibration and Acoustics*, v. 133, 2011. DOI: <https://asmedigitalcollection.asme.org/vibrationacoustics/article/doi/10.1115/1.4002788/469605/Modeling-and-Testing-of-a-Novel-Aeroelastic>.

CARVALHO, P. A. N. de. *Projeto ótimo robusto de sistemas aeroviscoelásticos estocásticos em regime subsônico utilizando Doublet Lattice*. Thesis (PhD) — Universidade Federal de Uberlândia, 2024. DOI: <https://repositorio.ufu.br/handle/123456789/41723>.

CHEN, M. et al. Flutter analysis of a flag of fractional viscoelastic material. *Journal of Sound and Vibration*, v. 333, p. 7183–7197, 2014. DOI: <https://linkinghub.elsevier.com/retrieve/pii/S0022460X14006968>.

CHRISTENSEN, R. M. *Theory of Viscoelasticity*. 2. ed. Academic Press, 1982. 364 p. DOI: <https://www.sciencedirect.com/book/9780121742522/theory-of-viscoelasticity?via=ihub=https://linkinghub.elsevier.com/retrieve/pii/B9780121742522X50017>.

CINIELLO, A. P. D. *Aplicação do Cálculo Fracionário na Identificação do Módulo de Relaxação de Materiais Viscoelásticos no Domínio do Tempo*. 156 p. Thesis (PhD) — Universidade Federal do Paraná, 2016.

CLARIVATE ANALYTICS. *Web of Science*. 2025.

CUNHA FILHO, A. et al. A new and efficient constitutive model based on fractional time derivatives for transient analyses of viscoelastic systems. *Mechanical Systems and Signal Processing*, v. 146, p. 107042, 2021. DOI: <https://linkinghub.elsevier.com/retrieve/pii/S0888327020304283>.

CUNHA FILHO, A. et al. Flutter suppression of plates subjected to supersonic flow using passive constrained viscoelastic layers and golla–hughes–mctavish method. *Aerospace Science and Technology*, v. 52, p. 70–80, 2016. DOI: <https://doi.org/10.1016/j.ast.2016.02.022>.

CUNHA FILHO, A. et al. Flutter suppression of plates using passive constrained viscoelastic layers. *Mechanical Systems and Signal Processing*, v. 79, p. 99–111, 2016. DOI: <https://doi.org/10.1016/j.ymssp.2016.02.025>.

CUNHA FILHO, A. G. *Abordagem transiente sobre os efeitos do amortecimento viscoelástico na estabilidade aeroelástica de estruturas aeronáuticas*. 183 p. Thesis (PhD) — Universidade Federal de Uberlândia, 2019. DOI: <https://repositorio.ufu.br/handle/123456789/28227>.

DAI, Y.; YANG, C. Methods and advances in the study of aeroelasticity with uncertainties. *Chinese Journal of Aeronautics*, Chinese Society of Aeronautics and Astronautics, v. 27, p. 461–474, 2014. DOI: <http://dx.doi.org/10.1016/j.cja.2014.04.016>.

DAWNSON, S. T. M.; BRUNTON, S. L. Improved approximations to the wagner function using sparse identification of nonlinear dynamics. *AIAA Journal*, 2021. DOI: <http://arxiv.org/abs/2104.15122>.

DEB, K. et al. A fast and elitist multiobjective genetic algorithm: Nsga-ii. *IEEE Transactions on Evolutionary Computation*, v. 6, p. 182–197, 2002. DOI: <http://ieeexplore.ieee.org/document/996017/>.

DELGADO FILHO, M. A. et al. Combining viscoelastic damping and nonlinearities to widen the operational speed range of flutter energy harvesting. *Journal of Applied Mechanics*, v. 92, 2025. DOI: <https://doi.org/10.1115/1.4068452>.

DIAS, J. A. C.; DE MARQUI, C.; ERTURK, A. Three-degree-of-freedom hybrid piezoelectric-inductive aeroelastic energy harvester exploiting a control surface. *AIAA Journal*, v. 53, p. 394–404, 2015. DOI: <https://arc.aiaa.org/doi/10.2514/1.J053108>.

DINIZ, G. F. *Metodologia de projeto ótimo-robusto de sistemas aeroeletromecânicos com harvesters piezocerâmicos e circuitos multimodais para amortecimento passivo e supressão de flutter*. Thesis (PhD) — Universidade Federal de Uberlândia, 2024. DOI: <https://repositorio.ufu.br/handle/123456789/42227>.

ERTURK, A.; INMAN, D. J. *Piezoelectric Energy Harvesting*. [S.l.]: Wiley, 2011.

ERTURK, A. et al. On the energy harvesting potential of piezoaeroelastic systems. *Applied Physics Letters*, v. 96, p. 184103, 2010. DOI: <http://aip.scitation.org/doi/10.1063/1.3427405>.

FASIHI, A.; SHAHGHOLI, M.; GHAHREMANI, S. The effects of nonlinear energy sink and piezoelectric energy harvester on aeroelastic instability of an airfoil. *Journal of Vibration and Control*, v. 28, p. 1418–1432, 2022. DOI: <https://journals.sagepub.com/doi/10.1177/1077546321993585>.

FUNG, Y. C. *An Introduction to The Theory of Aeroelasticity*. [S.l.]: Dover Publications, Inc, 1993. 498 p.

HAO, Y.; LI, J. Prediction of the flutter envelope and parametric analysis of a flutter-based aeroelastic piezoelectric energy harvester. *Communications in Nonlinear Science and Numerical Simulation*, v. 142, p. 108520, 2025. DOI: <https://linkinghub.elsevier.com/retrieve/pii/S1007570424007056>.

HILTON, H. (aero)elasticity and (aero-)viscoelasticity: A critical appreciation of similarities and differences. In: *51st AIAA/ASME/ASCE/AHS/ASC Structures, Structural Dynamics, and Materials Conference 18th AIAA/ASME/AHS Adaptive Structures Conference 12th*. American Institute of Aeronautics and Astronautics, 2010. DOI: <http://arc.aiaa.org/doi/abs/10.2514/6.2010-2702>.

JONES, R. T. *The unsteady lift of a wing of finite aspect ratio: Report 681*. [S.l.], 1940. DOI: <https://ntrs.nasa.gov/citations/19930081468>.

LACARBONARA, W.; CETRARO, M. Flutter control of a lifting surface via visco-hysteretic vibration absorbers. *International Journal of Aeronautical and Space Sciences*, v. 12, p. 331–345, 2011. DOI: <https://doi.org/10.5139/IJASS.2011.12.4.331>.

LEAL JUNIOR, A. G. et al. Hysteresis compensation technique applied to polymer optical fiber curvature sensor for lower limb exoskeletons. *Measurement Science and Technology*, v. 28, p. 125103, 2017. DOI: <https://iopscience.iop.org/article/10.1088/1361-6501/aa946f>.

LEE, B.; PRICE, S.; WONG, Y. Nonlinear aeroelastic analysis of airfoils: bifurcation and chaos. *Progress in Aerospace Sciences*, v. 35, p. 205–334, 1999. DOI: <https://doi.org/10.1016/S0376-0421(98)00015-3>.

LEE, K.-H.; PARK, G.-J. Robust optimization considering tolerances of design variables. *Computers & Structures*, v. 79, p. 77–86, 2001. DOI: <https://linkinghub.elsevier.com/retrieve/pii/S0045794900001176>.

LI, D.; GUO, S.; XIANG, J. Aeroelastic dynamic response and control of an airfoil section with control surface nonlinearities. *Journal of Sound and Vibration*, v. 329, p. 4756–4771, 2010. DOI: <https://linkinghub.elsevier.com/retrieve/pii/S0022460X10003780>.

LI, K. et al. Nonlinear magnetic-coupled flutter-based aeroelastic energy harvester: modeling, simulation and experimental verification. *Smart Materials and Structures*, v. 28, p. 015020, 2019. DOI: <https://iopscience.iop.org/article/10.1088/1361-665X/aaede3>.

LI, K.; YANG, Z.; ZHOU, S. Performance enhancement for a magnetic-coupled bi-stable flutter-based energy harvester. *Smart Materials and Structures*, v. 29, p. 085045, 2020. DOI: <https://iopscience.iop.org/article/10.1088/1361-665X/ab9238>.

LI, Y. et al. A predictive multiscale computational framework for viscoelastic properties of linear polymers. *Polymer*, v. 53, p. 5935–5952, 2012. DOI: <https://linkinghub.elsevier.com/retrieve/pii/S0032386112008403>.

LI, Z.; ZHOU, S.; LI, X. A piezoelectric–electromagnetic hybrid flutter-based wind energy harvester: Modeling and nonlinear analysis. *International Journal of Non-Linear Mechanics*, v. 144, p. 104051, 2022. DOI: <https://doi.org/10.1016/j.ijnonlinmec.2022.104051>.

LI, Z.; ZHOU, S.; YANG, Z. Recent progress on flutter-based wind energy harvesting. *International Journal of Mechanical System Dynamics*, v. 2, p. 82–98, 2022. DOI: <https://doi.org/10.1002/msd2.12035>.

LIMA, A. M. G. de. *Modelagem e otimização robusta de sistemas mecânicos em presença de amortecimento viscoelástico*. 197 p. Thesis (PhD) — Universidade Federal de Uberlândia, 2007.

LIMA, A. M. G. de et al. An efficient modeling methodology of piezoaeroviscoelastic systems for vibration-based energy harvesting and subsonic flutter suppression. *Journal of the Brazilian Society of Mechanical Sciences and Engineering*, v. 47, p. 104, 2025. DOI: <https://doi.org/10.1007/s40430-025-05410-6>.

LIU, H.; GAO, X. Vibration energy harvesting under concurrent base and flow excitations with internal resonance. *Nonlinear Dynamics*, v. 96, p. 1067–1081, 2019. DOI: <http://link.springer.com/10.1007/s11071-019-04839-4>.

LIU, Q.; XU, Y.; KURTHS, J. Active vibration suppression of a novel airfoil model with fractional order viscoelastic constitutive relationship. *Journal of Sound and Vibration*, v. 432, p. 50–64, 2018. DOI: <https://doi.org/10.1016/j.jsv.2018.06.022>.

LIU, S.; LI, P.; YANG, Y. On the design of an electromagnetic aeroelastic energy harvester from nonlinear flutter. *Meccanica*, v. 53, p. 2807–2831, 2018. DOI: <https://doi.org/10.1007/s11012-018-0875-6>.

LOBATO, F. S. *Otimização Multi-Objetivo para o Projeto de Sistemas de Engenharia*. 402 p. Thesis (PhD) — Universidade Federal de Uberlândia, 2008.

MARTINS, P. C. O. *Estudo da influência do amortecimento viscoelástico no fenômeno aeroelástico de Flutter*. Thesis (Master) — Universidade Federal de Uberlândia, 2014. DOI: <https://repositorio.ufu.br/handle/123456789/14978>.

MARTINS, P. C. O. et al. Numerical and experimental investigation of aeroviscoelastic systems. *Mechanical Systems and Signal Processing*, v. 85, p. 680–697, 2017. DOI: <https://doi.org/10.1016/j.ymssp.2016.08.043>.

MARTINS, P. C. O. et al. Hybrid control technique applied to an aero-servo-viscoelastic simplified wing model. *Aerospace Science and Technology*, v. 122, p. 107387, 2022. DOI: <https://doi.org/10.1016/j.ast.2022.107387>.

MCCARTHY, J. M. et al. Downstream flow structures of a fluttering piezoelectric energy harvester. *Experimental Thermal and Fluid Science*, v. 51, p. 279–290, 2013. DOI: <https://linkinghub.elsevier.com/retrieve/pii/S0894177713001854>.

MCCARTHY, J. M. et al. Fluttering energy harvesters in the wind: A review. *Journal of Sound and Vibration*, v. 361, p. 355–377, 2016. DOI: <https://linkinghub.elsevier.com/retrieve/pii/S0022460X1500783X>.

MOHEIMANI, S. O. R.; FLEMING, A. J. *Piezoelectric Transducers for Vibration Control and Damping*. Springer-Verlag, 2006. 271 p. DOI: <http://link.springer.com/10.1007/1-84628-332-9>.

MOKHTARI, M.; PERMOON, M. R.; HADDADPOUR, H. Aeroelastic analysis of sandwich cylinder with fractional viscoelastic core described by zener model. *Journal of Fluids and Structures*, v. 85, p. 1–16, 2019. DOI: <https://linkinghub.elsevier.com/retrieve/pii/S0889974618301567>.

NAQVI, A. et al. Energy harvesting from fluid flow using piezoelectric materials: A review. *Energies*, v. 15, p. 7424, 2022. DOI: <https://www.mdpi.com/1996-1073/15/19/7424>.

NASHIF, A. D.; JONES, D. I. G.; HENDERSON, J. P. *Vibration Damping*. [S.l.]: John Wiley & Sons, Inc., 1985.

PEREIRA, D. A. et al. Effects of combined hardening and free-play nonlinearities on the response of a typical aeroelastic section. *Aerospace Science and Technology*, v. 50, p. 44–54, 2016. DOI: <https://doi.org/10.1016/j.ast.2015.12.022>.

PIGOLOTTI, L. et al. Critical and post-critical behaviour of two-degree-of-freedom flutter-based generators. *Journal of Sound and Vibration*, v. 404, p. 116–140, 2017. DOI: <https://linkinghub.elsevier.com/retrieve/pii/S0022460X17304030>.

PRITZ, T. Five-parameter fractional derivative model for polymeric damping materials. *Journal of Sound and Vibration*, v. 265, p. 935–952, 2003. DOI: <https://linkinghub.elsevier.com/retrieve/pii/S0022460X02015304>.

RAO, S. S. *Engineering Optimization: Theory and Practice*. 4. ed. John Wiley & Sons, Inc., 2009. DOI: <https://onlinelibrary.wiley.com/doi/book/10.1002/9780470549124>.

RAO, S. S. *Mechanical Vibrations*. 5th. ed. [S.l.]: Pearson, 2010. 1104 p.

RONG, Z.; CAO, B.; HU, J. Stability analysis on an aeroelastic system for design of a flutter energy harvester. *Aerospace Science and Technology*, v. 60, p. 203–209, 2017. DOI: <https://linkinghub.elsevier.com/retrieve/pii/S1270963816310811>.

ROSTAMI, S.; NERI, F.; GYAURSK, K. On algorithmic descriptions and software implementations for multi-objective optimisation: A comparative study. *SN Computer Science*, v. 1, p. 247, 2020. DOI: <https://link.springer.com/10.1007/s42979-020-00265-1>.

SALES, T. de P. et al. Dynamic assessment of nonlinear typical section aeroviscoelastic systems using fractional derivative-based viscoelastic model. *Journal of Sound and Vibration*, v. 423, p. 230–245, 2018. DOI: <https://doi.org/10.1016/j.jsv.2018.02.008>.

SALES, T. de P. et al. Modeling and dynamic characterization of nonlinear non-smooth aeroviscoelastic systems. *Mechanical Systems and Signal Processing*, v. 116, p. 900–915, 2019. DOI: <https://doi.org/10.1016/j.ymssp.2018.07.003>.

SANTOS, C. R. dos; MARQUES, F. D.; HAJJ, M. R. The effects of structural and aerodynamic nonlinearities on the energy harvesting from airfoil stall-induced oscillations. *Journal of Vibration and Control*, v. 25, p. 1991–2007, 2019. DOI: <https://journals.sagepub.com/doi/10.1177/1077546319844383>.

SEARS, W. R. Operational methods in the theory of airfoils in non-uniform motion. *Journal of the Franklin Institute*, v. 230, p. 95–111, 1940. DOI: <https://linkinghub.elsevier.com/retrieve/pii/S0016003240906512>.

SHAN, X. et al. Enhancing performance of a piezoelectric energy harvester system for concurrent flutter and vortex-induced vibration. *Energies*, v. 13, p. 3101, 2020. DOI: <https://www.mdpi.com/1996-1073/13/12/3101>.

SHU, Z.; YOU, R.; ZHOU, Y. Viscoelastic materials for structural dampers: A review. *Construction and Building Materials*, v. 342, p. 127955, 2022. DOI: <https://linkinghub.elsevier.com/retrieve/pii/S0950061822016257>.

SILVA, G. C. *Sistemas de controle ativo e passivo para supressão de flutter de uma seção típica*. Thesis (PhD) — ITA, 2016.

SILVA, G. C. et al. Active and passive control for acceleration reduction of an aeroelastic typical wing section. *Journal of Vibration and Control*, v. 24, p. 2673–2687, 2018. DOI: <https://doi.org/10.1177/1077546317728147>.

SILVA, L. A. *Modelagem Aeroviscoelástica de painéis sanduíches planos via método dos paineis*. 110 p. Thesis (PhD) — Universidade Federal de Uberlândia, 2018. DOI: <https://repositorio.ufu.br/handle/123456789/31229>.

SILVESTRE, F. J.; LUCKNER, R. Experimental validation of a flight simulation model for slightly flexible aircraft. *AIAA Journal*, v. 53, p. 3620–3636, 2015. DOI: <https://arc.aiaa.org/doi/10.2514/1.J054023>.

SOUSA, V. C. et al. Enhanced aeroelastic energy harvesting by exploiting combined nonlinearities: theory and experiment. *Smart Materials and Structures*, v. 20, p. 094007, 2011. DOI: <https://iopscience.iop.org/article/10.1088/0964-1726/20/9/094007>.

SRINIVAS, N.; DEB, K. Muiltiobjective optimization using nondominated sorting in genetic algorithms. *Evolutionary Computation*, v. 2, p. 221–248, 1994. DOI: <https://direct.mit.edu/evco/article/2/3/221-248/1396>.

STOPPA, M. *Modelagem numérica e projeto ótimo de sistemas de amortecimento viscoelásticos aplicados a placas retangulares*. Thesis (PhD) — Universidade Federal de Uberlândia, 2003. DOI: <https://repositorio.ufu.br/handle/123456789/30428>.

THEODORSEN, T. *General Theory of Aerodynamic Instability and the Mechanism of Flutter NTRS Document, NACA-TR-496.* [S.l.], 1935. DOI: <https://ntrs.nasa.gov/citations/19930090935>.

TIAN, H. et al. A method for investigating aerodynamic load models of piezoaeroelastic energy harvester. *Journal of Sound and Vibration*, v. 502, p. 116084, 2021. DOI: <https://linkinghub.elsevier.com/retrieve/pii/S0022460X21001565>.

TIAN, H. et al. Enhanced performance of airfoil-based piezoaeroelastic energy harvester: numerical simulation and experimental verification. *Mechanical Systems and Signal Processing*, v. 162, p. 108065, 2022. DOI: <https://linkinghub.elsevier.com/retrieve/pii/S0888327021004544>.

TIAN, W.; YANG, Z.; GU, Y. Dynamic analysis of an aeroelastic airfoil with freeplay nonlinearity by precise integration method based on padé approximation. *Nonlinear Dynamics*, v. 89, p. 2173–2194, 2017. DOI: <http://link.springer.com/10.1007/s11071-017-3577-z>.

VANDERPLAATS, G. N. *Numerical optimization techniques for engineering design*. 3. ed. [S.l.]: Vanderplaats Research and Development, Inc, 1999. 449 p.

WAGNER, H. Über die entstehung des dynamischen auftriebes von tragflügeln. *ZAMM - Journal of Applied Mathematics and Mechanics*, v. 5, p. 17–35, 1925.

WANG, E. et al. On the nonlinear dynamics of self-sustained limit-cycle oscillations in a flapping-foil energy harvester. *Journal of Fluids and Structures*, v. 83, p. 339–357, 2018. DOI: <https://linkinghub.elsevier.com/retrieve/pii/S0889974618303475>.

WANG, G. *Analyses of Sandwich Beams and Plates with Viscoelastic Cores*. 196 p. Thesis (PhD) — University of Maryland, 2001.

WANG, Q. et al. Current status and prospects of digital twin approaches in structural health monitoring. *Buildings*, v. 15, p. 1021, 2025. DOI: <https://www.mdpi.com/2075-5309/15/7/1021>.

WRIGHT, J. R.; COOPER, J. E. *Introduction to Aircraft Aeroelasticity and Loads*. 2. ed. Wiley, 2014. 574 p. DOI: <https://onlinelibrary.wiley.com/doi/book/10.1002/9781118700440>.

WU, Y. et al. Piezoaeroelastic energy harvesting based on an airfoil with double plunge degrees of freedom: Modeling and numerical analysis. *Journal of Fluids and Structures*, v. 74, p. 111–129, 2017. DOI: <https://linkinghub.elsevier.com/retrieve/pii/S0889974616306892>.

YANG, Y.-G.; GUO, S.-L.; SUN, Y.-H. A viscoelastic energy harvester: probabilistic and bifurcation analysis. *The European Physical Journal Plus*, v. 137, p. 1091, 2022. DOI: <https://link.springer.com/10.1140/epjp/s13360-022-03303-4>.

ZHAO, L.; YANG, Y. Enhanced aeroelastic energy harvesting with a beam stiffener. *Smart Materials and Structures*, v. 24, p. 032001, 2015. DOI: <https://iopscience.iop.org/article/10.1088/0964-1726/24/3/032001>.

ZHOU, Z. et al. Scavenging wind energy by a dynamic-stable flutter energy harvester with rectangular wing. *Applied Physics Letters*, v. 114, 2019. DOI: <https://pubs.aip.org/apl/article/114/24/243902/594356/Scavenging-wind-energy-by-a-dynamic-stable-flutter>.

Appendix A

Aerodynamic Matrices

The aerodynamic matrices $\boldsymbol{a_j}$ and $\mathbf{b}_j$ $(j = 1, 2, 3, 4)$, mentioned in Chapter II, are defined by the following expressions (THEODORSEN, 1935; SILVA et al., 2018):

$$\boldsymbol{a_1} = l \begin{bmatrix} -\pi b^2 \rho & \pi b^3 \rho a \\ \pi b^3 \rho a & -\pi b^{-4} \rho \left(\frac{1}{8} + a^2\right) \end{bmatrix} \tag{A.1}$$

$$\boldsymbol{a_2} = l \begin{bmatrix} -2\pi\rho V b & -2\pi\rho V b^2 (1-a) \\ 2b^2 \left(a + \frac{1}{2}\right) \pi\rho V & \left[-\pi b^3 \rho + 2b^3 \left(a + \frac{1}{2}\right) \pi\rho\right] V \left(\frac{1}{2} - a\right) \end{bmatrix} \tag{A.2}$$

$$\boldsymbol{a_3} = l \begin{bmatrix} 0 & -2\pi\rho V^2 b \\ 0 & 2b^2 \left(a + \frac{1}{2}\right) \pi\rho V^2 \end{bmatrix} \tag{A.3}$$

$$\boldsymbol{a_4} = l \begin{bmatrix} -2\pi\rho V b & -2\pi\rho V b \\ 2b^2 \left(a + \frac{1}{2}\right) \pi\rho V & 2b^2 \left(a + \frac{1}{2}\right) \pi\rho V \end{bmatrix} \tag{A.4}$$

$$\mathbf{b_1} = \begin{bmatrix} -0.165 & -0.165b\,(0.5 - a) \\ -0.335 & -0.335b\,(0.5 - a) \end{bmatrix} \tag{A.5}$$

$$\mathbf{b_2} = \begin{bmatrix} 0 & -0.165V \\ 0 & -0.335V \end{bmatrix} \tag{A.6}$$

$$\mathbf{b_3} = \begin{bmatrix} 0 & 0 \\ 0 & 0 \end{bmatrix} \tag{A.7}$$

$$\mathbf{b_4} = \begin{bmatrix} -0.041\frac{V}{b} & 0 \\ 0 & -0.320\frac{V}{b} \end{bmatrix} \tag{A.8}$$

Appendix B

State Matrix

By imposing linear springs in Eq. 3.21, $a_0^h = a_0^\theta = 1$, $a_1^h = a_1^\theta = 0$, the state-space representation for the FEH device without viscoelastic dampers is $\dot{\mathbf{x}} = \mathbf{A}\mathbf{x}$, where $\mathbf{x} = \begin{Bmatrix} h & \theta & \dot{h} & \dot{\theta} & \lambda_1 & \lambda_2 & v \end{Bmatrix}^{\mathsf{T}}$. Following the procedure described in Chapter III, the state matrix can be written as:

$$\mathbf{A} = \begin{bmatrix} \mathbf{0} & \mathbf{I} & \mathbf{0} & \mathbf{0} \\ \mathbf{A_{21}} & \mathbf{A_{22}} & \mathbf{A_{23}} & \mathbf{A_{24}} \\ \mathbf{A_{31}} & \mathbf{A_{32}} & \mathbf{A_{33}} & \mathbf{A_{34}} \\ \mathbf{0} & \mathbf{A_{42}} & \mathbf{0} & A_{44} \end{bmatrix} \tag{B.1}$$

where:

$$\mathbf{A_{21}} = -\tilde{\mathbf{M}}^{\mathbf{-1}}\tilde{\mathbf{K}} \tag{B.2}$$

$$\mathbf{A_{22}} = -\tilde{\mathbf{M}}^{\mathbf{-1}}\tilde{\mathbf{C}} \tag{B.3}$$

$$\mathbf{A_{23}} = -\tilde{\mathbf{M}}^{\mathbf{-1}}\boldsymbol{a_4} \tag{B.4}$$

$$\mathbf{A_{24}} = \tilde{\mathbf{M}}^{-1}\mathbf{H}^{\mathsf{T}} \tag{B.5}$$

$$\mathbf{A_{31}} = \left(\mathbf{b}_3 - \mathbf{b_1}\tilde{\mathbf{M}}^{-1}\tilde{\mathbf{K}}\right) \tag{B.6}$$

$$\mathbf{A_{32}} = \left(\mathbf{b_2} - \mathbf{b_1}\tilde{\mathbf{M}}^{-1}\tilde{\mathbf{C}}\right) \tag{B.7}$$

$$\mathbf{A_{33}} = \left(\mathbf{b_4} + \mathbf{b_1}\tilde{\mathbf{M}}^{-1}\boldsymbol{a_4}\right) \tag{B.8}$$

$$\mathbf{A_{34}} = \mathbf{b_1}\tilde{\mathbf{M}}^{-1}\mathbf{H}^{\mathsf{T}} \tag{B.9}$$

$$\mathbf{A_{42}} = -C_{eq}^{-1}\mathbf{H} \tag{B.10}$$

$$A_{44} = -(RC_{eq})^{-1} \tag{B.11}$$

If the piezoelectric transduction is removed, there will be no electromechanical coupling, and thus no voltage. For this situation, $\mathbf{x} = \begin{Bmatrix} h & \theta & \dot{h} & \dot{\theta} & \lambda_1 & \lambda_2 \end{Bmatrix}^{\mathsf{T}}$ and the state matrix becomes the following:

$$\mathbf{A} = \begin{bmatrix} \mathbf{0} & \mathbf{I} & \mathbf{0} \\ \mathbf{A_{21}} & \mathbf{A_{22}} & \mathbf{A_{23}} \\ \mathbf{A_{31}} & \mathbf{A_{32}} & \mathbf{A_{33}} \end{bmatrix} \tag{B.12}$$